論文 / 著書情報
Article / Book Information

題目(和文)	不定比酸化物 La_{n+1}Ni_nO_{3n+1+δ}および La₂CuO_{4+δ}結晶における過剰酸素配列の凍結過程と秩序化過程に関する研究
Title(English)	Ordering and Freezing-in Processes of Excess Oxygen Atoms in Nonstoichiometric Crystals La_{n+1}Ni_nO_{3n+1+δ}and La₂CuO_{4+δ}
著者(和文)	京免徹
Author(English)	Toru Kyomen
出典(和文)	学位:博士(理学), 学位授与機関:東京工業大学, 報告番号:甲第3969号, 授与年月日:1999年3月26日, 学位の種別:課程博士, 審査員:小國正晴
Citation(English)	Degree:Doctor of Science, Conferring organization: Tokyo Institute of Technology, Report number:甲第3969号, Conferred date:1999/3/26, Degree Type:Course doctor, Examiner:
学位種別(和文)	博士論文
Type(English)	Doctoral Thesis

DOCTORAL DISSERTATION

Ordering and Freezing-in Processes of Excess Oxygen Atoms in Nonstoichiometric Crystals $La_{n+1}Ni_nO_{3n+1+\delta}$ and $La_2CuO_{4+\delta}$

by

Tôru KYÔMEN

under supervision of

Professor Masaharu OGUNI

Graduate School of Science and Engineering

Tokyo Institute of Technology

January, 1999

Acknowledgments

I would like to express my sincere gratitude to Professor Masaharu Oguni, who introduced me to this field of investigation, for valuable suggestions and encouragement throughout the corse of this study as well as illuminating assistance in refining the expression of this thesis.

I am also deeply indebted to Dr. Minoru Hanaya for his encouragement, useful advice and fruitful discussion.

I wish to give my thanks Associate Professor Mitsuru Itoh and Dr. Jian Ding Yu for their collaboration in the studies of $La_2CuO_{4+\delta}$ system, especially, on the preparation of single crystals, the adjustments of excess oxygen composition, and the measurements of magnetic susceptibilities.

I wish to give my thanks Associate Professor Kenzô Kitayama for his collaboration in the adjustments of excess oxygen composition for some samples of $La_2NiO_{4+\delta}$.

Thanks are extended to Dr. Kazuhisa Kobashi for his collaboration in the X-ray powder diffraction measurements of a few samples.

Thanks are extended to Mr. Hiroyasu Tamura for his collaboration in the heat capacity measurements of $La_2CuO_{4.035}$ crystal.

I greatfully acknowledge many valuable advice and discussion by the member of Oguni Laboratory.

Finally, I am very grateful to my parents for hearty encouragement.

Toru KYÔMEN

Tokyo, Japan

January, 1999

Contents

Chapter 1

Introduction

There is a homologous series of oxide crystals refered to as Ruddlesden-Popper type which are constructed by stacking n successive ABO_3 perovskite layers and one AO rock-salt layer alternately as shown in Fig. 1.1 for $n = 2$ and 3,[1, 2] and thus the chemical formula are expressed by $A_{n+1}B_nO_{3n+1}$. These oxides often show oxygen-deficient or -excess nonstoichiometry. The present study is concerned with the nonstoichiometry of Ruddlesden-Popper type oxides with excess oxygen; namely, $La_{n+1}Ni_nO_{3n+1+\delta}$ and $La_2CuO_{4+\delta}$ crystals. In this chapter, crystallographic and thermodynamic studies, and a few topics on electronic properties of $La_2NiO_{4+\delta}$ and $La_2CuO_{4+\delta}$ crystals are reviewed briefly with stress on the oxygen nonstoichiometry, and the aims of the present study are mentioned in the last section of this chapter.

1.1 Oxygen nonstoichiometry, crystallographic and thermodynamic properties of $La_2MO_{4+\delta}$ (M= Ni, Cu) system

1.1.1 Oxygen nonstoichiometry

It is necessary to determine La/M cation ratio of $La_2MO_{4+\delta}$(M = Ni, Cu) crystal in order to discuss its oxygen nonstoichiometry. There was a controversy about La/Cu cation ratio of $La_2CuO_{4+\delta}$ crystals in the early days. Some research groups[3, 4] reported the presence of La vacancies in La_2CuO_4 crystal, however Schirber *et al.*[5] conducted careful electron

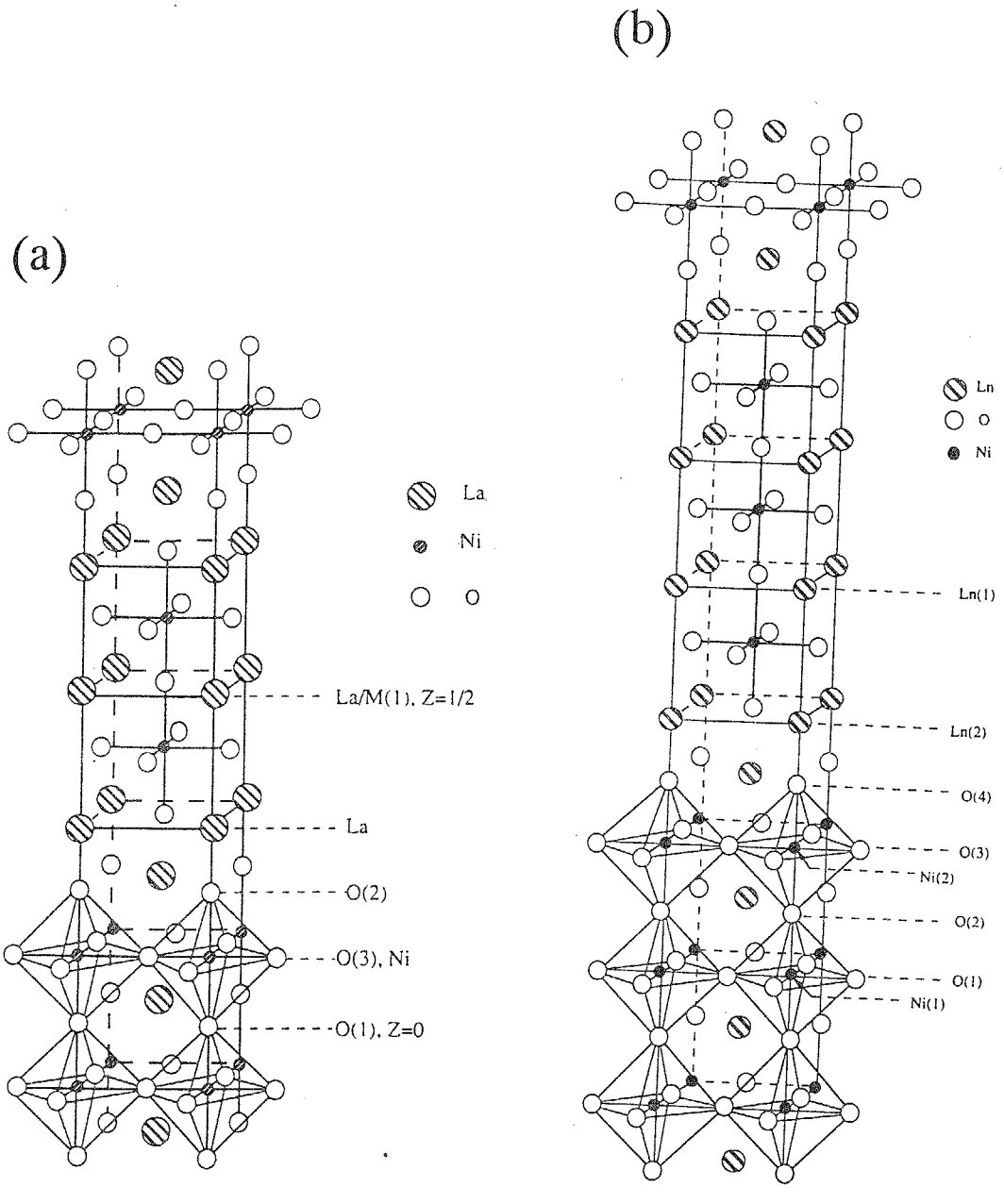

Figure 1.1: Crystal structures of Ruddlesden-Popper type oxides: (a) $La_3Ni_2O_7$;[1] (b) $Ln_4Ni_3O_{10}$.[2]

probe microanalysis with an estimated uncertainty of 1 % and obtained the stoichiometric value, 2, for the cation ratio of $La_2CuO_{4+\delta}$ crystal when it was prepared by annealing in high-pressure oxygen atmosphere. Jorgensen *et al.*[6] have done a conclusive work on the problem: They prepared polyphase specimens with varying La/Cu ratio, and measured the abundance of CuO and La_2O_3 impurity phases using multiphase Rietveld analysis of neutron powder diffraction data. It was concluded from the results that the La/Cu cation ratio of $La_2CuO_{4+\delta}$ phase did not vary from 2 by more than 0.01 and thus no significant concentration of La vacancies was present in $La_2CuO_{4+\delta}$ phase. $La_2CuO_{4+\delta}$ crystal are thus considered to be stoichiometric concerning the La/Cu cation ratio. In La_2NiO_4, however, there is a report which indicates the presence of La vacancies in the single crystal grown by floating zone method.[7] The chemical formula of the single crystal detemined by wet chemistry and thermogravimetric analysis was $La_{1.9}NiO_{3.93}$. If there were such a large amount of La vacancies in the crystal, La_2O_3 impurity phase as remaining subjected to no reaction could be detected by X-ray powder diffraction method. But the presence of such a phase has not been reported in studies of many research groups. Thus, the appearance of La vacancies would be associated only with the oxygen deficiency of the crystal.

Kitayama[8] proposed a phase diagram of La-Ni-O system by using a thermogravimetric technique and showed that the equilibrium value of δ of $La_2NiO_{4+\delta}$ crystal is 0.08 at 1473 K under 1 atm of oxygen partial pressure, P_{O_2}. The equilibrium value of δ has been reported to increase with decreasing temperature and to reach 0.16 at around 600 K under $P_{O_2} = 1$ atm.[9] Below 600 K, however, the establishment of equilibrium state with respect to excess oxygen content is hard because a potential barrier becomes too large for oxygen to enter into or go out of a crystal. On the other hand, oxygen non-stoichiometry of $La_2CuO_{4+\delta}$ crystal is much smaller than that of $La_2NiO_{4+\delta}$ crystal: It has been reported that equilibrium values of δ are 0.01 and 0.03 under $P_{O_2} = 1$ atm and $P_{O_2} = 100$ atm, respectively, at 853 K.[6] Recently, Wattiaux *et al.*[10, 11] reported that La_2CuO_4 can be oxidized electrochemically in basic aqueous solution in the potential range of $600 < E < 800$ mV at room temperature, and that $La_2CuO_{4+\delta}$ was prepared up

to $\delta \approx 0.1$ by the technique. They proposed that the following reaction occurred in the potential range:

$$La_2CuO_4 + 2\delta OH^- \rightarrow La_2CuO_{4+\delta} + \delta H_2O + 2\delta e^-. \quad (1.1)$$

In the early days, Jorgensen *et al.*[12] and Ganguly *et al.*[13] proposed that excess oxygen atoms are incorporated as forms of O^{2-} and O_2^{2-}, respectively, in La_2NiO_4 crystal with charge balance requiring NiO_2^- to be formed. It has been recently found from thermogravimetric analyses[14, 15] that O^{2-} dominates at least in the region of $0.03 < \delta < 0.15$. On the other hand, a number of proposals have been given in the early days concerning the form of excess oxygen atoms in La_2CuO_4 crystal including O^{2-}, O^-, O_2^{2-}, O_2^-, and O_2, with charge balance requiring CuO_2^- to be formed.[5, 6, 16, 17, 18] Su *et al.*[19] measured oxygen pressure dependence of electric conductivity of $La_2CuO_{4+\delta}$ crystal at 1123 K, and showed that excess oxygen atoms are incorporated as O^{2-} in the range of $-4 < \log(P_{O_2}/\text{atm}) < 0$. Furthermore, they showed, from the plot of the excess oxygen compositions versus the oxygen partial pressures under which the samples were prepared, that excess oxygen atoms are incorporated as O^{2-} at least in the range of $-5 < \log(P_{O_2}/\text{atm}) < 5$ which corresponds to $0 < \delta < 0.07$.

1.1.2 Crystal structures and structural phase transitions of stoichiometric crystal

The crystal system and the space group of both the stoichiometric crystals La_2NiO_4 and La_2CuO_4 at high temperatures are tetragonal and $I4/mmm$, respectively. This crystal structure refered to as a K_2NiF_4 type is shown in Fig. 1.2(a). There are two units of La_2MO_4 in the body-centered unit cell. By the way, face-centered tetragonal notation, $F4/mmm$, is often used for the space group of the crystal structure instead of body-centered tetragonal notation, $I4/mmm$, in order to coincide with the unit cells of the other crystal structures mentioned as follows. As shown in Fig. 1.2(b), a- and b- axes of $F4/mmm$ notation are along two perpendicular diagonals of square composed of a- and b-axes of $I4/mmm$ notation, and thus there are four units of La_2MO_4 in the face-centered

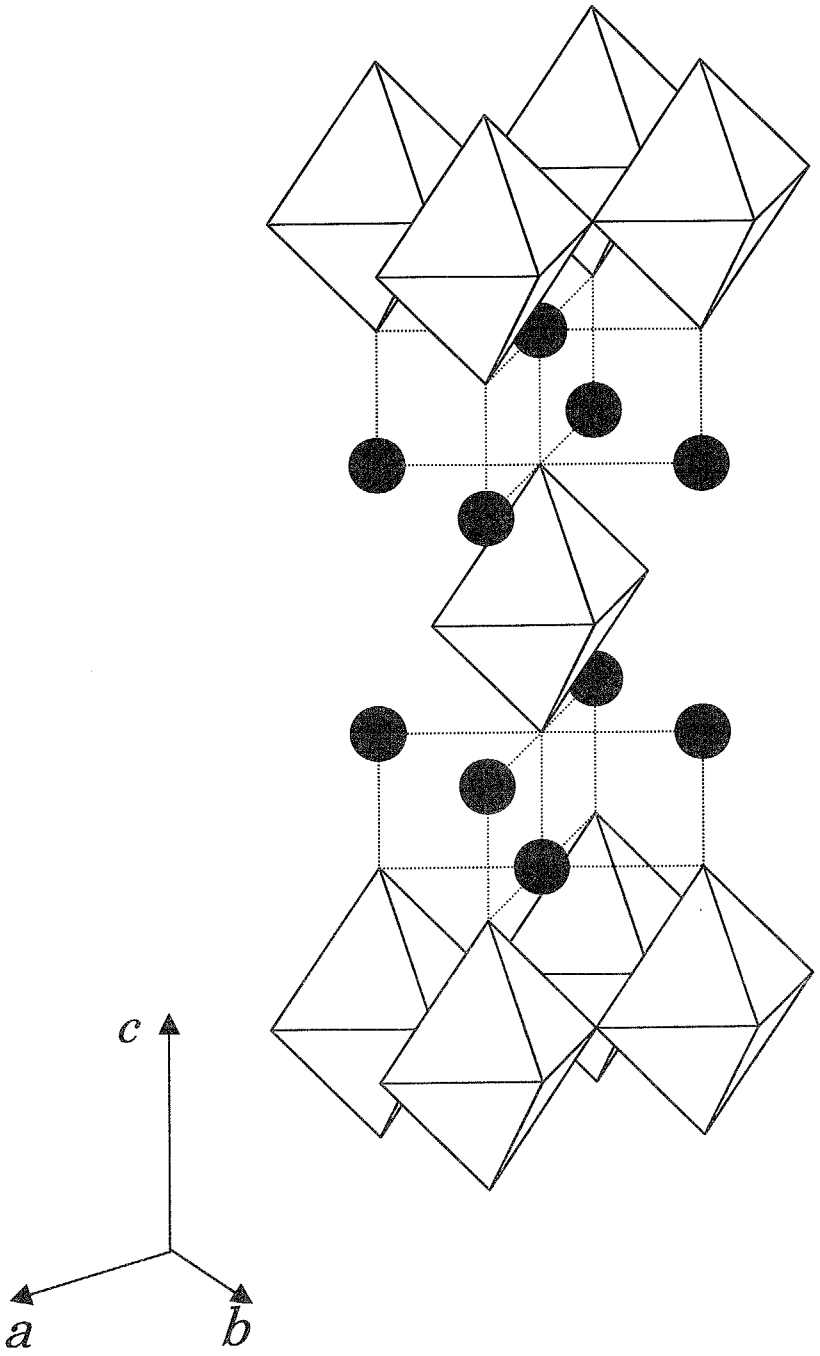

Figure 1.2(a): Crystal structure of stoichiometric crystals La_2MO_4 (M = Ni, Cu) at high temperatures in $I4/mmm$ notation: Solid circles represent lanthanum atoms. Oxygen atoms and nickel or copper atoms are located at the corners and center of an octahedron, respectively. This structure is named a K_2NiF_4 type structure in common use.

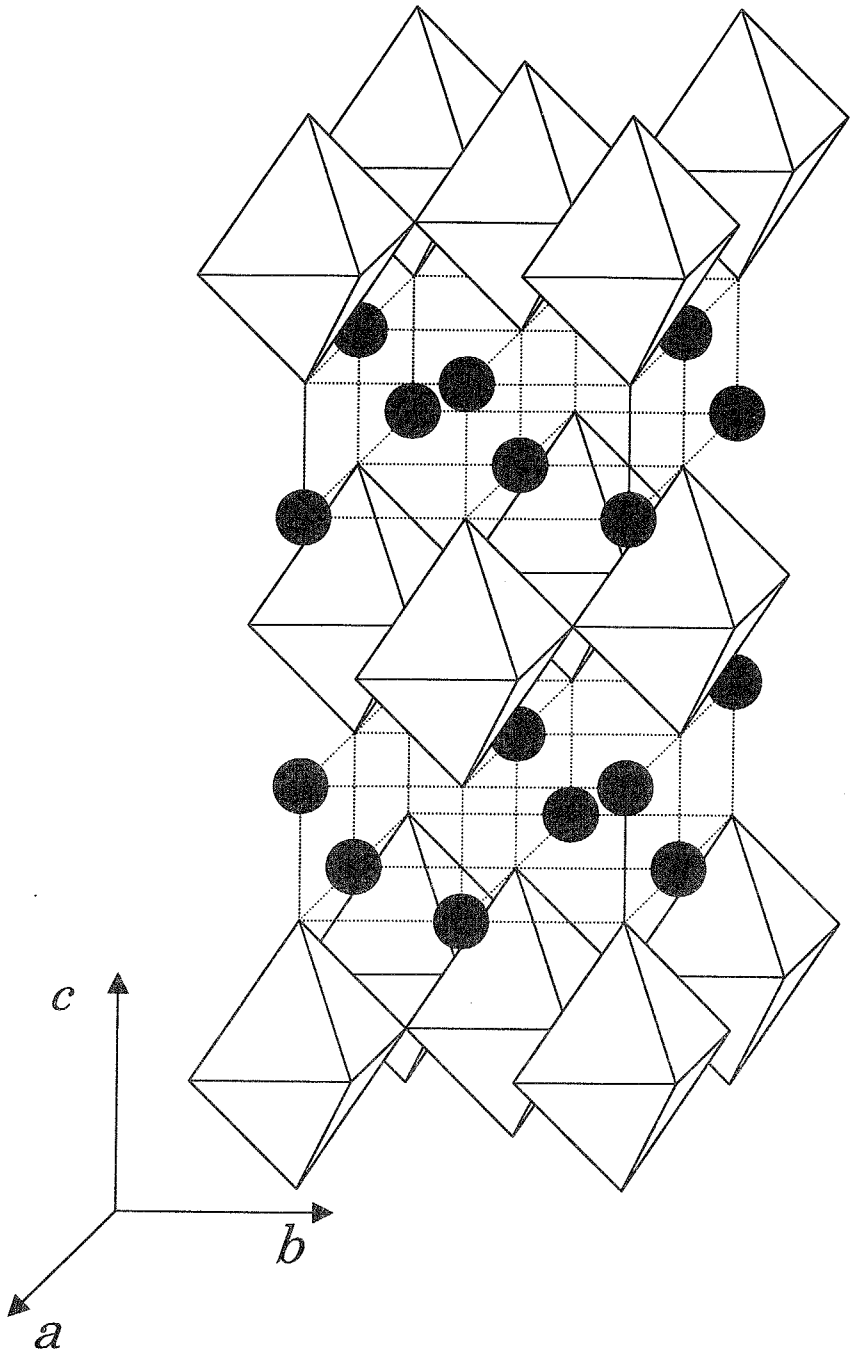

Figure 1.2(b): Crystal structure of stoichiometric crystals La_2MO_4 (M = Ni, Cu) at high temperatures in $F4/mmm$ notation.

unit cell of $F4/mmm$ notation. Both the crystals La_2NiO_4 and La_2CuO_4 transform to another crystal structure at around 770 K[20] and 530 K[21], respectively. These phase transitions are of a second-order type. The crystal system and space group below the respective temperatures are orthorhombic and $Bmab$, respectively. The crystal structure is shown in Fig. 1.3, and lattice constants, bond lengths, and an angle M-O(1)-M are tabulated in Table. 1.1.[6, 12] The difference from $F4/mmm$ structure is that MO_6 sharing a planar oxygen atom, O(1), rotate in the opposite directions to each other about a-axis. It is found that the MO_6 octahedra are elongated along the c-axis and that M-O(1)-M angle deviates from 180°. La_2CuO_4 crystal has $Bmab$ structure at low temperatures down to at least a few Kelvin. On the other hand, La_2NiO_4 crystal is known to transform subsequently to another structure at around 80 K.[22] The phase transition is of a first-order type. The space group of the low temperature phase has been proposed to be $P4_2/ncm$ by Rice *et al.*[23] and $Pccn$ by Hayashi *et al.*,[24] respectively. The structure of these phases are expressed as follows. (The space group, $Fmmm$, has often appeared in papers for the structure of nonstoichiometric crystal. The crystal structure of $Fmmm$ is similar to that of $F4/mmm$. It is obtained as transformation from $F4/mmm$ through elongation of the b-axis, and thus a symmetry element of the four-fold axis vanishes.)

The successive structural phase transitions of a K_2NiF_4-type crystal have been discussed by Axe *et al.*[25] on the basis of Landau theory. These transitions occur through variations in tilts of MO_6 octahedra, each tilt being characterized by displacements of the apical oxygen atoms, O(2) in Fig. 1.3, of MO_6 octahedra. Provided that the displacements of an apical oxygen atom along the [100] and [010] directions in $F4/mmm$ notation are designated by Q_1 and Q_2, respectively, the magnitudes of Q_1 and Q_2 in each space group are given as follows and shown graphically in Fig. 1.4.

$$
\begin{aligned}
F4/mmm \quad &; \ |Q_1| = |Q_2| = 0 \\
Bmab \quad &; \ |Q_1| = 0, |Q_2| \neq 0 \\
P4_2/ncm \quad &; \ |Q_1| = |Q_2| \neq 0 \\
Pccn \quad &; \ |Q_1| \neq |Q_2|, |Q_1| \neq 0, |Q_2| \neq 0.
\end{aligned}
$$

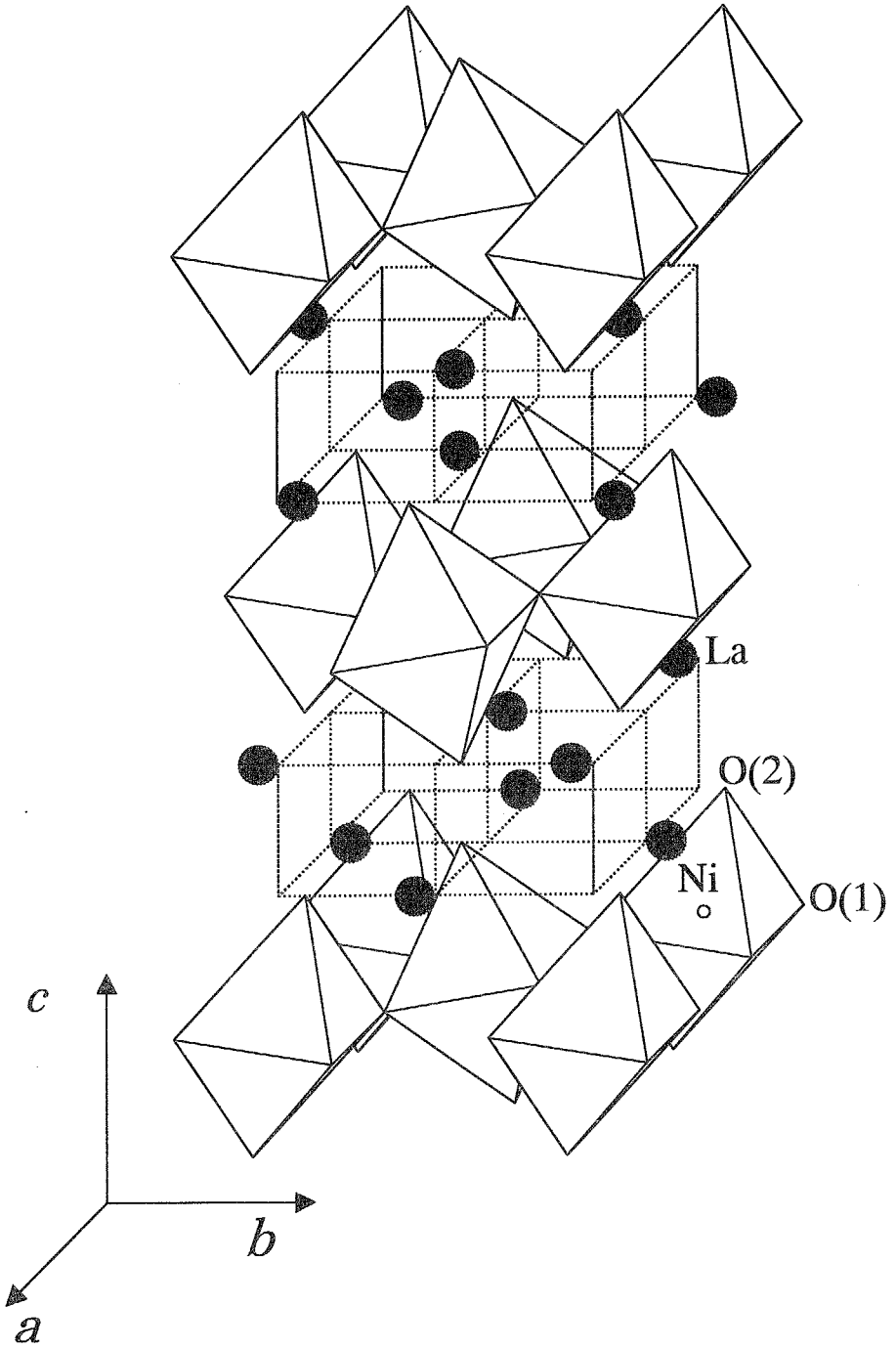

Figure 1.3: Crystal structure of stoichiometric crystals La_2MO_4 (M = Ni, Cu) at room temperature; Each octahedron is tilted in the direction of the b-axis. The space group is *Bmab*.

Table 1.1: lattice constants, bond length, and bond angle of La_2NiO_4[12] and La_2CuO_4[6] crystals with *Bmab* structure. Units of length and angle are angstrom and degree, respectively.

M	Ni	Cu
a	5.466	5.334
b	5.533	5.414
c	12.555	13.126
M-O(1)	1.947	1.903
M-O(2)	2.260	2.429
La-O(2)	2.328	2.351
$\angle M$-O(1)-M	173.6	173.2

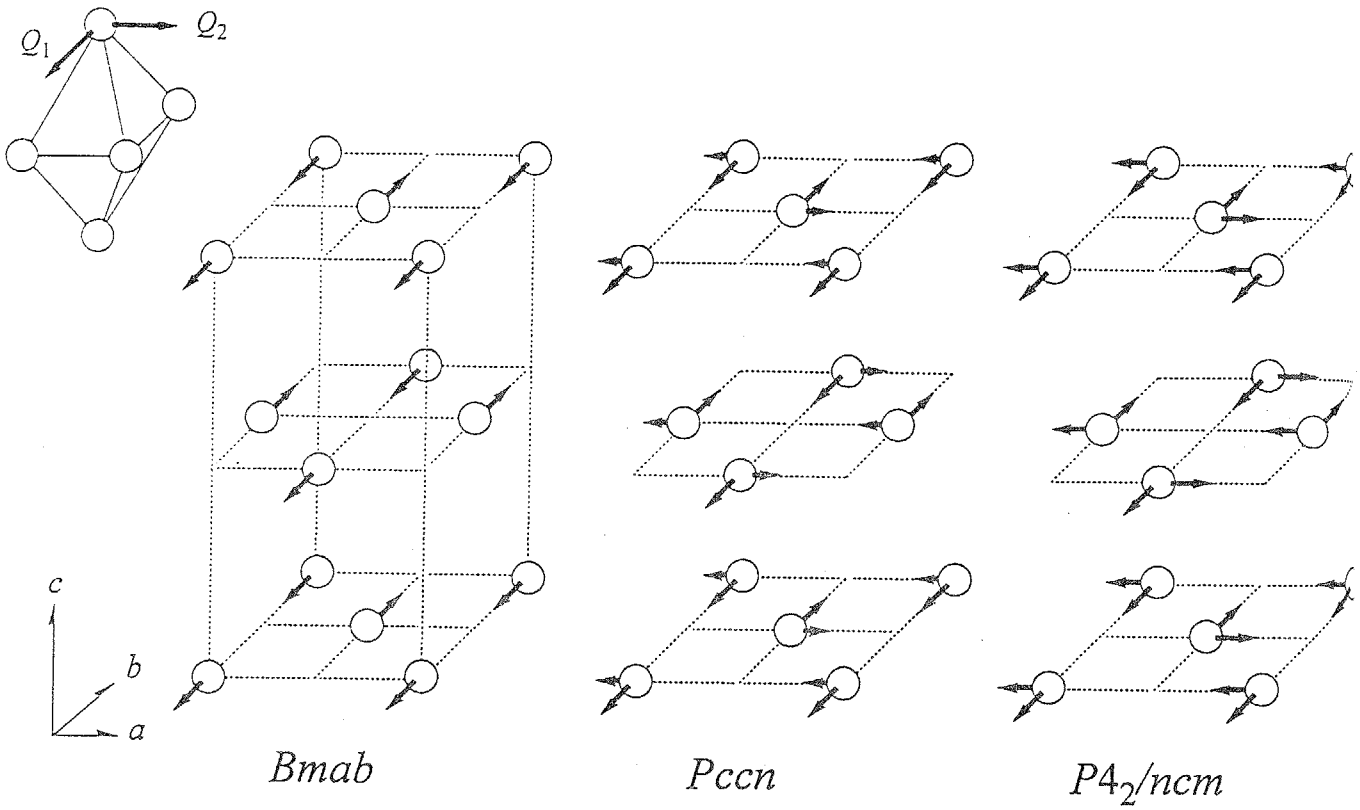

Figure 1.4: Arrangement of tilts of MO_6 octahedra represented by the displacements of apical oxygen atoms in different structural modifications, as viewed along the c-axis. The magnitudes of displacements along the a- and b- axes, $|Q_1|$ and $|Q_2|$, are different from and equal to each other in space groups $Pccn$ and $P4_2/ncm$, respectively.

It has been found from the analysis that following two cases of successive phase transitions potentially occur;

$$\text{case. 1} \quad F4/mmm \overset{(a)}{\leftrightarrow} Bmab \overset{(b)}{\leftrightarrow} P4_2/ncm$$

$$\text{case. 2} \quad F4/mmm \overset{(a)}{\leftrightarrow} Bmab \overset{(a)}{\leftrightarrow} Pccn \overset{(a)}{\leftrightarrow} P4_2/ncm,$$

where (a) and (b) denote that the two relevant space groups are and are not connected, respectively, by the relation between group and subgroup with respect to their symmetry elements. The *Bmab*-to-$P4_2/ncm$ transition should be of a first order because the two space groups are not linked by the group-subgroup relation, but all the other transitions could be of a second order.

1.1.3 Accessible site to and arrangement of excess oxygen atoms

It has been found by structural refinements of neutron diffraction data of both $La_2NiO_{4.18}$ powder crystal[12] and $La_2CuO_{4.032}$ single crystal[26] that an excess oxygen atom is located at $(\frac{1}{4}, \frac{1}{4}, \frac{1}{4})$ site which is surrounded tetrahedrally by four lanthanum atoms and four apical oxygen atoms, O(2) in Fig. 1.3, of two LaO planes as shown in Fig. 1.5. Thus, there are eight sites of excess oxygen atoms in the unit cell of $F4/mmm$ notation.

Long-range-ordered structures of the excess oxygen atoms have been suggested so far to exist. Hiroi *et al.*[27] first observed two types of homologous series of superstructures in $La_2NiO_{4+\delta}$ crystals by electron diffraction and transmission electron microscopy, and proposed that the superstructures are based on three-dimensional ordering of excess oxygen atoms. Demourgues *et al.*[28] have observed by an electron diffraction technique superlattice structures in $La_2NiO_{4.17}$ and $La_2NiO_{4.25}$ single crystals prepared by electrochemical oxidation technique. Tranquada *et al.*[29] have suggested one-dimensional ordering similar to the staging of intercalates in graphite in the vicinity of $\delta = 0.07$ and $\delta = 0.10$ on the basis of the obtained superlattice reflections by a neutron diffraction technique. Furthermore, Tranquada *et al.*[30] observed by neutron diffraction experiment of $La_2NiO_{4.125}$ crystal two types of superstructures below 300 K and suggested that order-disorder phase transition of excess oxygen atoms takes place at around 300 K from three-dimensionally

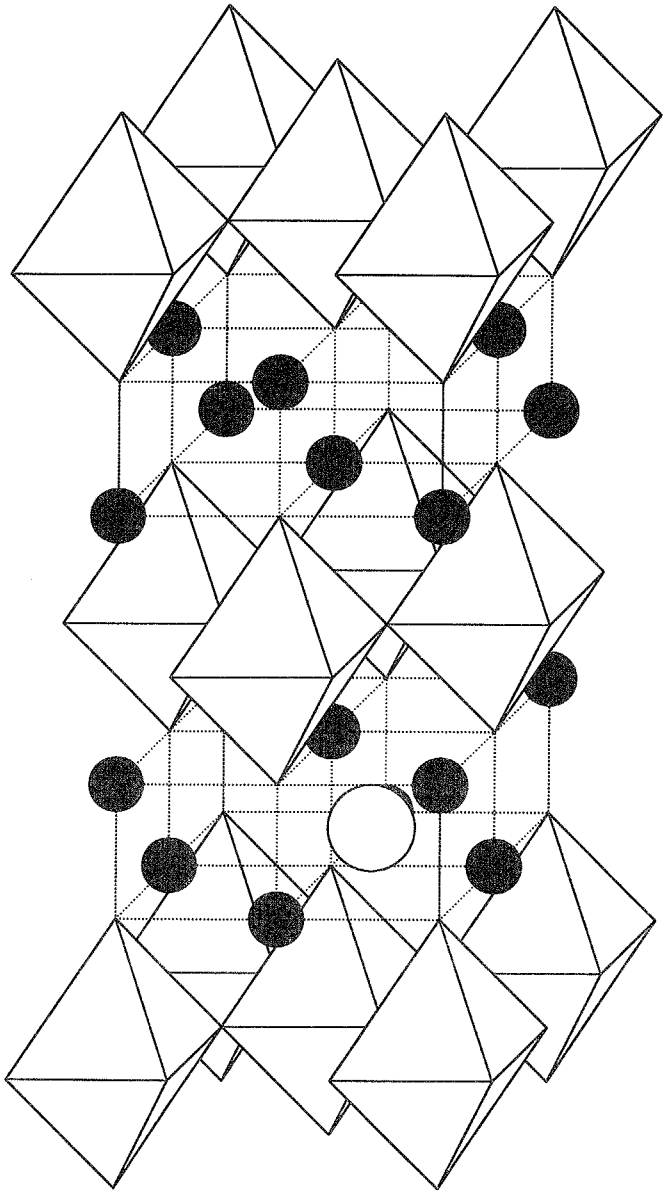

Figure 1.5: Interstitial site of excess oxygen atoms, represented by open circles, at ($\frac{1}{4}$, $\frac{1}{4}$, $\frac{1}{4}$) in $F4/mmm$ notation. There are eight equivalent sites in the unit cell of $F4/mmm$ notation.

ordered phase to disordered phase.

For the copper system, Radaelli *et al.*[31] have studied an electrochemically oxidized single crystal $La_2CuO_{4.1}$ using a neutron diffraction technique, and determined the space group to be $Fmmm$. Besides, they observed satellites around the several Bragg peaks as well as around the forbidden peaks of $Fmmm$ symmetry. They indicated that the appearance of satellites around the forbidden reflections is due to the distortion associated with the modulation which locally breaks $Fmmm$ symmetry, and furthermore suggested that the superstructure is due to the ordering patterns of the interstitial oxygen atoms and of the apical oxygen displacements spanning many fundamental unit cells. Wells *et al.*[32, 33] have observed by neutron diffraction technique superlattice peaks corresponding to stage-6, stage-4, stag-3 and stage-2 structures similar to those suggested by Tranquada *et al.* in electrochemically oxidized crystals, the excess oxygen composition of which were not determined.

1.1.4 Phase separation with respect to excess oxygen composition

Jorgensen *et al.*[12] first reported, from Reitveld refinement of neutron diffraction data of $La_2NiO_{4+\delta}$ crystals, the presence of phase separation into oxygen-rich and oxygen-poor phases the space groups of which were $Fmmm$ and $Bmab$, respectively. Systematic studies with variation of excess oxygen content have shown the presence of three phase separation regions so far.[15, 29, 34, 35] Hosoya *et al.*[34] reported by magnetic susceptibility measurements that the two phase separation regions of $0.01 < \delta < 0.02$ and $0.03 < \delta < 0.06$ appeared. Rice *et al.*[35] and Tamura *et al.*[15] also observed the appearance of the same phase separation regions by powder X-ray diffraction technique, and suggested that the space groups of three single phases formed in the ranges $0 < \delta < 0.01$, $0.02 < \delta < 0.03$, and $\delta > 0.06$ were $Bmab$, $Pccn$(or $P4_2/ncm$), and $I4/mmm$($Fmmm$ at low temperatures), respectively. Tranquada *et al.*[29] reported by neutron diffraction technique of single crystals that another phase separation occurred at around room temperature in the range $0.07 < \delta < 0.10$. The diffraction studies with variation of temperature[15, 29] have lead to a conclusion that the

phase separations in the ranges $0.03 < \delta < 0.06$ and $0.07 < \delta < 0.10$ were accompanied by structural phase transition in either of two phases present. Tranquada *et al.*[29] reported on the behavior in the range $0.07 < \delta < 0.10$ that only high-temperature phase existed above 290 K, that the high-temperature phase with $\delta \approx 0.07$ and the low-temperature phase with $\delta \approx 0.10$ coexisted in the temperature range 240-290 K, and that the high-temperature phase with $\delta \approx 0.07$ vanished and new low-temperature phase with $\delta \approx 0.07$ appeared and coexisted with the other low-temperature phase with $\delta \approx 0.10$ below 240 K. They also reported the similar stepwise anomalies in the range $0.03 < \delta < 0.06$.

For $La_2CuO_{4+\delta}$ system, there are still controversies concerning the phase separation region and the phase separation temperature. Jorgensen *et al.*[6] have first suggested a phase separation into oxygen-rich *Fmmm* and oxygen-poor *Bmab* phases below 320 K, based on the structural analysis using the neutron diffraction data. The similar phase separation phenomenon has been observed in $La_2CuO_{4.03}$ powder crystal by using detailed synchrotron X-ray and neutron diffraction techniques by Zolliker *et al.*,[36] and the separation temperature was determined to be 290 K. Further, Vaknin *et al.*[37] observed by the neutron scattering study of $La_2CuO_{4.03}$ single crystal that the linewidth of the (006) reflection begins to broaden abruptly at around 260 K, and concluded that phase separation occurs at $T_{ps} = 260 \pm 5$ K. Around 260 K, Hundley *et al.*[38] have also observed hysteresis phenomena in the magnetic susceptibility, resistivity, and thermoelectric power for $La_2CuO_{4.032}$ single crystal and suggested them to be due to slowness of oxygen diffusion in the crystal. Hammel *et al.*[39] observed in ^{139}La NMR study of $La_2CuO_{4.032}$ crystal two signals, one originating from oxygen-rich region and the other from oxygen-poor region, and found that the doublet signal based on the magnetic spin ordering originating from the oxygen-poor region vanished above 265 K. The above two research groups concluded that a phase separation occurs at around 265 K in $La_2CuO_{4.032}$ crystal. Ryder *et al.*[40] observed by using an electron microscopic technique for $La_2CuO_{4+\delta}$ polycrystal that a "herringbone" pattern with a very strong diffraction contrast of black-white "fringes" developed below room temperature. They have proposed a spinodal decomposition into $\delta \approx 0$ and $\delta \approx 0.05$ phases with a periodicity of $\sim$300 Å and determined the separation

temperature to be 280 K from the results of resistivity and Seebeck coefficient measurements. Wells *et al.*[32, 33] have proposed a phase diagram of $La_2CuO_{4+\delta}$ crystal with four phase separation regions on the basis of their neutron diffraction data. According to their phase diagram, the first phase separation occurs around room temperature in the range $0.01 < \delta < 0.055$, and the other three phase separations also occur around room temperature in the range $\delta > 0.055$ but the details of the composition ranges have not been clarified.

1.2 Topics on electronic property of $La_2MO_{4+\delta}$ (M = Ni, Cu) system

1.2.1 Antiferromagnetic ordering in stoichiometric crystals

Both the stoichiometric crystals of La_2NiO_4 and La_2CuO_4 are Mott-Hubbard insulators(in detailed reality, charge-transfer type insulators). The characteristic of La_2MO_4 crystal in the magnetic properties is two-dimensional antiferromagnetic nature in each MO_2 plane which is expected from the layered structure. The two-dimensional antiferromagnetic properties have been studied in detail in K_2NiF_4 crystal: Neutron diffraction experiments[41, 42] have disclosed that a three-dimensional antiferromagnetic phase transition occurs at around 97 K and is accompanied by two-dimensional critical scattering, and that the in-plane antiferromagnetic short-range-order remains up to rather high temperatures. These phenomena have been understood to be as follows: The two-dimensional antiferromagnetic short-range-order exists at rather high temperatures above the three-dimensional antiferromagnetic phase transition temperature, the correlation length within each NiF_2 plane and thus the effective exchange interaction of spins between the planes increase as the temperature decreases, and when the correlation length reaches a particular value, the three-dimensional ordering cooperatively occurs. The similar three-dimensional antiferromagnetic phase transitions have been reported to occur at 335 K and 315 K in La_2NiO_4[43] and La_2CuO_4,[44] respectively. There is, however, a difference between the two compounds. The three-dimensional antiferromagnetic phase transition

is and is not accompanied by two-dimensional critical scattering in nickel[45] and copper[46] crystals, respectively. Furthermore, the magnitude of in-plane nearest-neighbor M-M exchange interaction, J ~1300 K, for La_2CuO_4 crystal[47] is rather higher than that, J ~340 K, for La_2NiO_4 crystal.[48]

1.2.2 Annealing effect on superconductivity in $La_2CuO_{4+\delta}$ crystal below room temperature

Since the suggestion of phase separation with respect to excess oxygen composition by Jorgensen *et al.*,[6] most of research groups have related anomalies of superconductivity due to the effects of cooling rate and annealing time below room temperature to the freezing-in or -out of the diffusion of excess oxygen atoms concerning the phase separation as follows. Ahrens *et al.*[49] pointed out that the superconducting T_c of $La_2CuO_{4.032}$ crystal was sensitive to the cooling rate around 195 K, and the T_c of slowly cooled sample, ~33 K, was 4 K higher than that of rapidly cooled one, ~29 K. The result was explained as due to freezing-in of the phase separation process halfway in the non-equilibrium state, since the diffusion rate of excess oxygen atoms would become small as the temperature decreased. Then, metallic phase in the rapidly cooled sample has small δ than that in the slowly cooled one. The small δ, meaning dilute hole concentration, leads to lowering in the T_c. Kremer *et al.*[50, 51] have investigated the annealing effects at some temperatures on the Meissner fraction of $La_2CuO_{4.017}$ crystal, and suggested the freezing-in of the diffusion of hole clusters around 180 K in addition to that of excess oxygen atoms around 220 K. However, any of the research groups has not observed directly the phase separation with respect to excess oxygen composition and thus oxygen migration.

1.2.3 Charge stripe ordering in $La_2NiO_{4+\delta}$ crystal

It has been reported that holes doped into NiO_2 planes of $La_2NiO_{4+\delta}$ crystal tend to order themselves in periodically spaced stripes.[29, 30, 52, 53] The phenomenon is refered to as a charge stripe ordering. These charge stripes run diagonally in the square lattice defined by the Ni-O-Ni bond and thus along the a-axis of $F4/mmm$ notation as shown

in Fig. 1.6. In the essentially undoped regions between the stripes, the Ni spins can order antiferromagnetically, with the charge stripes acting as domain walls. The charge stripe ordering phenomena have been observed by neutron diffraction technique only in $La_2NiO_{4.125}$ and $La_2NiO_{4.133}$ crystals in addition to orderings of excess oxygen atoms and magnetic spins in NiO_2 plane.[29, 30, 52, 53] The orderings of excess oxygen atoms and magnetic spins have been reported to occur cooperatively near room temperature and at 110 K, respectively. It was reported that the superlattice peaks based on the order of holes start to be observed around 220 K with the periodicity commensurate to that of the order of excess oxygen atoms. Then, the intensity of the superlattice peaks increased exponentially with decreasing temperature, and the peak position and intensity changed discontinuously at 110 K.

1.3 Calorimetric appearance of a glass transition due to freezing-in of rearrangement motion of excess oxygen atoms

In the study on the oxygen nonstoichiometry of $La_{n+1}Ni_nO_{3n+1+\delta}$ and $La_2CuO_{4+\delta}$ crystals, it is indispensable to obtain the information on diffusion rate of excess oxygen atoms in the crystals in order to judge whether the crystal is in the equilibrium state or not with respect to positional arrangement of excess oxygen atoms. The information can be obtained by calorimetry as mentioned below.

The diffusion process of excess oxygen atoms is thermal activation process. The relaxation time taken for each excess oxygen atom to surmount a potential barrier, $\Delta\varepsilon_a$, is expressed by,

$$\tau = \tau_0 \exp(\Delta\varepsilon_a / RT). \tag{1.2}$$

where τ_0, R, and T are pre-exponetial factor, gas constant, and absolute temperatrure, respectively. As the temperature of the crystal decreases, the relaxation time becomes long, and when the time becomes longer than the experimental time scale(10^2-10^6s in the present calorimetric work), the positional arrangement of excess oxygen atoms is effec-

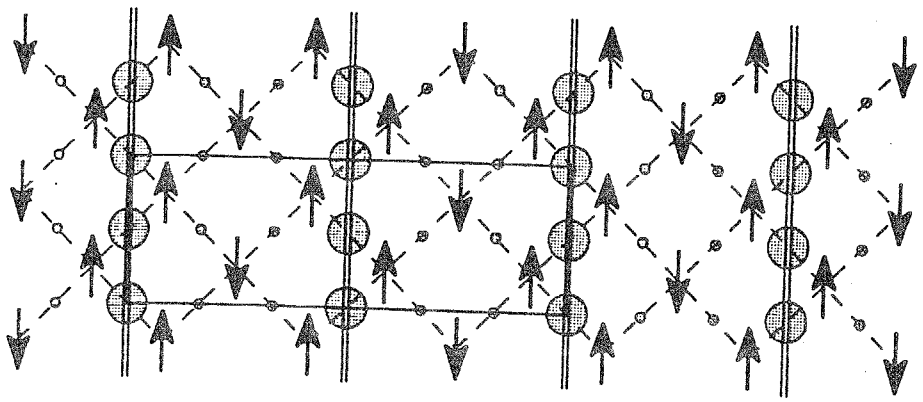

Figure 1.6: Model of spin and hole ordering in NiO_2 plane suggested by Tranquada *et al.*:[52] circles, positions of holes; arrows, correlated Ni moments. The double lines indicate positions of domain walls.

tively frozen in. A glass transition is such a freezing-in phenomenon, and the transition temperature, T_g, is often defined as the temperature at which the relaxation time becomes 10^3s. When the relaxation time is brought into the range of 10^2-10^6s, spontaneous enthalpy relaxation as an equilibration process of arrangement of excess oxygen atoms is observed on account of the crossing between the time scales of the rearrangement of excess oxygen atoms and the calorimetry.

The enthalpy relaxation due to the glass transition is observed as spontaneous heat evolution and absorption effects of a sample. If any spontaneous heat evolution or absorption effect appears in the sample, it is detected as a spontaneous temperature rise or fall, respectively, of the cell under adiabatic conditions. Figures 1.7 (a) and 1.7 (b) show a diagram illustrating how the configurational enthalpy follows in the cooling and heating processes in the glass transition region and how the temperature drift rates are observed in the heat capacity measurements on heating under adiabatic condition, respectively, for a rapidly precooled sample, A, and a slowly precooled one, B. The upper-right to lower-left thick solid line in Fig. 1.7 (a) represents the equilibrium enthalpy curve concerning the degree of freedom with respect to positional arrangement of excess oxygen atoms. When the sample is precooled rapidly, the excess oxygen atoms are arrested in the state corresponding to that at a relatively high temperature such as T_1. As the temperature increases in the course of heat capacity measurements, the enthalpy starts to relax appreciably toward the equilibrium value at around the temperature at which the relaxation time becomes $\sim 10^6$ s. The rates of exothermic relaxations first observed become large with reduction in the relaxation times at higher temperatures, and then become small as the enthalpy approaches the equilibrium value as shown in the figures. After crossing of the enthalpy with the equilibrium line at T_1', endothermic relaxations appear till the relaxation time becomes shorter than $\sim 10^2$ s at higher temperatures such as T_3. When the sample is precooled slowly or is annealed for a long time at low temperatures around T_2, on the other hand, the enthalpy of the sample is brought to a very low value corresponding, for example, to T_2 in the figure. As the temperature increases for measurements, a small exothermic effect starts to appear at around the temperature at which the relaxation time

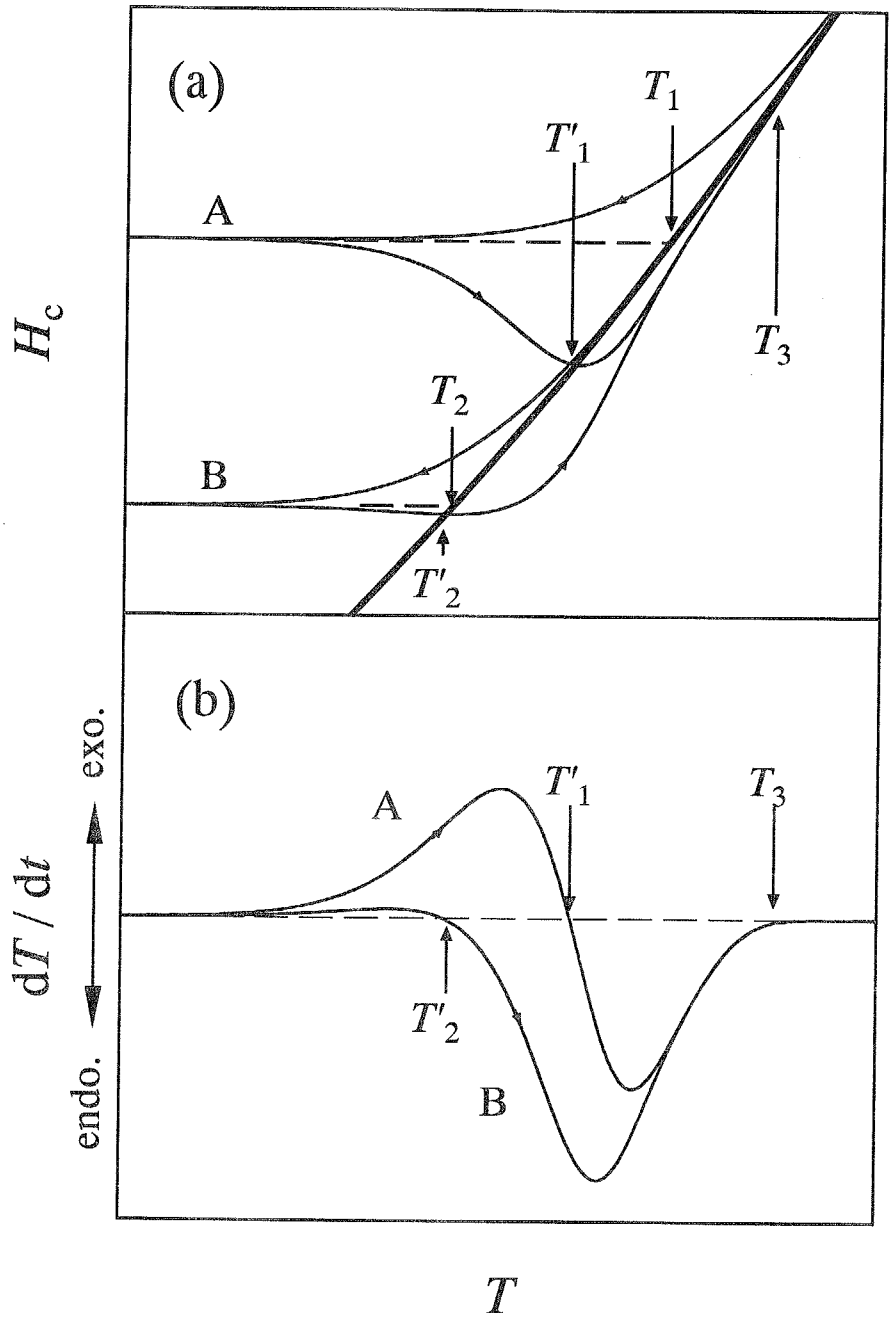

Figure 1.7: (a) Schematic configurational enthalpy vs. temperature relation in a glass transition temperature region: A, rapidly precooled sample; B, slowly precooled sample. Thick solid line stands for the equilibrium configurational enthalpy, and thin solid lines for the paths along which the sample, when cooled and heated continuously, follows. (b) Temperature drift rate curves observed on heating the samples A and B.

becomes $\sim 10^6$ s. A following endothermic effect starts to appear at T_2' which is definitely lower than the T_1' in the above case of rapidly precooled sample, and is considerably large compared with that in the rapidly precooled case.

1.4 Aim of the present study

Layered perovskite oxides constructed by stacking perovskite layers and rock-salt layers with a certain periodicity show nonstoichiometry with respect to oxygen composition, giving rise to oxygen-deficient site(vacancy) or interstitial excess oxygen. These oxides are attractive with the interesting electronic properties such as superconductivity in copper oxides, colossal magnetoresistance in manganese oxides, and so on. The fraction of oxygen vacancies is often large and the vacancies are arranged in the ordered way. On the other hand, the ordering processes and the ordered arrangements of intetstitial excess oxygen atoms have not been clarified yet. The dynamic properties of nonstoichiometric oxygen atoms in oxide are interesting themselves, and, of course, indispensable in order to judge whether the crystal is in equilibrium state or not. But, there is no study on the dynamic property of oxygen atoms in nonstoichiometric oxides.

$La_{n+1}Ni_nO_{3n+1+\delta}$ crystals are a typical homologous series of layered perovskite oxides, and can be synthesized easily for $n = 1$, 2, 3, and ∞. This series of crystals are thus the best for the systematic study on the oxygen nonstoichiometry of layered perovskite oxides. $La_2NiO_{4+\delta}$ crystal is insulator with respect to electric conductivity but, on the other hand, $La_3Ni_2O_{7+\delta}$[1] and $La_4Ni_3O_{10+\delta}$[2] crystals are metallic. Because $La_2CuO_{4+\delta}$ crystal is also metallic, the comparison between $La_2CuO_{4+\delta}$ and $La_2NiO_{4+\delta}$ crystals are interesting, for example, to clarify the role of electronic energy to the stability of various phases such as oxygen ordered phase.

Unsolved problems on the phase relation, crystallography, and interrelation between crystal structure and electronic properties of $La_{n+1}Ni_nO_{3n+1+\delta}$ and $La_2CuO_{4+\delta}$ crystals are collected in the following. Many research groups have reported that phase separation with respect to excess oxygen composition and order-disorder phase transition of excess

oxygen atoms occurred at some temperature in $La_2NiO_{4+\delta}$ and $La_2CuO_{4+\delta}$ crystals as stated in sections 1.1.3 and 1.1.4. However, there is no evidence so far indicating that the excess oxygen atoms really rearrange at those temperatures. It is unclear whether the phase separations occuring in $La_2NiO_{4+\delta}$ crystals are of a eutectoid, a peritectoid or any other type, and the phase relation is not clarified in the range $\delta > 0.10$ at all. The positional arrangement of excess oxygen atoms in $La_2NiO_{4+\delta}$ crystals as stated in section 1.1.3 is doubtful because the analysis did not take scattering from excess oxygen atoms themselves into account. As concerned with the annealing effect reported around 200 K on the superconductivity in $La_2CuO_{4+\delta}$ crystal as stated in section 1.2.2, it is unclear whether the annealing effect is due to freezing-in or -out of diffusion of excess oxygen atoms or not, because no direct evidence has been given for the freezing-in or -out process. There is no understanding for the reason why a charge stripe ordering in $La_2NiO_{4+\delta}$ crystal as stated in section 1.2.3 appears only around $\delta = 0.13$. There is no study on the oxygen nonstoichiometry and phase relation of $La_3Ni_2O_{7+\delta}$ and $La_4Ni_3O_{10+\delta}$ crystals at all.

The first aim of the present study on $La_{n+1}Ni_nO_{3n+1+\delta}$ and $La_2CuO_{4+\delta}$ crystals is to clarify the phase relations as a function of excess oxygen content and temperature, the second to clarify the ordering process of excess oxygen atoms, the third to clarify the dynamic properties of excess oxygen atoms, and the fourth to clarify the electronic properties in relation to the phase relation.

The format of thesis is as follows. In Chapter 2, the method of sample preparation and the experimental techniques are mentioned. The results of adiabatic calorimetry and magnetometry are shown in Chapter 3. Most of the crystals showed glass transition phenomenon due to freezing-in of excess oxygen atoms. Particularly, $La_2NiO_{4+\delta}$ crystals showed glass transition phenomena indicating the presence of phase separation with respect to excess oxygen composition as discussed in section 4.3. Order-disorder phase transitions with respect to positional arrangement of excess oxygen atoms were observed in $La_2NiO_{4+\delta}$ crystals but, on the other hand, such a transition was not observed both in $La_3Ni_2O_{7+\delta}$ and $La_2CuO_{4+\delta}$ crystals. In $La_2CuO_{4+\delta}$ crystals, many structural phase transitions of a displacive type were observed in the nonstoichiometric region and the

correlation between superconductivity and the phase transitions(but not phase separation) was discovered. In $La_2CuO_{4.05}$ and $La_2CuO_{4.07}$ crystals, it was indicated that an order-disorder process on the arrangement of excess oxygen atoms occurs above 400 K. In section 4.1, phase relation, ordering process of excess oxygen atoms, and magnetic and electronic properties in $La_2NiO_{4+\delta}$ crystals are discussed. In section 4.2, phase relation, antiferromagnetic ordering, and correlation between superconductivity and structural phase transitions are discussed. In subsection 4.2.4, potential reasoning for the difference between some features of phase transitions in $La_2NiO_{4+\delta}$ and $La_2CuO_{4+\delta}$ crystals is discussed. In section 4.3, dynamic properties and freezing-in processes of excess oxygen atoms are discussed in $La_2NiO_{4+\delta}$, $La_3Ni_2O_{7+\delta}$, and $La_2CuO_{4+\delta}$ crystals. In Chapter 5, some concluding remarks of the present study are mentioned in relation to the chemistry and physics of nonstoichiometric layered perovskite oxides.

Chapter 2

Experiment

2.1 Preparation of samples

Powder crystals were used for the present study of crystalline $La_2NiO_{4+\delta}$, $La_3Ni_2O_{7+\delta}$, and $La_4Ni_3O_{10+\delta}$ corresponding to $n = 1$, 2, and 3 in $La_{n+1}Ni_nO_{3n+1+\delta}$ series. The powder sample of $La_2NiO_{4+\delta}$ crystal was prepared by a usual method. La_2O_3(99.9% purity) and NiO(99.9% purity) crystals were dried by calcining at about 1200 K in air. Appropriate amounts of the crystals were mixed in an agate mortar, and heated in air to 1527 K with intermittent mixing of several times. The powder samples of $La_3Ni_2O_{7+\delta}$ and $La_4Ni_3O_{10+\delta}$ crystals were prepared by sol-gel method using citric acid as follows, because impurity phases remains when the samples were prepared by the usual method. After La_2O_3 crystal was dried by calcining at about 1200 K in air, appropriate amount of La_2O_3 and $Ni(NO_3)_2{\cdot}6H_2O$(99.9% purity) crystals were disolved into water by adding nitric acid until La_2O_3 crystal is completely disolved. Then, citric acid was added into the solution as the whole charge of the citric ions is about twice of the charge of sum of Ni^{2+} and La^{3+} ions in the solution. The solution was heated with a gas burner for dehydration of the solution to enhance the polymerization of citric acid. After the polymerization, the gel was fired in a furnace at around 423-473 K, then heated to 1573 K, and kept there for a day to react. The samples of $La_{n+1}Ni_nO_{3n+1+\delta}$ crystals as prepared by the above methods were confirmed each to be a single phase by X-ray powder diffractometry.

Single crystals and powder crystal were used for the present calorimetries of crys-

talline $La_2CuO_{4+\delta}$ in the ranges $\delta \leq 0.035$ and $\delta \geq 0.05$, respectively. La_2O_3 and CuO(99.9% purity) powders were dried by calcining at about 1200 K in air. Appropriate amounts of the powders were mixed with ethanol in an agate mortar, and heated in air to 1123 K with intermittent mixing of several times. Single crystals were grown by Traveling Solvent Floating Zone (TSFZ) method[54, 55] as follows. There is a coexistent region composed of La_2CuO_4 solid phase and a liquid phase of La_2O_3-CuO in the phase diagram,[56] and such a liquid phase can be used as the solvent for single crystal growth by zone levelling technique. The crystal growth apparatus is an infrared radiation furnace (Nichiden Machinery Ltd.) equipped with an ellipsoidal mirror and a 750 W halogen lamp as the heat source. One of the foci of the ellipsoid is occupied by the lamp and the other by a sample; the solvent rod was attached to the top of the lower shaft located just below the focus and the feed rod was suspended at the bottom of the upper shaft located just above it. The light produced by the halogen lamp is focused and cast on the top of the solvent rod from every direction, the rod is dissolved into the molten zone between two rods, and $La_2CuO_{4+\delta}$ solid phase precipitates from it on to the feed rod as it passes this zone. The state of the sample is able to be examined from the enlarged figure image of the molten zone projected on the screen through the lens, and the intensity of the halogen lamp is controlled to be in the desired state. The growth region is isolated by a fused quartz tube and the atmosphere in the region can be controlled to prevent the molten sample from evaporation. La_2CuO_4 powder and La_2O_3-CuO mixed powder with the solvent composition of 78 mol% CuO were formed into a cylindrical shape 6 mm in diameter by 80 mm in length, and compressed at hydrostatic pressure of about 250 MPa. These rods were sintered at 1373 K for 12 h in oxygen atmosphere and were then used as the feed and the solvent rod, respectively. Growth conditions involve growth rate of 1.0 mmh^{-1}, counter-rotation rate of each shaft of 30 $rmin^{-1}$, and growth atmosphere of 0.2 MPa O_2 to prevent the melt from evaporation of CuO.

2.2 Adjustment of excess oxygen composition

Table 2.1 shows the values of excess oxygen compositions determined by an iodometric titration technique described in the next section with uncertainty of about ± 0.003, together with the quantities of the samples used for the present calorimetry.

Adjustment of the excess oxygen composition of $La_2NiO_{4+\delta}$ crystals in the range $\delta \leq 0.073$ was carried out by annealing at 1473 K for a day under different oxygen partial pressure using mixed gases of CO_2 and H_2 or of CO_2 and O_2 to achieve the desired oxygen pressure.[8] After the sample was quenched to room temperature in the atmosphere, the sample was annealed in an evacuated and sealed quartz tube at around 700 K for a few days and then cooled slowly down to room temperature in the furnace in order to homogenize the oxygen content in the crystal. Adjustment of the excess oxygen composition of $La_2NiO_{4+\delta}$ crystal in the range $\delta \geq 0.098$ was carried out by annealing at respectively different temperatures in air for a day, and then the sample was quenched into liquid nitrogen. Because the cooling rate is very rapid, the samples are considered to be homogeneous with respect to excess oxygen content. It was found that there is a linear relation between δ and the annealing temperature as shown in Fig. 2.1. Adjustment of the excess oxygen compositions of $La_3Ni_2O_{7.094}$ and $La_4Ni_3O_{10.00}$ crystals was carried out by annealing at 573 K for a day. It was found that oxygen nonstoichiometry of $La_3Ni_2O_{7+\delta}$ is smaller than $La_2NiO_{4+\delta}$ crystal and that $La_4Ni_3O_{10+\delta}$ crystal shows no appreciable oxygen nonstoichiometry. Thus, calorimetry of $La_4Ni_3O_{10+\delta}$ crystal was not carried out.

Adjustment of the excess oxygen compositions of $La_2CuO_{4+\delta}$ ($\delta = 0$, 0.011) samples was also carried out in the same procedure as that of nickel system. $La_2CuO_{4.035}$ sample was prepared by thermal treatment at 873 K under pure oxygen gas pressure of 600 atm for a week. For $La_2CuO_{4.05}$ and $La_2CuO_{4.07}$ samples, the oxygen adjustment was carried out by an electrochemical oxidation technique first reported by Wattiaux *et al.*[10, 11] as follows: An electrochemical cell of the type, La_2CuO_4|1 N KOH aq.|Pt, was used for oxidation. A Ag/AgCl electrode was used as a reference electrode connected to the solution via the salt bridge. The La_2CuO_4 pellet was polished to a thickness of 2 mm, and Pt wire was attached

Table 2.1: Excess oxygen contents, masses, and quantities of samples

δ	mass(g)	quantiy(mol)
	$La_2NiO_{4+\delta}$	
0.047	14.184	0.035350
0.062	20.614	0.051344
0.067	31.227	0.077763
0.073	24.809	0.061764
0.098	19.705	0.049009
0.116	30.955	0.076934
0.123	18.653	0.046346
0.126	17.755	0.044110
0.131	17.066	0.042389
0.141	16.228	0.040293
0.150	22.928	0.056907
0.154	13.292	0.032986
	$La_3Ni_2O_{7+\delta}$	
0.091	15.079	0.023286
	$La_2CuO_{4+\delta}$	
0.002	8.7692	0.021634
0.011	11.235	0.027705
0.035	9.0097	0.022196
0.05	21.217	0.052239
0.07	11.861	0.029181

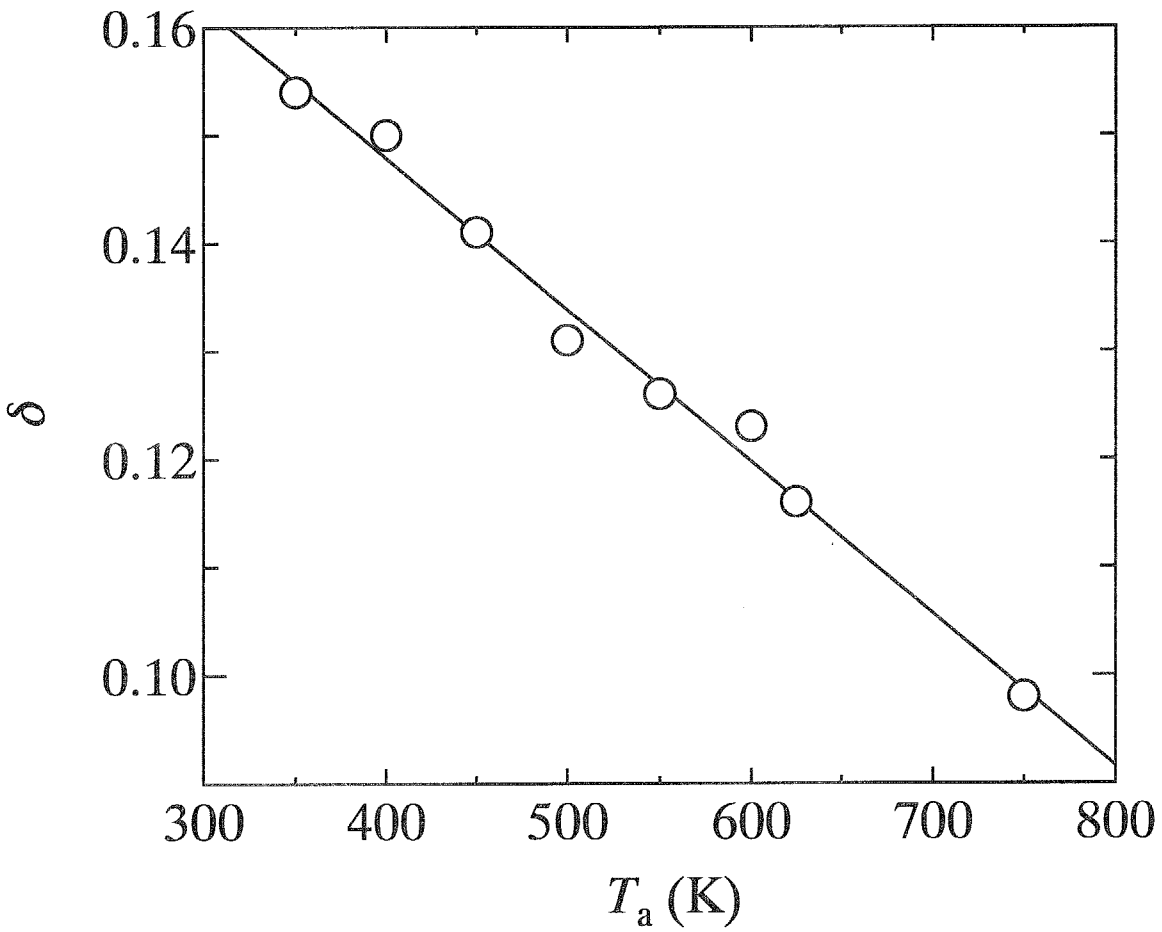

Figure 2.1: Excess oxygen contents of the $La_2NiO_{4+\delta}$ crystals prepared by annealing at temperature, T_a. Solid line in the figure was obtained by fitting a straight line to the data.

by silver paste and fixed by epoxy resin. The electrochemical oxidation experiment was carried out at room temperature under both a constant potential and a constant current using a HOKUTO HA-301 potentio-galvanostat. The amount of electricity passing the cell was measured by a HOKUTO HF-201 coulombmeter. After the oxidation process, the sample pellet was washed and rinsed with distilled water and evacuated under vacuum at 10^{-3} Torr for 24 h.

2.3 Chemical analysis of excess oxygen composition

The formal valence of copper or nickel atoms, p, was determined by iodometric titration technique as follows. The excess oxygen compositions were calculated from the values of p assuming that excess oxygen atoms are incorporated as O^{2-} species in the crystal and on the basis of the fact that the valence numbers of the other oxygen atoms and lanthanum atoms are -2 and $+3$, respectively. The formula is thus written as $La^{3+}_{n+1}M^{p+}_{n}O^{2-}_{3n+1+\delta}$, and the relation between excess oxygen composition, δ, and the formal valence of M atom, p, is then represented by

$$p = 3 - \frac{1}{n} + \frac{2\delta}{n}. \tag{2.1}$$

Concentration of sodium thiosulfate standard solution was determined by titration of KIO_3 of $\sim$10 mg dried at about 80 °C in air. $La_2NiO_{4+\delta}$ sample of $\sim$0.2 g was dissolved into a 6N HCl solution with excess KI of $\sim$3 g; then the following reaction rapidly occurred.

$$Ni^{p+} + (p-2)I^- \rightarrow Ni^{2+} + \frac{p-2}{2}I_2. \tag{2.2}$$

After the sample was completely dissolved, acetic acid and sodium acetate buffer solution were added in order to prevent iodide ion from air-oxidation, and then the solution was titrated with $\sim$0.002 mol% and 0.02 mol% sodium thiosulfate solution for $La_2NiO_{4+\delta}$ crystal and for $La_3Ni_2O_{7+\delta}$ and $La_4Ni_3O_{10+\delta}$ crystals, respectively, using starch as an indicator. Since the air-oxidation of iodide ion always occurs during dissolving the sample, a 6N HCl blank solution with the same amounts of KI and buffer solution as the sample solution but without a sample was titrated, after the same duration as in the case with

the sample, in order to estimate a volume for correction due to air-oxidation of iodide ion, and a value derived by subtracting it from the titration volume for the sample solution was used as the titration volume due to the sample itself for calculation of p value.

$La_2CuO_{4+\delta}$ crystal of ~0.2 g was also dissolved into a 6N HCl solution with excess KI of ~3 g, and then the following reaction rapidly occurred.

$$Cu^{p+} + pI^- \rightarrow CuI \downarrow + \frac{p-1}{2} I_2. \tag{2.3}$$

Differing from the nickel ions in the nickel system, copper ions are reduced to Cu^+, and any Cu^+ ion in the solution precipitates out as CuI. The same titration procedures as for the nickel sample were taken for the sample and the blank solutions.

2.4 Principle of calorimetry and evaluation procedure of heat capacity

Figure 2.2 shows a cryostat of an adiabatic calorimeter used in the present study.[57] The adiabatic condition was so prepared as to minimize the heat leak between a calorimeter cell (A) and its surroundings. For this preparation an innermost shield (B) surrounding the cell is always kept in principle at the same temperature as the cell, while the space around the cell is exhausted to 10^{-4} Pa to prevent a heat leakage by convection.

For controlling the temperatures of the calorimeter cell (A) and innermost shield (B), outer adiabatic shields (C)-(E) were controlled at adequately low temperatures referred to that of the shield (B). The calorimeter cell is made of copper and gold plated, and has vanes for help of heat conduction within the cell. Equilibration of the temperature within the cell after heating off is achieved within 5 ~ 6 min and the imprecision of the thermometry is within the order of 10^{-5} K.

Calorimetry was carried out in the temperature range of 13-500 K by the intermittent heating method[58] schematically described in Fig. 2.3: The temperature is rated with a resistance thermometer fixed on the bottom of the sample vessel until the temperature of the calorimeter cell is equilibrated, for example, for 13 min, some known quantity of

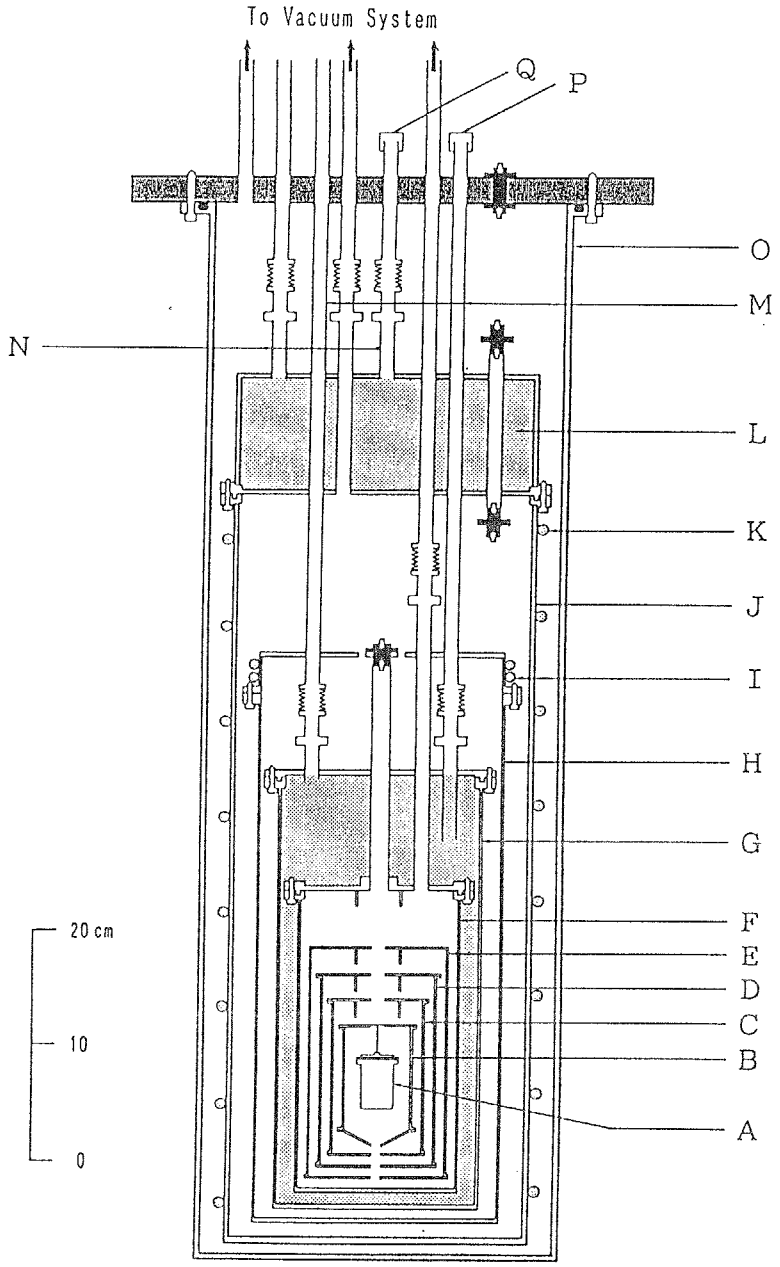

Figure 2.2: Schematic drawing of a cryostat: (A), calorimeter cell; (B), (C), (D), and (E), adiabatic shields; (F), inner vacuum jacket; (G), liquid helium tank; (H), floating radiation shield; (I), spiral tube for cold helium gas; (J), middle vacuum jacket; (K), spiral tube for cold nitrogen gas; (L), liquid nitrogen tank; (M), liquid helium inlet and gas outlet; (N), liquid nitrogen inlet and gas outlet; (O), outer vacuum jacket; and (P), and (Q), caps.

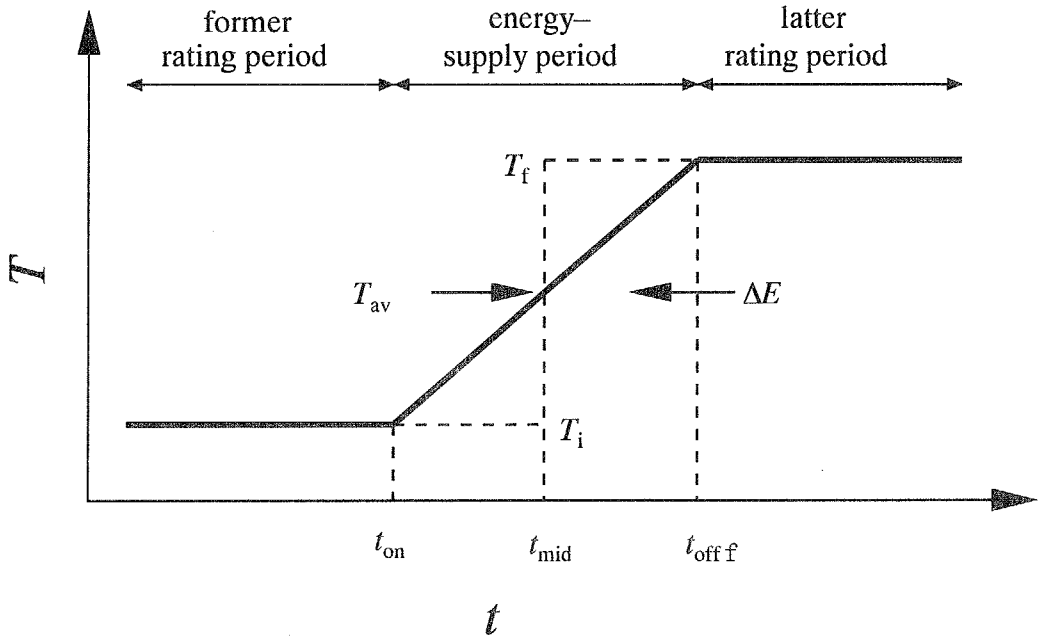

Figure 2.3: Schematic diagram showing a procedure of heat capacity determination.

electrical energy, ΔE, is supplied into a calorimeter cell loaded with the sample through the heater wire (about 100 Ω) wound on the outside wall of the sample vessel, and again the temperature is rated for 13 min. The initial temperature, T_i, and the final one, T_f, are estimated by extrapolating temperature drift data to a middle point of energy-supply period, t_{mid}, in terms of a straight line. The gross heat capacity of the cell, C_{total}, at $T_{av} = (T_f + T_i)/2$ is evaluated to be

$$C_{total} = \frac{\Delta E}{T_f - T_i}. \tag{2.4}$$

The latter temperature drift serves as the former temperature drift for determination of T_i of the next set of a heat capacity measurement. If any spontaneous heat evolution or absorption effect appears in the sample, it is detected as a spontaneous temperature rise or fall, respectively, of the cell in the above rating periods. All the spontaneous temperature drift rates in the present study were taken as the values at 10 min after each energy supply.

Net heat capacity of a sample is given by

$$C_{net} = C_{total} - C_{cell} + C_{He}. \tag{2.5}$$

where C_{cell} is heat capacity of the cell filled only with helium gas of 0.1 MPa at room temperature, and C_{He} is heat capacity of helium gas excluded from the cell by existence of sample. The heat capacity of the cell, C_{cell}, was measured in advance, and the heat capacity of helium gas, C_{He}, was evaluated assuming that the gas is ideal gas.

A platinum resistance thermometer (Minco Products S1059, U. S. A.), which had a nominal resistance of 100 Ω at 0 °C was used after the temperature scale was transferred from the other thermometer calibrated on the ITS-90. The imprecision and inaccuracy of the measurements with the apparatus were estimated previously to be less than ±0.04% and ±0.4%, respectively.[57]

2.5 Magnetic susceptibility measurement

Magnetic susceptibility measurements of $La_2CuO_{4+\delta}$ crystals were carried out in order to determine the antiferromagnetic and the superconducting phase transition temperatures. The experiments were performed using a Quantum Design MPMS-2 SQUID magnetometer. The measured magnetic susceptibilities of samples were corrected by subtracting the contribution due to the orbital diamagnetism of relevant ions from the raw data. The annealing effects of superconductivity as stated in section 1.2.2 were also investigated in $La_2CuO_{4.011}$ crystal by the magnetic susceptibility measurements.

Chapter 3

Results

3.1 $La_2NiO_{4+\delta}$ system

3.1.1 Heat capacities of stoichiometric crystal

Experimental molar heat capacities of $La_2NiO_{4.00}$ crystal are tabulated in Table 3.1 and shown graphically in Fig. 3.1 in the temperature range 14-500 K. Three heat capacity anomalies were observed at around $T_2 = 80$ K, $T_1 = 150$ K, and $T_N = 330$ K, due to a first-order structural phase transition reported before,[23, 59, 60] a second-order phase transition, and a three-dimensional antiferromagnetic phase transition, respectively, as described below.

Lattice molar heat capacities at constant pressure, $C_{p,m}^{lat}$, as represented by a solid line in Fig. 3.1, were calculated in order to estimate excess molar heat capacities due to the phase transitions. The solid line in Fig. 3.1, representing lattice molar heat capacity curve at constant volume, $C_{v,m}^{lat}$, was first evaluated from the phonon density of states obtained by inelastic neutron scattering measurements,[61] and a $(C_{p,m}^{lat} - C_{v,m}^{lat})$ correction term was calculated according to the following equation;

$$C_{p,m}^{lat} - C_{v,m}^{lat} = A\, C_{p,m}^{lat\ 2}\, T. \tag{3.1}$$

Here constant A was determined from the structural and other data at 300 K as follows. The correction term can be estimated by using formally a thermodynamic relation;

$$C_{p,m}^{lat} - C_{v,m}^{lat} = T\left(\frac{\partial p}{\partial T}\right)_v \left(\frac{\partial v}{\partial T}\right)_p = BV_m\alpha^2 T, \tag{3.2}$$

Table 3.1: Molar heat capacities of $La_2NiO_{4.00}$; R=8.31451 $JK^{-1}mol^{-1}$

$\frac{T_{av}}{K}$	$\frac{C_{p,m}}{R}$	$\frac{T_{av}}{K}$	$\frac{C_{p,m}}{R}$	$\frac{T_{av}}{K}$	$\frac{C_{p,m}}{R}$
14.09	0.1242	57.48	4.442	110.60	9.847
14.95	0.1525	58.79	4.605	112.92	10.04
15.88	0.1894	60.11	4.756	115.28	10.24
16.86	0.2323	61.42	4.900	117.66	10.43
17.94	0.2854	62.74	5.051	120.09	10.62
19.13	0.3512	64.18	5.229	122.54	10.81
20.39	0.4294	65.78	5.410	125.03	11.00
21.71	0.5227	67.43	5.599	127.55	11.19
23.03	0.6258	69.02	5.793	130.10	11.38
23.97	0.6937	70.57	5.974	132.69	11.57
24.62	0.7504	72.13	6.163	135.31	11.75
25.68	0.8433	73.69	6.354	137.96	11.93
27.03	0.9711	75.02	6.524	140.65	12.10
28.41	1.108	76.11	6.680	143.37	12.28
29.89	1.253	77.21	6.824	146.12	12.47
31.36	1.408	78.34	6.958	148.91	12.65
32.85	1.561	79.48	7.074	151.73	12.81
34.40	1.730	80.63	7.174	154.57	12.97
36.05	1.913	81.80	7.263	157.43	13.14
37.54	2.080	83.27	7.398	160.32	13.30
38.90	2.235	84.37	7.477	163.24	13.46
40.25	2.390	85.69	7.601	166.18	13.62
41.60	2.548	85.74	7.600	169.15	13.77
42.94	2.703	87.49	7.764	171.91	13.92
44.28	2.862	89.30	7.934	174.46	14.05
45.61	3.021	91.14	8.107	177.05	14.18
46.94	3.181	93.27	8.296	179.67	14.31
48.26	3.338	95.33	8.491	182.32	14.44
49.58	3.497	97.41	8.685	185.14	14.57
50.90	3.655	99.52	8.877	187.85	14.72
52.22	3.814	101.67	9.070	190.59	14.85
53.53	3.971	103.85	9.263	193.36	14.97
54.85	4.128	106.07	9.460	196.17	15.09
56.16	4.280	108.32	9.653	199.00	15.21

(to be continued)

Table 3.1: (continued)

$\frac{T_{\mathrm{av}}}{\mathrm{K}}$	$\frac{C_{p,\mathrm{m}}}{R}$	$\frac{T_{\mathrm{av}}}{\mathrm{K}}$	$\frac{C_{p,\mathrm{m}}}{R}$	$\frac{T_{\mathrm{av}}}{\mathrm{K}}$	$\frac{C_{p,\mathrm{m}}}{R}$
201.86	15.34	301.77	18.57	401.10	20.42
204.76	15.46	304.67	18.65	404.10	20.45
207.68	15.58	307.57	18.72	407.12	20.54
210.64	15.70	310.47	18.81	410.16	20.54
213.62	15.82	313.38	18.88	413.21	20.55
216.64	15.94	316.28	18.96	416.27	20.59
219.68	16.06	319.19	19.04	419.35	20.59
222.76	16.17	322.09	19.12	422.44	20.64
225.86	16.28	325.00	19.20	425.54	20.66
228.99	16.40	327.91	19.29	428.66	20.66
232.15	16.54	330.83	19.37	431.79	20.74
235.35	16.64	333.74	19.39	434.95	20.79
238.56	16.73	336.66	19.39	438.10	20.81
241.81	16.83	339.58	19.42	441.25	20.85
245.08	16.98	342.51	19.43	444.42	20.86
248.34	17.07	345.43	19.44	447.61	20.92
251.60	17.16	348.36	19.53	450.81	20.92
254.87	17.26	351.30	19.58	454.03	20.92
258.12	17.36	354.42	19.65	457.26	20.97
261.38	17.44	357.36	19.69	460.51	20.97
264.63	17.55	360.30	19.76	463.78	21.00
267.84	17.65	363.31	19.80	467.06	21.01
270.75	17.72	366.18	19.87	470.34	21.08
273.66	17.80	369.04	19.93	473.65	21.04
276.57	17.87	372.00	19.95	476.96	21.07
279.48	17.96	376.32	20.04	480.28	21.10
282.39	18.05	380.67	20.10	483.61	21.11
285.30	18.12	385.04	20.19	486.94	21.15
288.21	18.21	389.43	20.25	490.28	21.18
291.12	18.30	393.85	20.33	493.62	21.20
294.03	18.37	398.28	20.37	496.98	21.21
296.94	18.44	395.12	20.35	500.33	21.20
299.85	18.52	398.10	20.37		

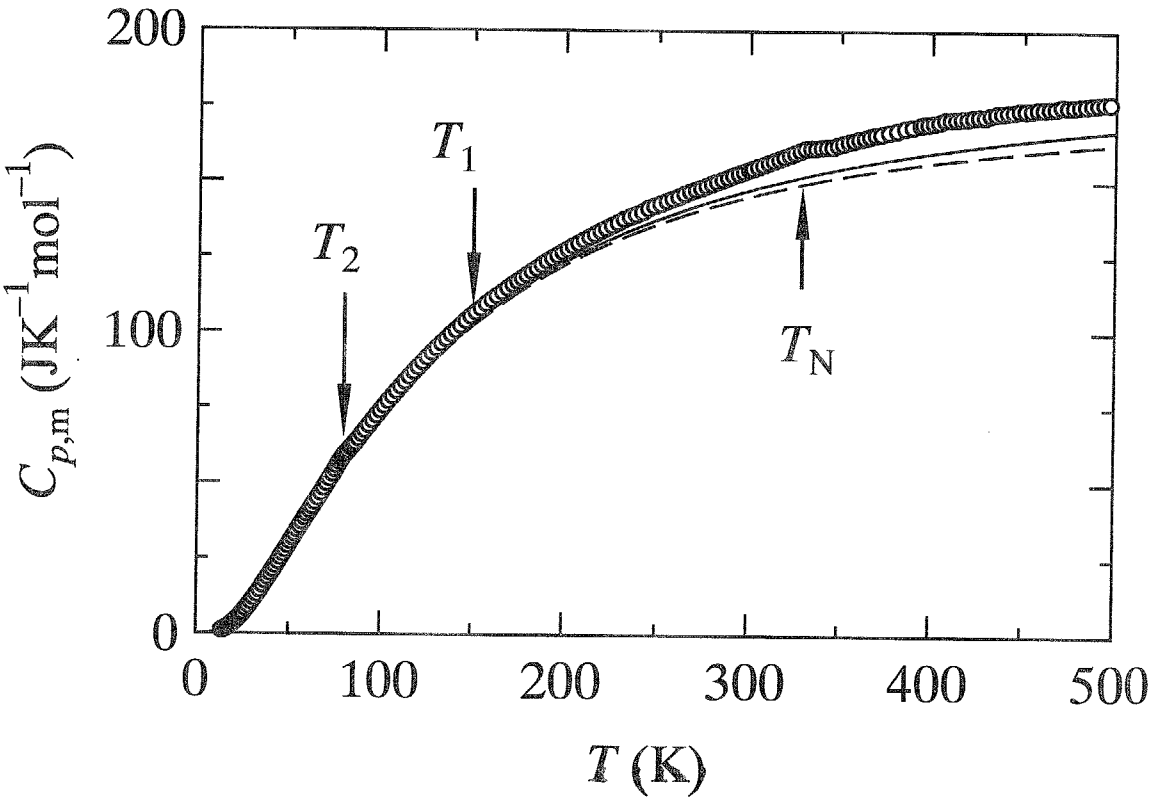

Figure 3.1: Experimental heat capacities of $La_2NiO_{4.00}$ crystal. Dashed and solid lines represent calculated lattice heat capacities at constant volume and at constant pressure, respectively. See text for detail.

where B, $V_{\rm m}$ and α are bulk modulus, molar volume, and volume thermal expansion coefficient, respectively. Bulk modulus $B = 1.13 \times 10^{-5}$ Jcm^{-3} was taken from the result of Brill *et al.*,[62] and $V_{\rm m} = 57.21$ cm^{3}mol^{-1} and $\alpha = 3.31 \times 10^{-5}$ K^{-1} were calculated from the data of temperature dependence of the unit cell volume obtained by Hayashi *et al.*[24] $C_{v,\rm m}^{\rm lat}$ at 300 K was derived from the phonon density of states as mentioned above to be $C_{v,\rm m}^{\rm lat}(300\ {\rm K}) = 145.16$ JK^{-1}mol^{-1}, and thus $C_{p,\rm m}^{\rm lat}$ at 300 K was evaluated to be

$$C_{p,\rm m}^{\rm lat}(300\ {\rm K}) = 147.29\ {\rm JK^{-1}mol^{-1}}. \tag{3.3}$$

Substituting the evaluated $C_{p,\rm m}^{\rm lat}$ and $C_{v,\rm m}^{\rm lat}$ values into Eq. (3.1) resulted in $A = 3.26 \times 10^{-7}$ J^{-1}mol^{-1}.

Figure 3.2 shows excess heat capacities of $La_2NiO_{4.00}$ crystal obtained by subtracting the solid line values in Fig. 3.1 from the experimental heat capacities. The heat capacity anomaly at around 150 K is demonstrated to exist definitely. The solid line in the figure stands for a base line, obtained by smoothly interpolating the values in the ranges of 14-40 K and of 200-300 K, to the structural phase transitions at T_1 and T_2. Figure 3.3 shows the excess heat capacities on an enlarged scale. The total entropy of the transitions was estimated to be 0.8 JK^{-1}mol^{-1}. No appreciable spontaneous temperature drift nor sharp heat-capacity peak were observed at around T_1 in the heat capacity measurements on heating. The phase transition at T_1 was thus determined to be of a second order.

Circles in Fig. 3.4 represent excess heat capacities, due mainly to antiferromagnetic ordering of spins, for the normalization of the three-dimensional antiferromagnetic phase transition temperature, 330 K, on an enlarged scale. The transition point was determined as the temperature of the small heat-capacity peak, and was rather close to the literature values by Yamada *et al.*[43] The heat capacity curve showed a wide tail on the low temperature side of the transition, and is expected to do on the high temperature side as well with showing a hump a little above the transition temperature.

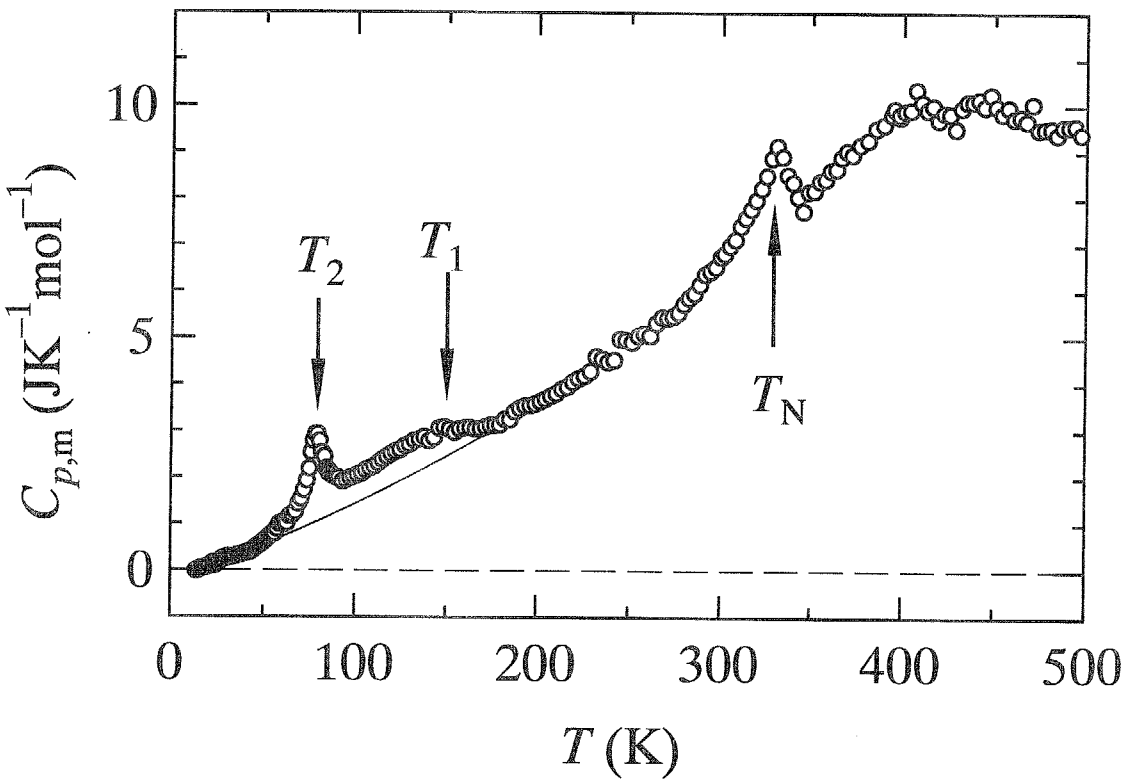

Figure 3.2: Excess heat capacities of $La_2NiO_{4.00}$ crystal as referred to the values of solid line in Fig. 3.1. A solid line represents the base line to the contribution from the structural phase transitions at T_1 and T_2. The baseline was drawn by linking smoothly the values in the ranges of 14-40 K and 200-300 K.

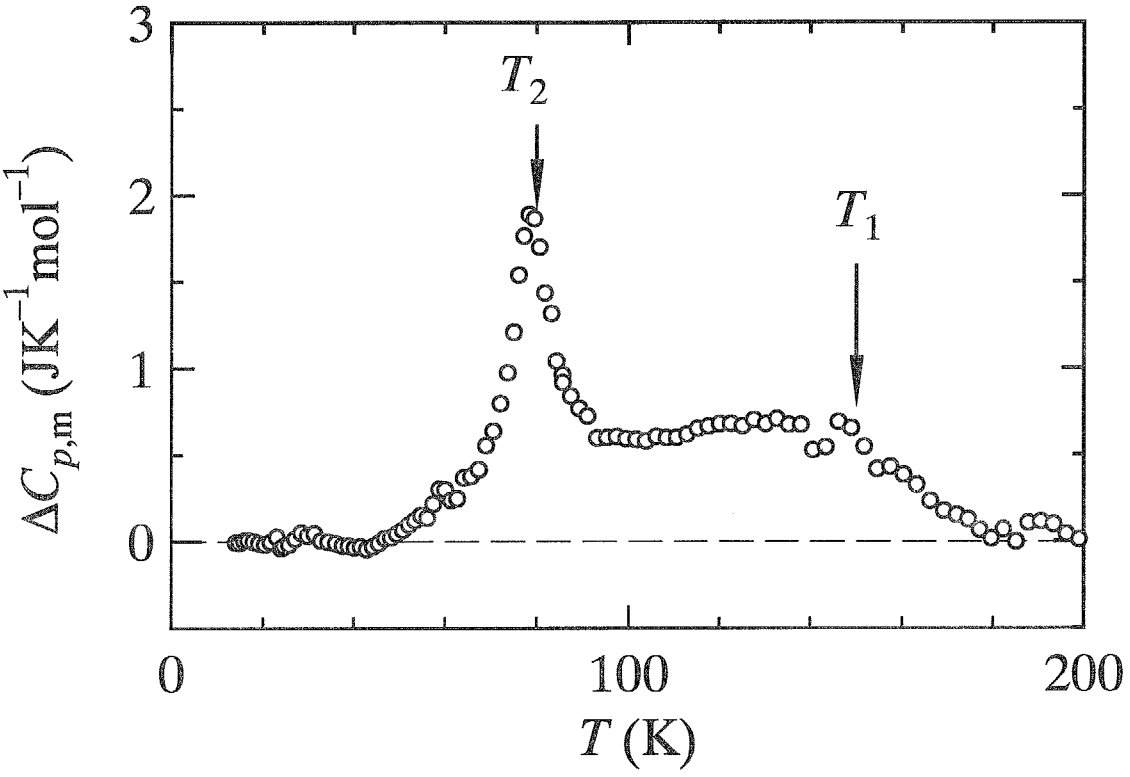

Figure 3.3: The assessed heat capacities due to the structural phase transitions at T_1 and T_2 on an enlarged scale.

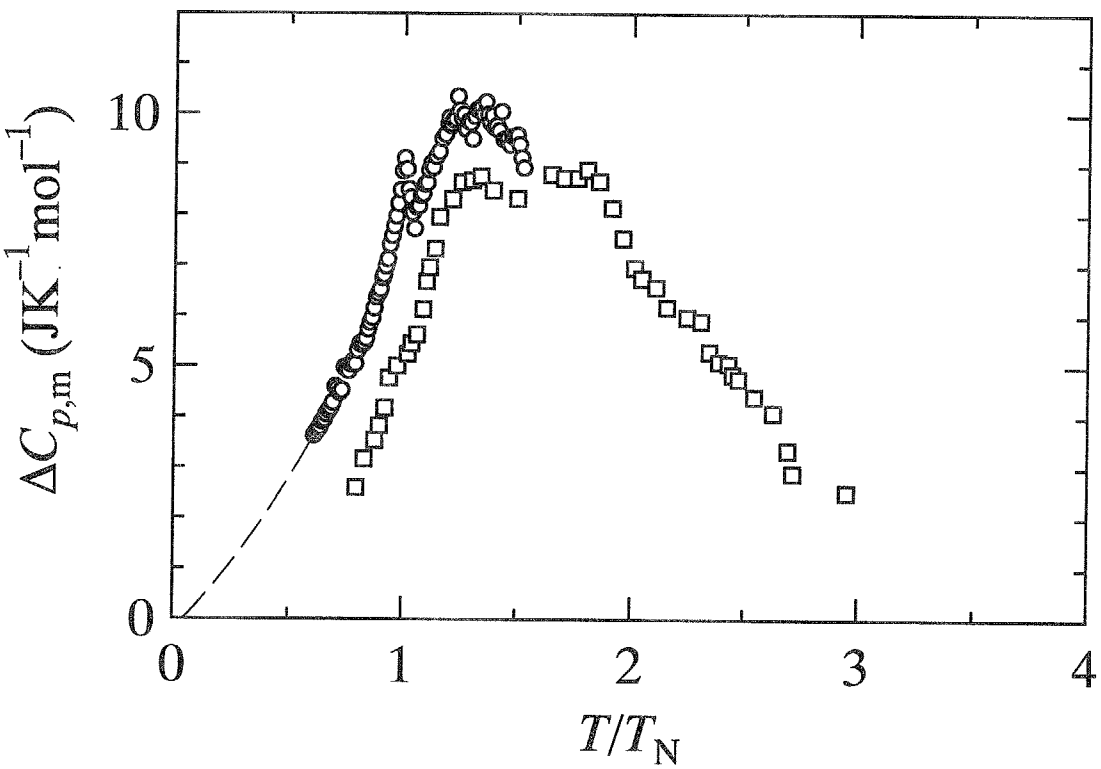

Figure 3.4: Excess heat capacities due to magnetic contribution: ○, the present result; □ , the result of K_2NiF_4 by Salamon *et al.*[78]

3.1.2 Standard thermodynamic functions of stoichiometric crystal

Standard thermodynamic functions of a $La_2NiO_{4.00}$ crystal were evaluated with the obtained heat capacity data according to the following basic equations;

$$\Delta_0^T H_{\rm m}^\circ = H(T) - H(0) = \int_0^T C_{p,{\rm m}} dT, \tag{3.4}$$

$$\Delta_0^T S_{\rm m}^\circ = S(T) - S(0) = \int_0^T C_{p,{\rm m}}/T dT, \tag{3.5}$$

$$\Phi_{\rm m}^\circ = \Delta_0^T S_{\rm m}^\circ - \Delta_0^T H_{\rm m}^\circ/T. \tag{3.6}$$

Here $H(0)$ and $S(0)$ denote the lattice energy at zero Kelvin and the residual entropy, respectively, and were taken to be zero in this evaluation. Heat capacity values below 13 K were estimated by extrapolating the values below 20 K in terms of an odd-order polynomial function as follows:

$$C_{p,{\rm m}}/({\rm JK^{-1}mol^{-1}}) = 2.134 \times 10^{-4}(T/{\rm K})^3 + 1.051 \times 10^{-6}(T/{\rm K})^5 - 1.354 \times 10^{-9}(T/{\rm K})^7. \tag{3.7}$$

The evaluated values are tabulated in Table 3.2.

3.1.3 Spontaneous temperature drift-rates and heat capacities observed in the heat capacity measurements of nonstoichiometric crystals

3.1.3.1 The samples precooled rapidly from high temperature to 90 K

Figures 3.5(a) and 3.5(b) show spontaneous temperature-drift rates observed during the heat capacity measurements of $La_2NiO_{4+\delta}$ crystals. Open circles in the figures represent values obtained on heating the samples precooled rapidly at 20 $Kmin^{-1}$ from 300 K (400 K for $\delta = 0.150$ and 0.154 crystals) to 90 K. All the samples showed complex heat evolution and absorption phenomena. The complex phenomena are understood to be superposition of two contributions: One is a glass transition due to freezing-in of rearrangement motion of excess oxygen atoms and the other is a positional phase transition/separation of excess oxygen atoms. The glass transition penomenon was clearly demonstrated in $\delta = 0.126$

Table 3.2: Standard thermodynamic functions of $La_2NiO_{4.00}$; R=8.31451 $JK^{-1}mol^{-1}$

$\frac{T}{K}$	$\frac{C^\circ_{p,m}}{R}$	$\frac{\Delta_0^T H^\circ_m}{R \cdot K}$	$\frac{\Delta_0^T S^\circ_m}{R}$	$\frac{\Phi^\circ_m}{R}$ [a]
0	0	0	0	0
10	0.0367	0.0832	0.0108	0.0025
20	0.4047	1.854	0.1196	0.0268
30	1.267	9.872	0.4329	0.1038
40	2.362	27.89	0.9437	0.2464
50	3.546	57.39	1.597	0.4493
60	4.736	98.85	2.350	0.7021
70	5.898	152.0	3.167	0.9952
80	7.117	217.3	4.037	1.321
90	8.001	292.8	4.925	1.672
100	8.918	377.4	5.815	2.042
110	9.799	471.0	6.707	2.425
120	10.62	573.1	7.595	2.819
130	11.37	683.1	8.475	3.220
140	12.07	800.4	9.344	3.627
150	12.70	924.3	10.20	4.037
160	13.28	1054	11.04	4.448
170	13.82	1190	11.86	4.860
180	14.33	1331	12.66	5.271
190	14.81	1476	13.45	5.681
200	15.26	1627	14.22	6.089
210	15.67	1781	14.98	6.494
220	16.07	1940	15.72	6.896
230	16.44	2103	16.44	7.296
240	16.79	2269	17.14	7.691
250	17.11	2438	17.84	8.083

[a] $\Phi^\circ_m/R = (\Delta_0^T S^\circ_m - \Delta_0^T H^\circ_m/T)/R$

(to be continued)

Table 3.2: (continued)

$\frac{T}{\mathrm{K}}$	$\frac{C^\circ_{p,\mathrm{m}}}{R}$	$\frac{\Delta^T_0 H^\circ_{\mathrm{m}}}{R \cdot \mathrm{K}}$	$\frac{\Delta^T_0 S^\circ_{\mathrm{m}}}{R}$	$\frac{\Phi^\circ_{\mathrm{m}}{}^a}{R}$
260	17.41	2611	18.51	8.472
270	17.71	2787	19.18	8.856
280	17.97	2965	19.83	9.236
290	18.26	3146	20.46	9.612
298.15	18.47	3296	20.97	9.916
300	18.52	3330	21.08	9.984
310	18.79	3517	21.70	10.35
320	19.06	3706	22.30	10.72
330	19.34	3898	22.89	11.08
340	19.42	4092	23.47	11.43
350	19.54	4287	24.03	11.78
360	19.75	4483	24.58	12.13
370	19.94	4681	25.13	12.48
380	20.11	4882	25.66	12.82
390	20.26	5084	26.19	13.15
400	20.39	5287	26.70	13.48
410	20.52	5491	27.21	13.81
420	20.63	5697	27.70	14.14
430	20.73	5904	28.19	14.46
440	20.82	6112	28.67	14.78
450	20.90	6320	29.14	15.09
460	20.98	6530	29.60	15.40
470	21.05	6740	30.05	15.71
480	21.11	6951	30.49	16.01
490	21.16	7162	30.93	16.31
500	21.20	7374	31.35	16.61

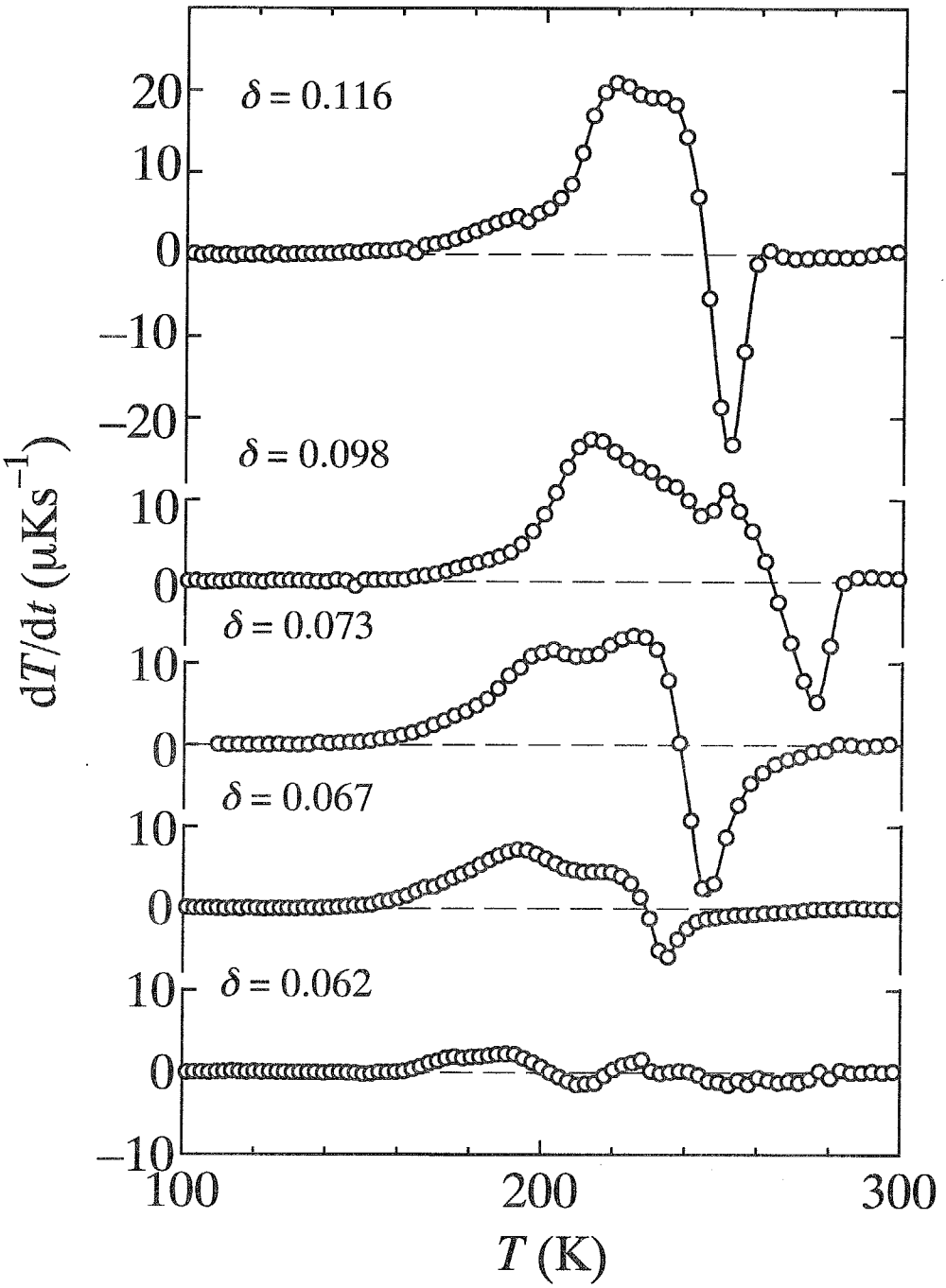

Figure 3.5(a): Spontaneous temperature-drift rates observed during the heat capacity measurements of $La_2NiO_{4+\delta}$ crystals($0.062 \leq \delta \leq 0.116$) precooled rapidly at 20 $Kmin^{-1}$ from high temperature to 90 K.

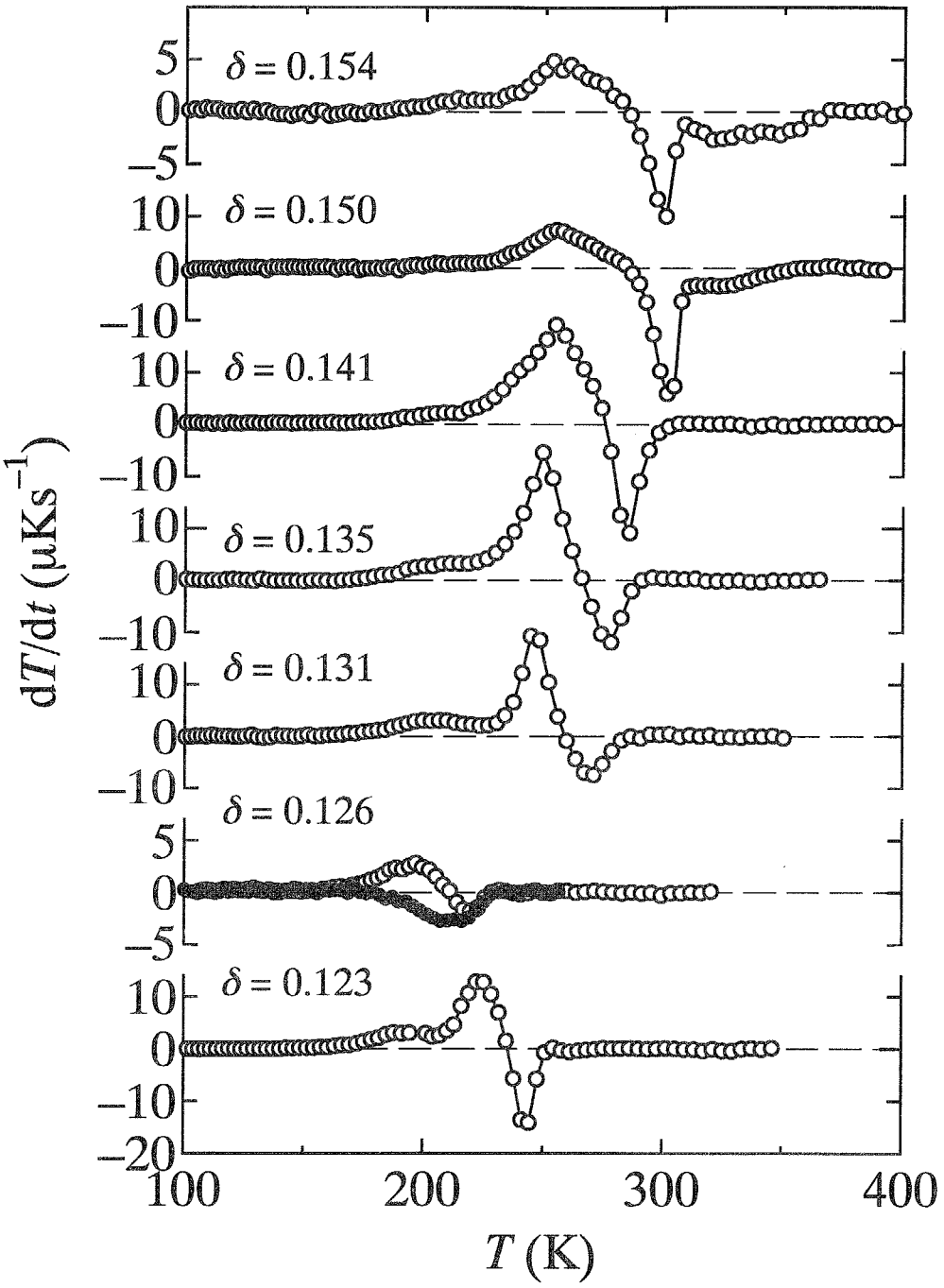

Figure 3.5(b): Spontaneous temperature-drift rates observed during the heat capacity measurements of $La_2NiO_{4+\delta}$ crystals($0.123 \leq \delta \leq 0.154$): ○, samples precooled rapidly at 20 $Kmin^{-1}$ from high temperature to 90 K; ●, sample precooled slowly at 20 $mKmin^{-1}$ from 210 K to 150 K.

crystal, because no phase transition/separation occurred in the crystal, the reason of which is discussed in the next chapter. The sample of $\delta = 0.126$ crystal precooled rapidly from 300 K showed heat evolution effect from 150 K to 220 K and then heat absorption effect up to 230 K as represented by open circles in Fig. 3.5(b), and the sample precooled at 20 $mKmin^{-1}$ from 210 K to 150 K, on the other hand, showed heat absorption effect from 150 K to 230 K as represented by solid circles. In addition, heat capacity jump was clearly observed around 220 K as shown in Fig. 3.7(b) and 3.9(b). These are characteristic of glass transition phenomenon. In the same way, the heat evolution(and absorption in $\delta = 0.062$ crystal) effect observed in the heat capacity measurements of the other crystals mainly in the range 150-220 K must be due to a glass transition occurring in the supercooled high-temperature phases. As stated in the next subsection, heat evolution effect in the range 200-280 K is due to (supercooled meta-stable)-to-(low-temperature stable) phase transition, and heat absorption effect above 230 K to (low temperature)-to-(high temperature) phase transition.

3.1.3.2 The samples transformed into low-temperature stable phases

Based on the results of the samples precooled rapidly as described above, heat capacity measurements were carried out after the samples were annealed at around 230-240 K for a few days to be transformed completely to the low-temperature stable phases after precooling to 100 K for enhancement of nucleation of the low-temperature phases. The completion of the phase transformation was judged by confirming that the heat evolution due to the transformation vanished completely. Figures 3.6(a) and 3.6(b) show spontaneous temperature-drift rates observed during the heat capacity measurements of $La_2NiO_{4+\delta}$ crystals which were subjected to stabilization to the low-temperature phases. No heat evolution effect due to transformation of the supercooled high-temperature to low-temperature phases was observed as seen from the figures. Figures 3.7(a) and 3.7(b) show the molar heat capacities, including the result of $\delta = 0.047$ crystal, obtained in the measurements.

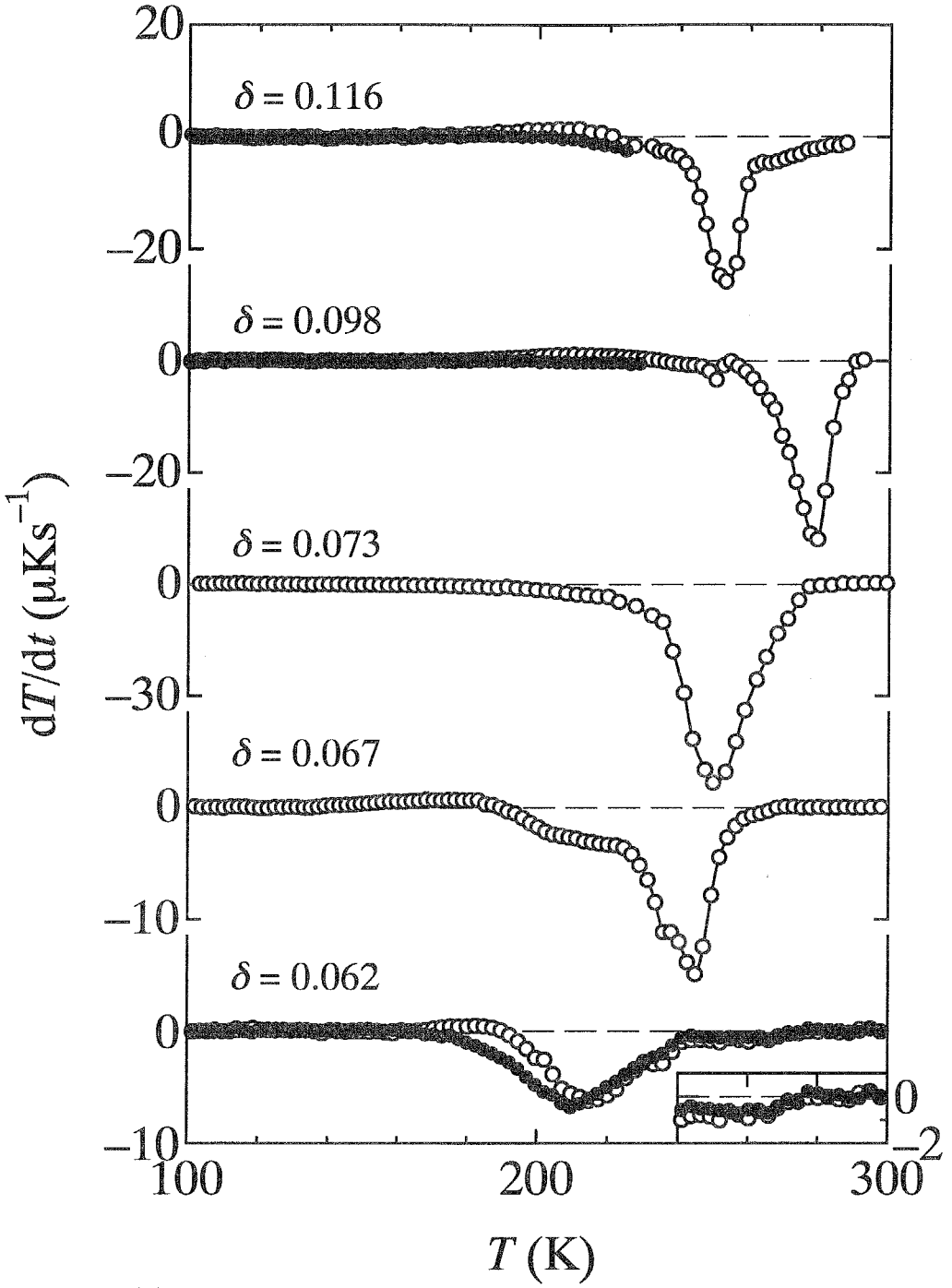

Figure 3.6(a): Spontaneous temperature-drift rates observed during the heat capacity measurements of $La_2NiO_{4+\delta}$ crystals($0.062 \leq \delta \leq 0.116$) transformed completely to each low-temperature stable state beforehand. The transformation was achieved by annealing the crystals at around 230 K for a few days. Inset in the bottom-right portion shows the results of $\delta = 0.062$ crystal on an enlarged scale.

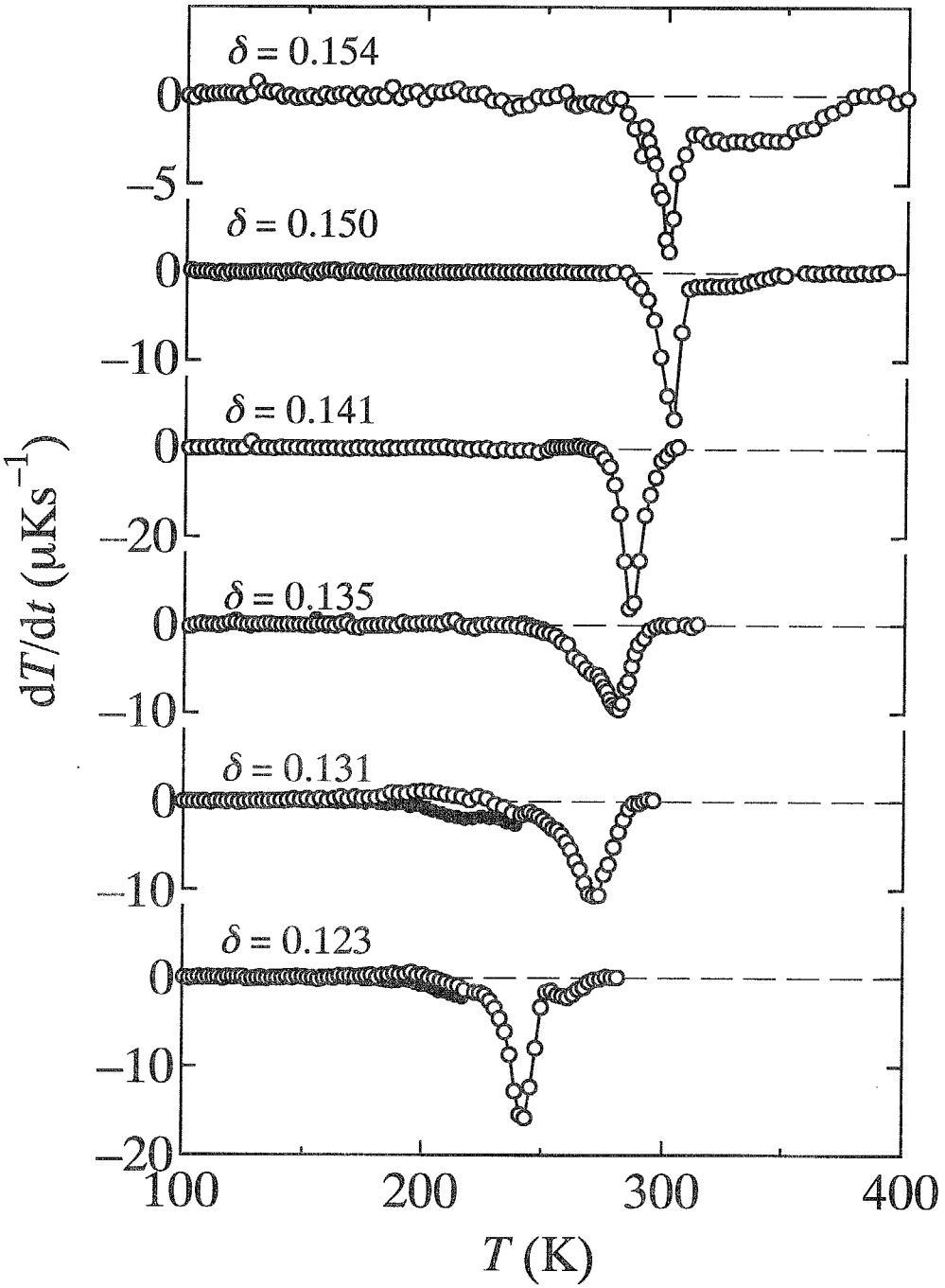

Figure 3.6(b): Spontaneous temperature-drift rates observed during the heat capacity measurements of $La_2NiO_{4+\delta}$ crystals($0.123 \leq \delta \leq 0.154$) transformed completely to each low-temperature stable state beforehand. The transformation was achieved by annealing the crystals at around 230 K for a few days.

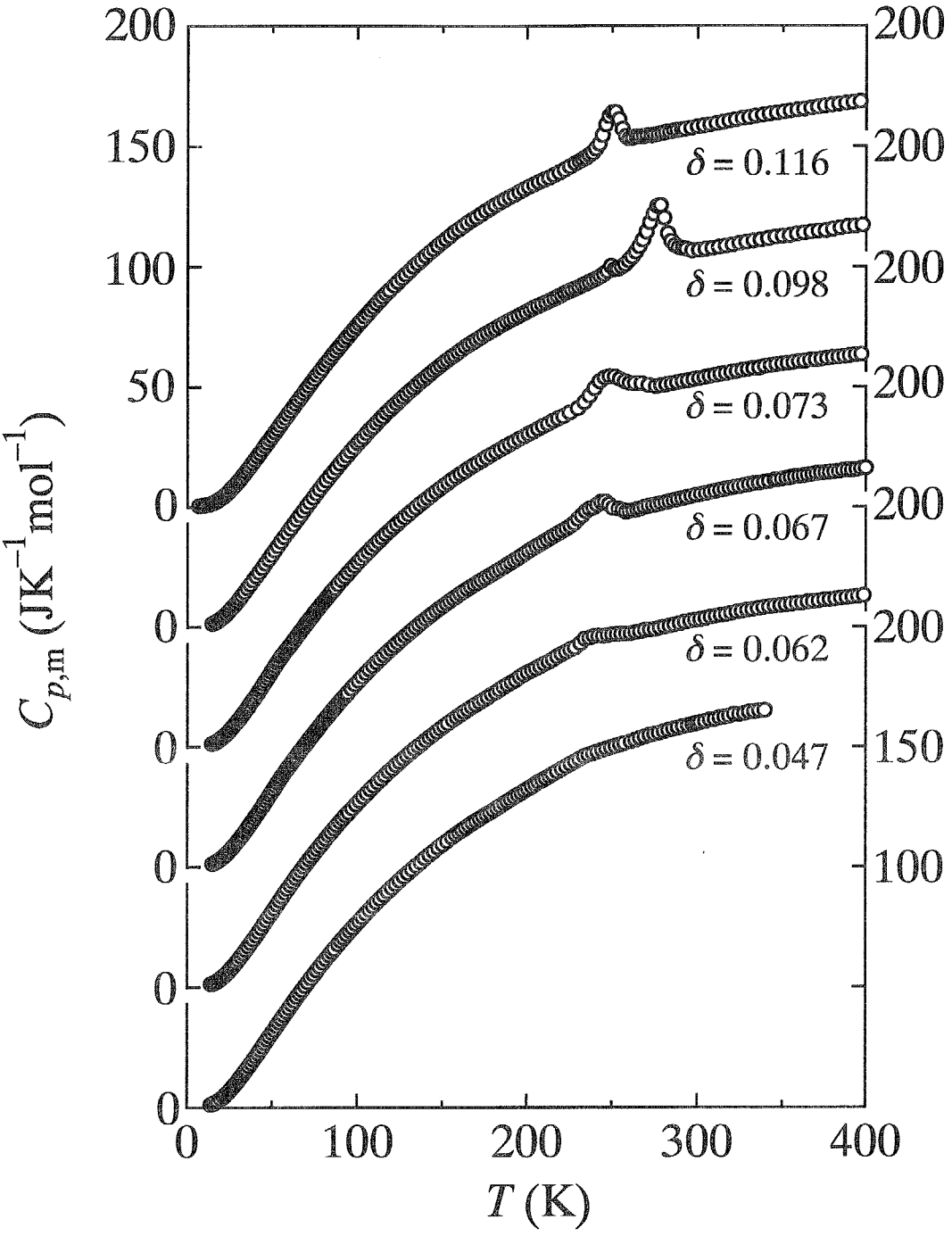

Figure 3.7(a): Molar heat capacities of $La_2NiO_{4+\delta}$ crystals with $0.047 \leq \delta \leq 0.116$. The origins of ordinate are shifted for clarity upwards by 50 $JK^{-1}mol^{-1}$ in the order of increasing δ.

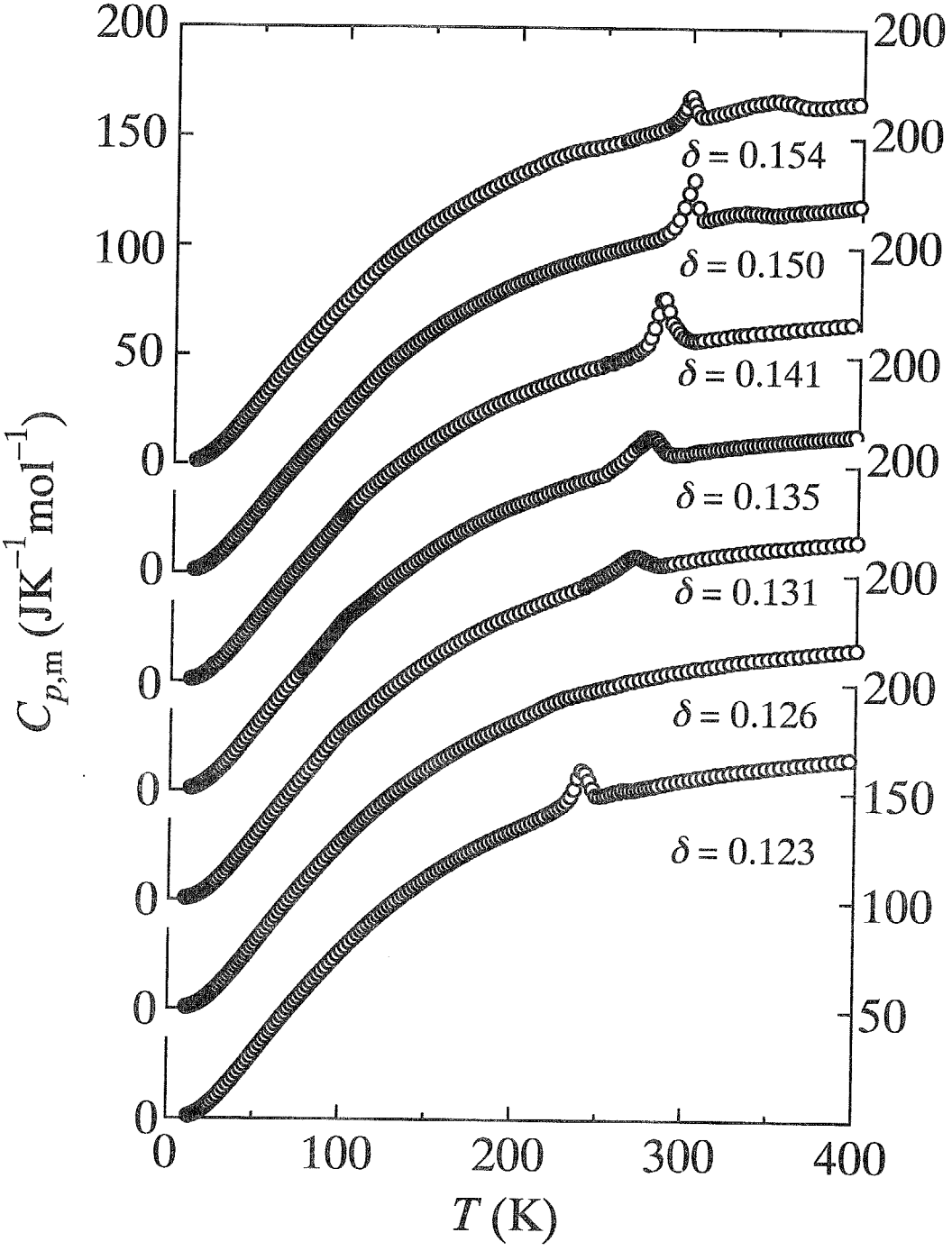

Figure 3.7(b): Molar heat capacities of $La_2NiO_{4+\delta}$ crystals with $0.123 \leq \delta \leq 0.154$. The origins of ordinate are shifted for clarity upwards by 50 JK^{-1}mol^{-1} in the order of increasing δ.

3.1.3.2.1 Glass transition phenomena Anomalous spontaneous heat evolution and absorption effects as shown in Fig. 3.6(a) and 3.6(b) are attributed to a glass transition and phase transitions roughly below and above 230 K, respectively. Open circles for δ = 0.062 crystal in Fig. 3.6(a) represent the results of the sample which was precooled at the rate of 20 mKmin^{-1} in the range 231-204 K and then cooled down to 90 K at the rate of 4 Kmin^{-1}. There appeared heat evolution effect from 160 K to 195 K and heat absorption effect above 195 K. Solid circles for δ = 0.062 crystal, on the other hand, represent the results of the sample precooled slowly at 20 mKmin^{-1} in the range 233-167 K and then cooled down to 90 K at the rate of 2 Kmin^{-1}. Heat evolution was hardly observed and heat absorption effect appeared above 160 K. Such dependence of heat evolution and absorption effects on the precooling rates is characteristic of a glass transition.

The results for δ = 0.098, 0.116, 0.123, and 0.131 crystals, which are plotted in Fig. 3.8 on enlarged scales, indicate the similar dependence: Open circles represent the results in the measurements in which the samples were precooled from 230 K to 90 K rather rapidly at 5 Kmin^{-1}. Heat evolution was observed around the ranges 160-230 K for the respective crystals. Solid circles, on the other hand, stand for the results in the measurements in which the samples were precooled slowly at 20 mKmin^{-1} in the range 240-150 K. Rather only heat absorption effect was observed above around 180 K for the respective crystals. The observation that the heat evolution effect in the low-temperature region below 220 K for the rapidly precooled sample changed to heat absorption effect for the slowly precooled sample is just characteristic of a glass transition as in the case of δ = 0.062 crystal.

The samples of δ = 0.067 and 0.073 crystals were precooled slowly at 4 mKmin^{-1} and 20 mKmin^{-1}, respectively, in the range 230-170 K. The heat evolution and absorption effects in the range 160-225 K and 180-230 K for the respective crystals are due to the glass transitions. No appreciable heat evolution and absorption effect due to a glass transition was observed in the sample with $\delta \geq 0.135$.

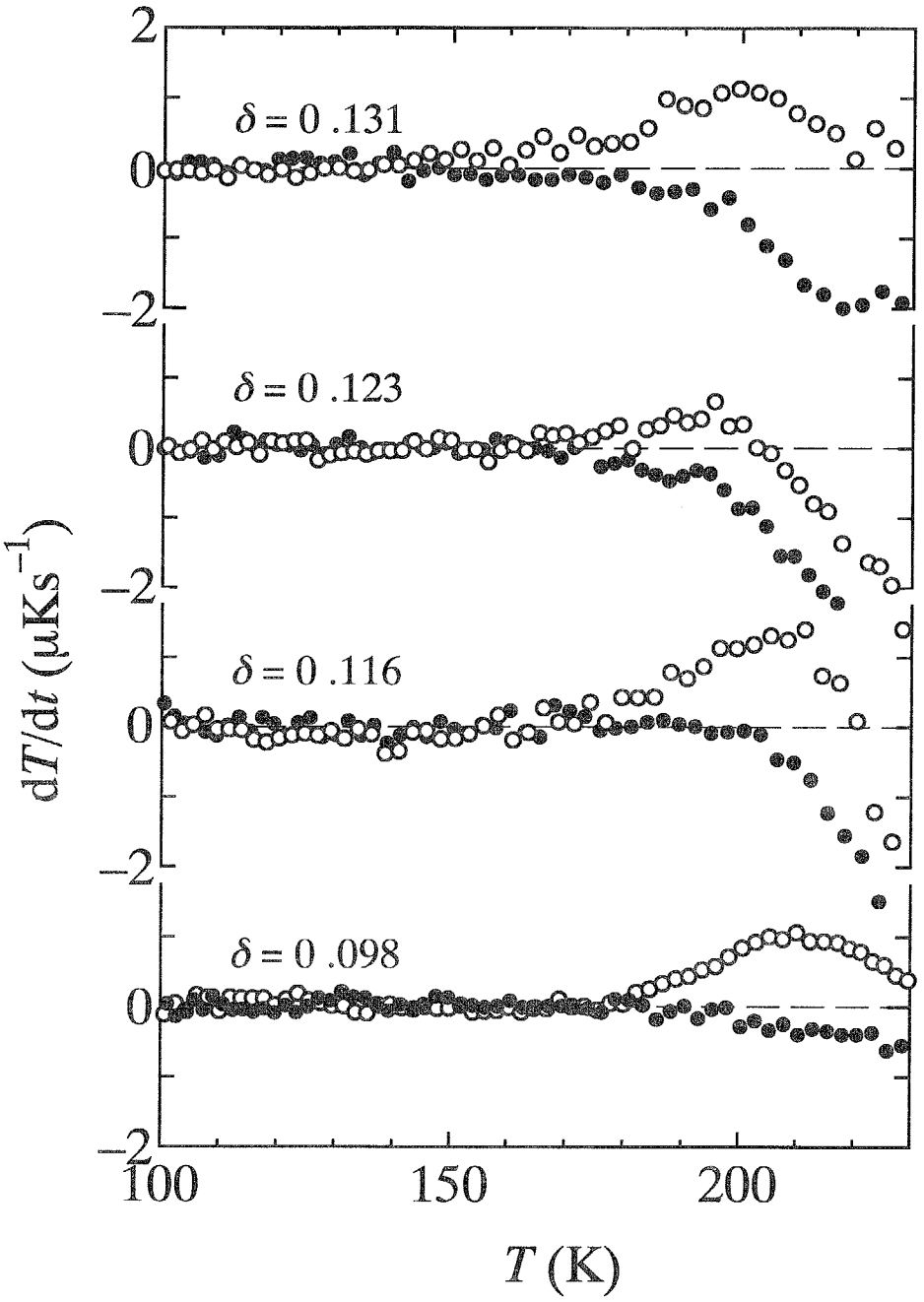

Figure 3.8: Spontaneous temperature-drift rates, shown on an enlarged scale, of $\delta = 0.098$, 0.116, 0.123, and 0.131 crystals in the range 100-230 K.

3.1.3.2.2 Phase transitions/phase separations The heat absorption effects above about 230 K observed in all the crystals are due to phase transitions as follows. Heat capacity curve of $\delta = 0.047$ crystal in Fig. 3.7(a) shows a small peak at 235 K. The peak is assigned as due to a phase transition. The results of $\delta = 0.062$ crystal represented by open and solid circles in Fig. 3.6(a) above 230 K show, in addition to high-temperature tail of heat absorption due to the glass transition, a small heat absorption peak or shoulder at 237 K and sluggish heat absorption effect continuing up to 270 K. Presence of the sluggish heat absorption effect is clearly seen from the plots on an enlarged scale in the bottom-right portion of Fig. 3.6(a). The anomaly at 237 K is due to a phase transition on account that a heat capacity peak was observed at the same temperature as shown in Fig. 3.7(a), and the sluggish absorption effect continuing up to around 270 K corresponds to some heat capacity contribution detected up to 265 K and indicates the presence of phase transition gradually progressing with temperature. The combined appearance of the two successive phase transitions suggests the progress of the processes such as eutectoid or peritectoid phenomena.

$\delta = 0.067$ crystal showed large heat absorption effect having two peaks at 237 K and at 244 K, and heat absorption continuing sluggishly up to 265 K. In view of the fact that two heat capacity peaks were observed at the former two temperatures, the absorption peaks at 237 K and 244 K were concluded to be due to the respective phase transitions. The latter absorption effect up to 265 K is connected to rather sudden decrease in the heat capacity curve at around 255 K, which corresponds to the temperature of completion of phase transition progressing gradually with temperature.

$\delta = 0.073$ crystal exhibited a large heat-absorption peak at 247 K and absorption effect continuing sluggishly up to 275 K. Heat capacity curve showed correspondingly a peak at 247 K and a shoulder at 270 K. The two anomalies are concluded to be caused by a phase transition and the completion of phase transition progressing gradually, respectively.

$\delta = 0.098$ crystal showed two heat-absorption peaks and two corresponding heat-capacity peaks at 249 K and 278 K. These are judged to be due to respective phase transitions. Above 278 K, spontaneous heat absorption effect continued sluggishly up to

above 290 K. This effect might be indicative of some change of state, as suggested from shoulder at the corresponding temperature in the anomalous heat capacity curve given later in Figs. 3.9(a) or 3.11(a).

In $\delta = 0.116$ and 0.123 crystals, a heat-absorption peak and the corresponding heat-capacity peak appeared at 250 K and 240 K, respectively. Then, spontaneous heat absorption effect continuing sluggishly up to around 280 K and 270 K, respectively, and the corresponding shoulders in the heat capacity curve were observed. The behaviors taking place successively of both the heat absorption effects and anomalous heat capacities were rather similar to those at 278 K and 290 K in $\delta = 0.098$ crystal.

$\delta = 0.131$, 0.135, and 0.141 crystals showed a heat-absorption peak and corresponding heat capacity peak at around 270 K, 278 K, and 285 K, respectively, due to a phase transition. It is found from Fig. 3.7(b) that the temperature of the transition increases, the shape of the heat capacity anomaly becomes sharper, and the enthalpy of the transition becomes larger as increasing the excess oxygen composition.

$\delta = 0.150$ and 0.154 crystals showed a sharp heat-absorption peak at 300 K and sluggish heat absorption effects up to 340 K and 360 K, respectively. The heat capacity peak and diffuse heat capacity anomaly were observed correspondingly at the temperature, 300 K, of the heat-absorption peak and in the temperature range where sluggish heat absorption effect was observed. It is concluded that the successive anomalies are due to respective phase transitions. It is found from Fig. 3.7(b) that as increasing the excess oxygen composition the magnitude of heat capacity peak at 300 K decreases, and on the other hand the magnitude of diffuse heat capacity anomaly continuing up to 340 K or 360 K increases. Such two successive phase transitions suggest the progress of the processes such as eutectoid or peritectoid phenomena.

3.1.4 Anomalous heat capacities and antiferromagnetic ordering

The anomalous part of heat capacities due to phase transitions was estimated by subtracting the contribution due to lattice vibrations of La_2NiO_4 crystal from the present experimental values just as done in section 3.1.1. Figures 3.9(a) and 3.9(b) show the

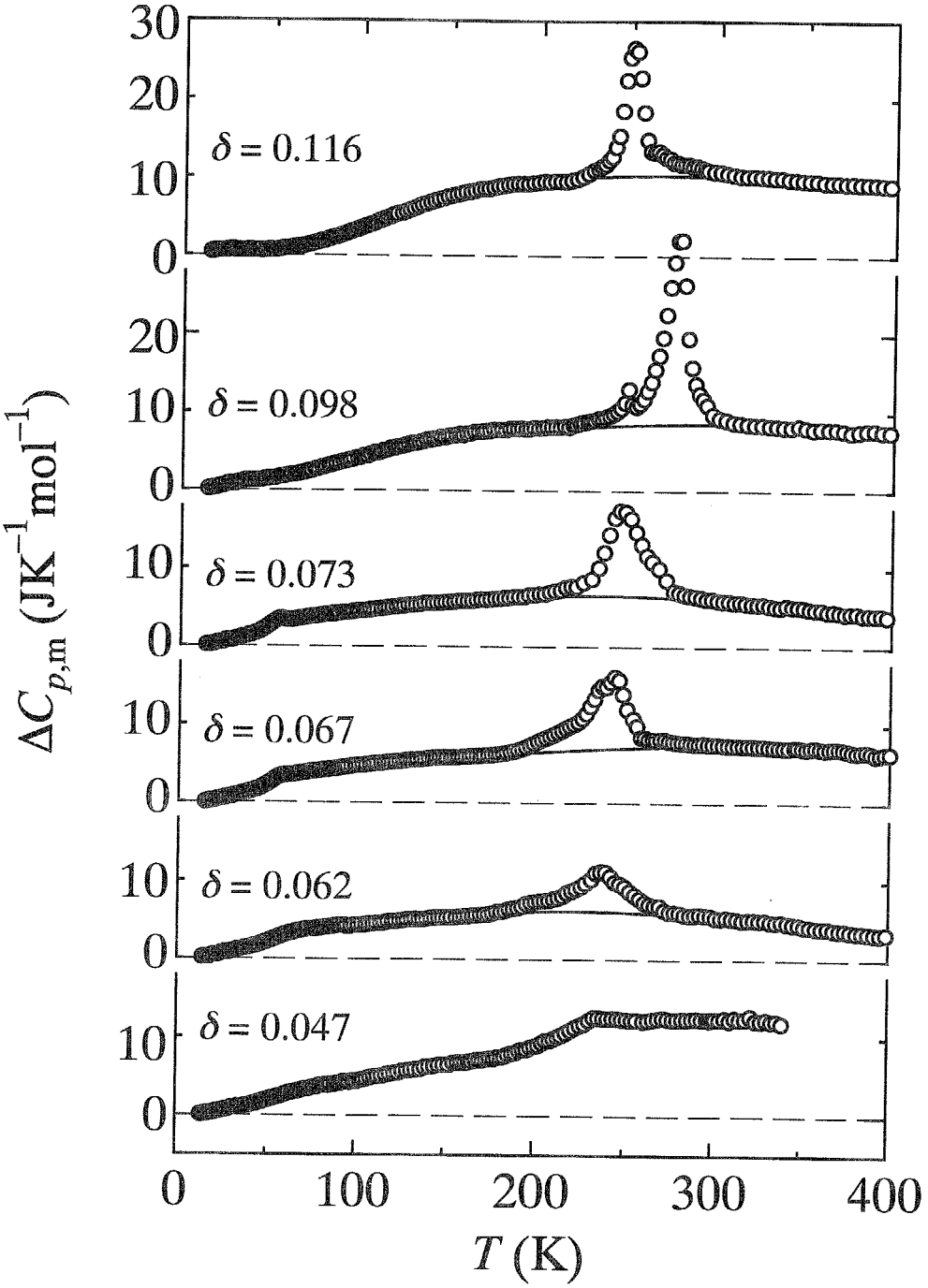

Figure 3.9(a): Excess molar heat capacities of $La_2NiO_{4+\delta}(0.047 \leq \delta \leq 0.116)$ crystals as referred to the lattice heat capacities of La_2NiO_4 crystal derived from the data of phonon density of states.[61]

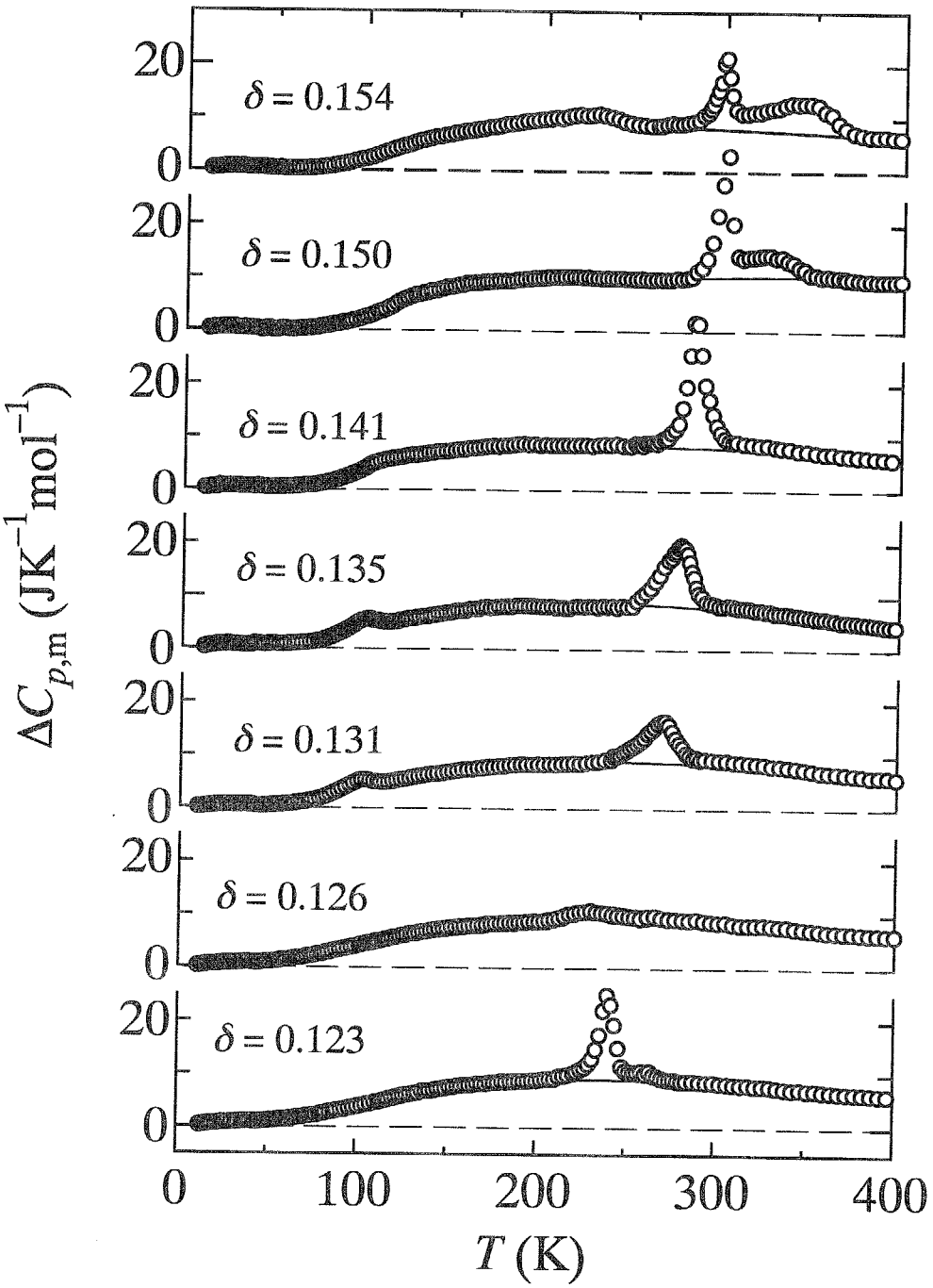

Figure 3.9(b): Excess molar heat capacities of $La_2NiO_{4+\delta}(0.123 \leq \delta \leq 0.154)$ crystals as referred to the lattice heat capacities of La_2NiO_4 crystal derived from the data of phonon density of states.[61]

estimated anomalous part of heat capacities. Anomalies as peaks or shoulders above 230 K were described above in the last section. Heat capacity jump due to a glass transition was clearly demonstrated in the figures around 200 K for $\delta = 0.062$ and 0.067 crystals, 215 K for $\delta = 0.073$ crystal, and 220 K for $\delta = 0.098$, 0.123, and 0.131 crystals, respectively. In $\delta = 0.126$ crystal, heat capacity jump was also observed around 220 K. In $\delta = 0.154$ crystal, a broad peak of heat capacity was observed around 230 K. Though the origin of the anomaly is unclear, it is not related to rearrangement of excess oxygen atoms for the following reason: If the anomaly were related to rearrangement of excess oxygen atoms, the rearrangement motion should be frozen in around 220 K and thus corresponding heat capacity jump should be observed there.

In addition to the anomalies due to phase transition and glass transition based on rearrangement of excess oxygen atoms, there were anomalous heat capacities found over the wide temperature range measured; those appeared to begin at around 15 K and remained up to above 400 K. These must be due to magnetic ordering/disordering of spins in NiO_2 planes similar to stoichiometric crystal. Heat capacity peaks appearing at 55 K in $\delta = 0.067$ and 0.073 crystals and a shoulder around 60 K in $\delta = 0.062$ crystal are interpreted as due to an antiferromagnetic phase transition according to literatures.[29, 63] It is noticed that the peak was sharp in the $\delta = 0.073$ crystal and became broad as the δ decreased. Heat capacity anomaly was observed around 40 K in $\delta = 0.098$, 0.116, and 0.123 crystals, which was interpreted as due to an antiferromagnetic phase transition as is consistent with literatures.[63] As mentioned in section 1.2.3, heat capacity anomalies were observed due to an antiferromagnetic phase transition at around 100 K in the vicinity of $\delta = 0.13$, as a sharp peak for $\delta = 0.131$ and 0.135 crystals and a broad one for $\delta = 0.141$ crystal. Figure 3.10 shows the excess heat capacities of $\delta = 0.131$, 0.135 and 0.141 crystals on an enlarged scale. Open circles in the figure represent the same data as shown in Fig. 3.9(b), that is, the values of low-temperature phase with respect to order-disorder phase transition of excess oxygen atoms. Solid circles in the figure represent values obtained on heating the samples precooled rapidly at 20 $Kmin^{-1}$ from 300 K to 14 K, namely, the values of the supercooled high-temperature phase. It is found that the anomalies around

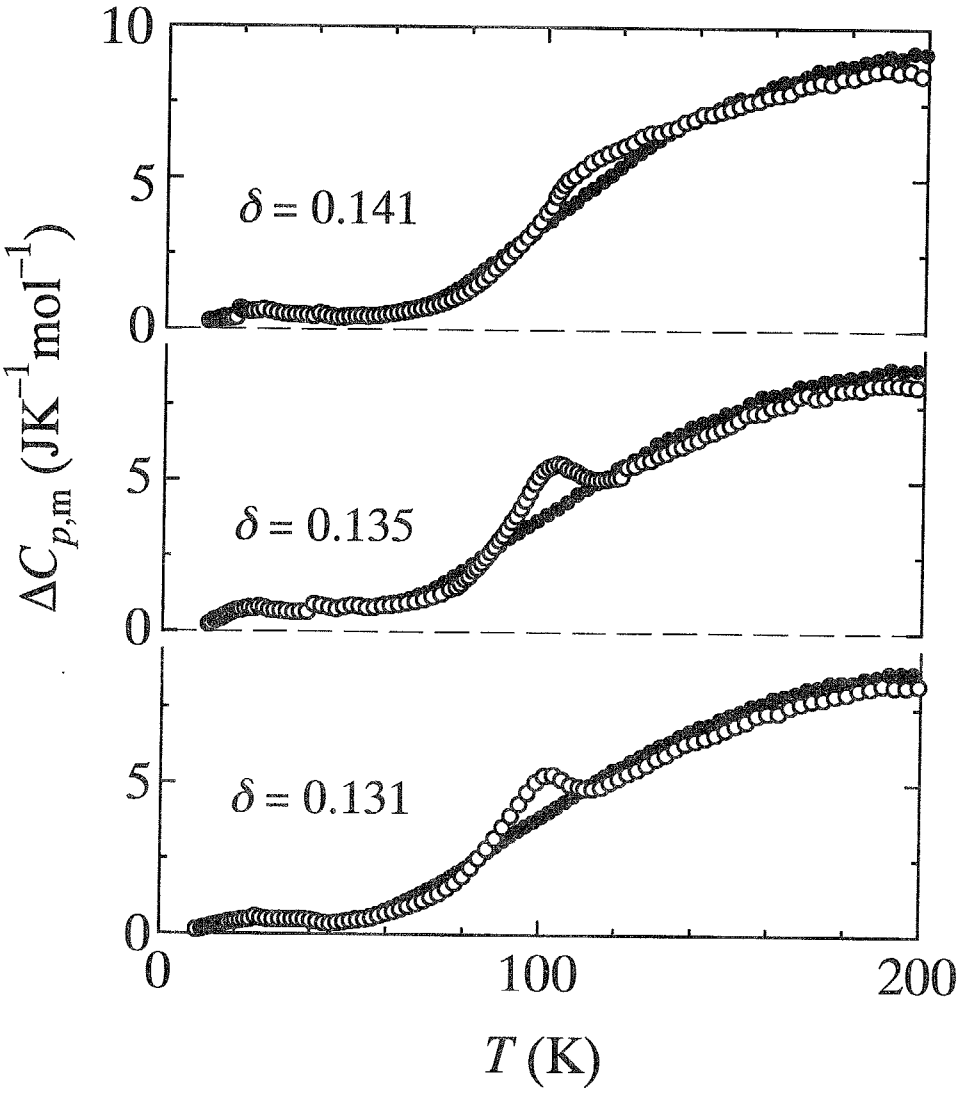

Figure 3.10: Excess molar heat capacities, shown on an enlarged scale, of $\delta = 0.131$, 0.135 and 0.141 crystals in the range 14-200 K: ○, low-temperature phase; ●, supercooled high-temperature phase.

100 K were observed only in the low-temperature phases of $\delta = 0.131$, 0.135, and 0.141 crystals.

3.1.5 Entropies of order-disorder phase transition of excess oxygen atoms

Since rearrangement motion of excess oxygen atoms is frozen-in below 180 K due to the glass transition as described later, there should be no contribution to heat capacities from change in the positional arrangement of excess oxygen atoms below 180 K. Only small heat capacity jumps due to the glass transition were observed in the crystals with $0.062 \leq \delta \leq 0.141$. The anomalous heat capacity curves of the crystals below 180 K seem to be linked smoothly to the respective curves above 350 K except for $\delta = 0.154$ crystal, as indicated by dotted lines in Figs. 3.9(a) and 3.9(b). The base line for $\delta = 0.154$ crystal was estimated by interporating the data in the ranges 250-260 K and 380-400 K. Figures 3.11(a) and 3.11(b) show excess heat capacities, evaluated by subtracting the base lines from the values in Figs. 3.9(a) and 3.9(b) respectively, based on order-disorder phase transition of excess oxygen atoms of the crystals. The entropies of the phase transition were estimated by integrating the excess heat capacity curves. These values are tabulated in Table 3.3 and shown graphically in Fig. 3.12.

3.2 $La_3Ni_2O_{7+\delta}$ system

3.2.1 Heat capacities

Experimental molar heat capacities of $La_3Ni_2O_{7.091}$ crystal are tabulated in Table 3.4 and shown graphically in Fig. 3.13 in the temperature range 14-400 K. The heat capacity curve is relatively smooth and no order-disorder phase transition was observed differently from the behaivior in $La_2NiO_{4.098}$ crystal in spite of similar occupation number of excess oxygen atoms within the interstitial layers.

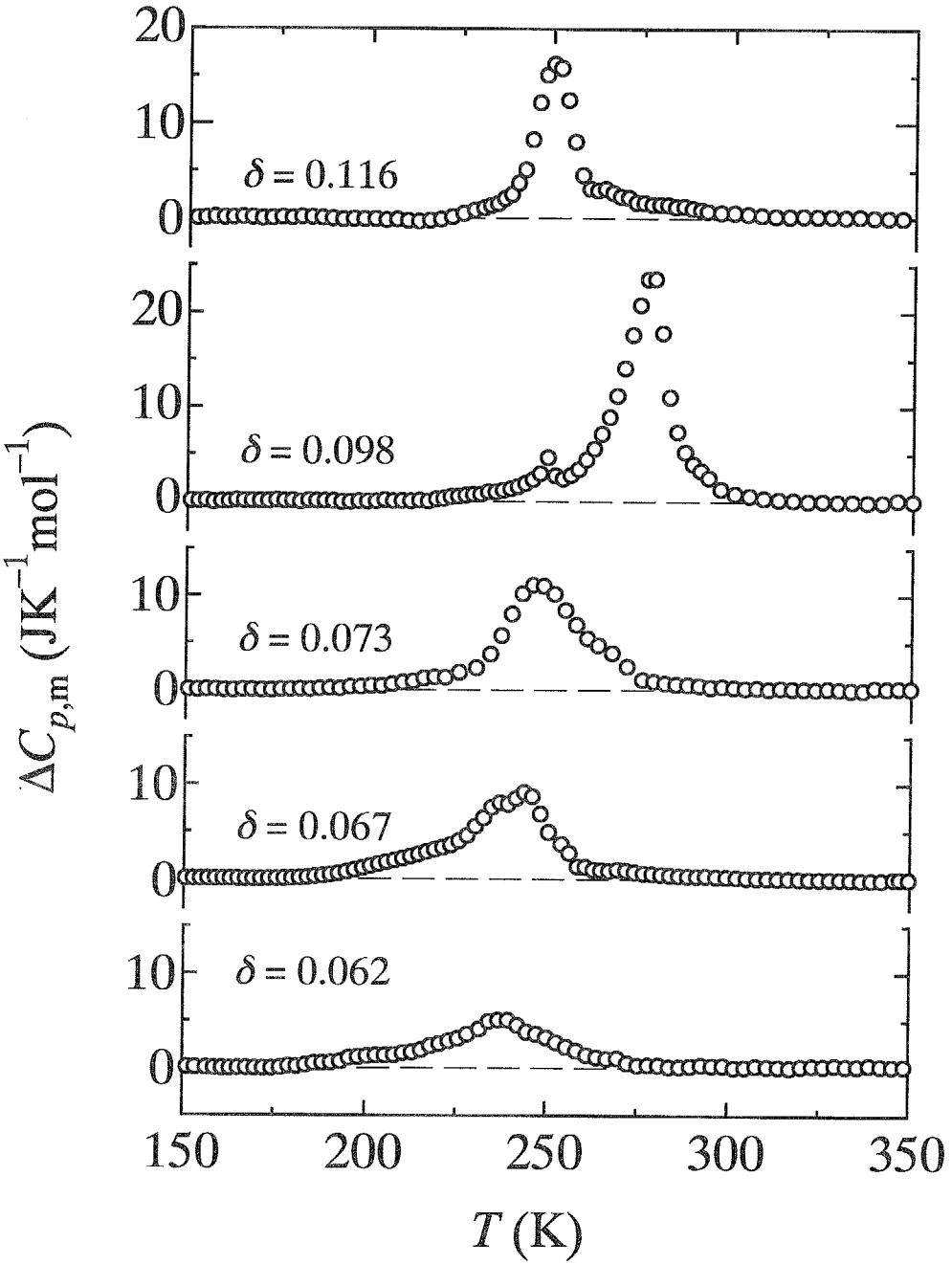

Figure 3.11(a): Anomalous heat capacities due to phase transitions of positional ordering/disordering of excess oxygen atoms in $La_2NiO_{4+\delta}$ crystals with $0.062 \leq \delta \leq 0.116$.

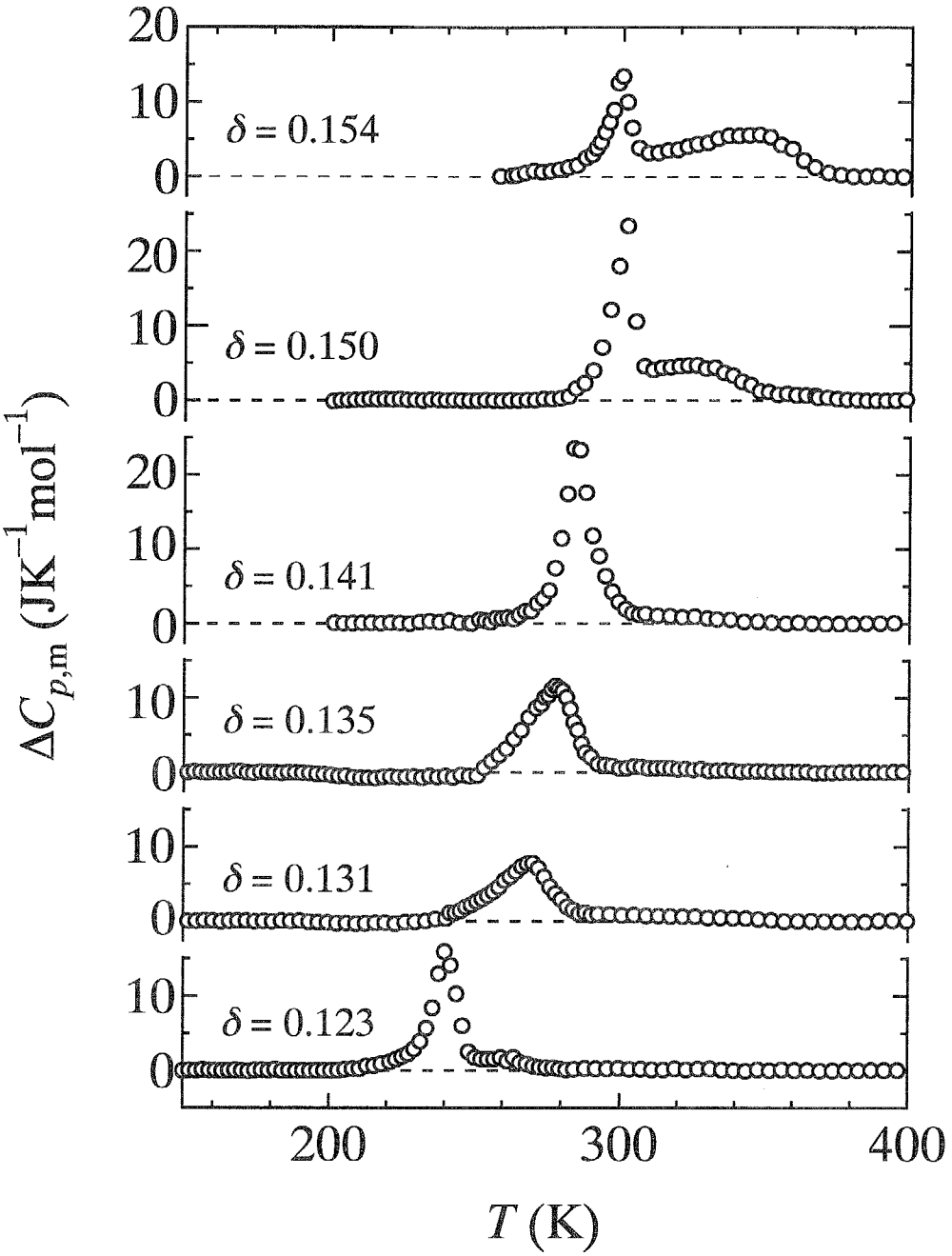

Figure 3.11(b): Anomalous heat capacities due to phase transitions of positional ordering/disordering of excess oxygen atoms in $La_2NiO_{4+\delta}$ crystals with $0.123 \leq \delta \leq 0.154$.

Table 3.3: Entropies of order-disorder phase transitions of excess oxygen atoms in $La_2NiO_{4+\delta}$ crystals

δ	$\Delta_{trs}S$ ($JK^{-1}mol^{-1}$)
0.062	0.91
0.067	1.28
0.073	1.35
0.098	1.77
0.116	1.13
0.123	0.97
0.131	0.96
0.135	0.99
0.141	1.28
0.150	1.14
0.154	1.28

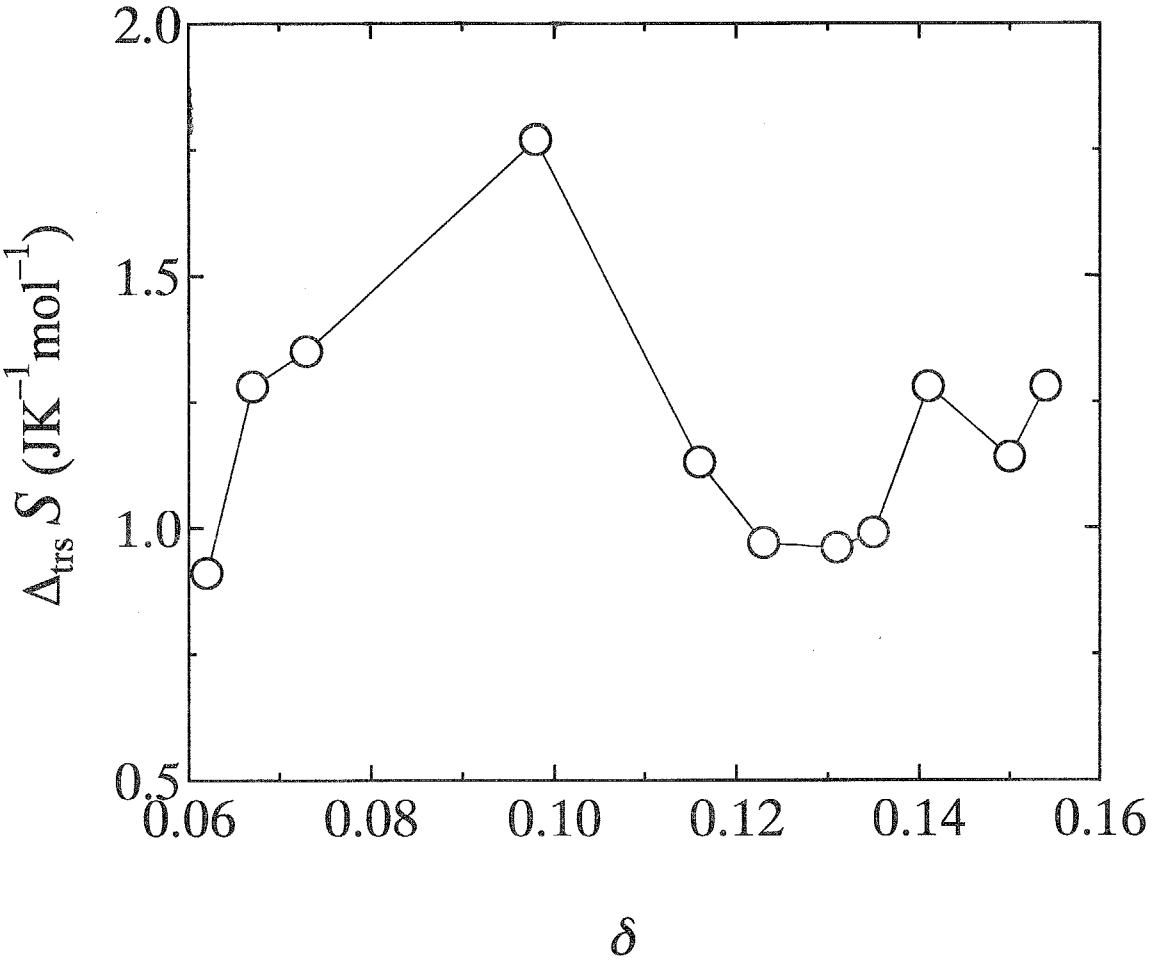

Figure 3.12: Entropies of order-disorder phase transition of excess oxygen atoms estimated by integrating the data shown in Fig. 3.11.

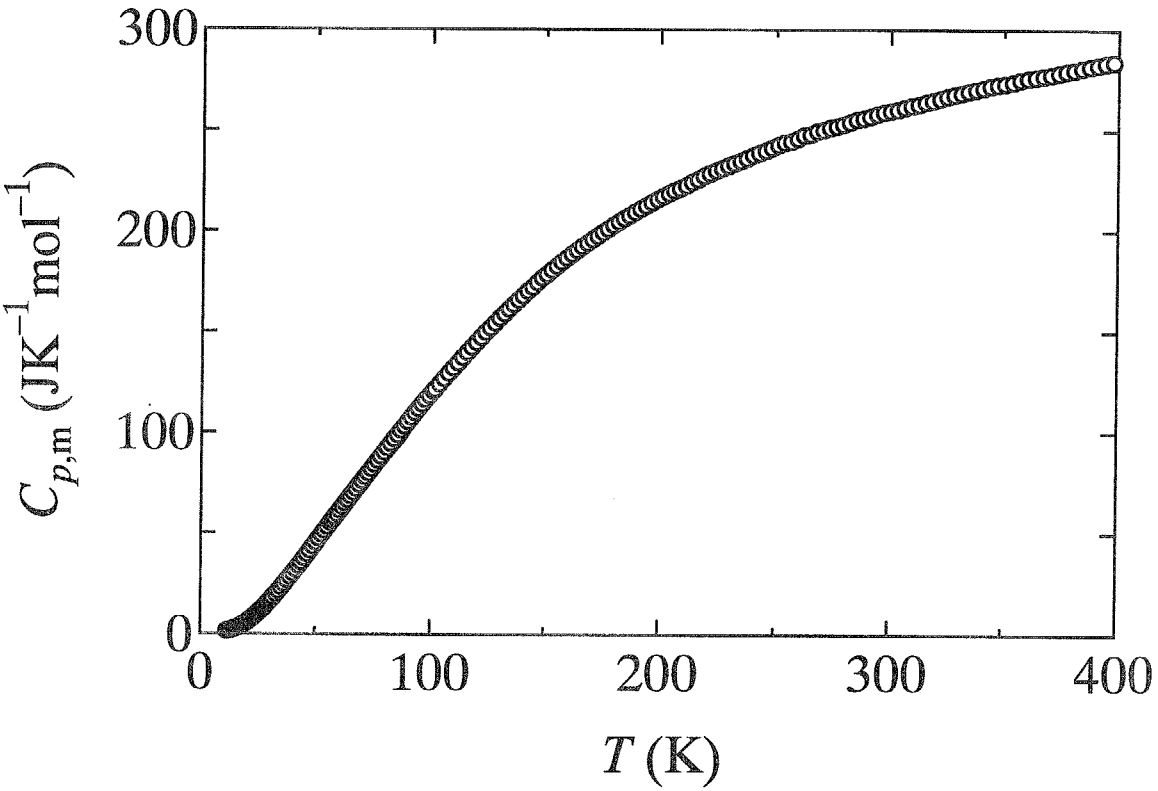

Figure 3.13: Molar heat capacities of $La_3Ni_2O_{7.091}$ crystal.

Table 3.4: Molar heat capacities of $La_3Ni_2O_{7.091}$; R=8.31451 $JK^{-1}mol^{-1}$

$\frac{T_{av}}{K}$	$\frac{C_{p,m}}{R}$	$\frac{T_{av}}{K}$	$\frac{C_{p,m}}{R}$	$\frac{T_{av}}{K}$	$\frac{C_{p,m}}{R}$
11.76	0.1589	50.34	5.450	59.57	7.152
12.37	0.1766	51.61	5.685	60.65	7.352
13.09	0.1946	52.87	5.918	61.76	7.558
14.02	0.2416	54.14	6.148	62.91	7.773
14.89	0.2816	55.41	6.385	64.08	7.991
15.71	0.3234	56.68	6.620	65.27	8.208
16.49	0.3696	57.95	6.860	66.49	8.429
17.32	0.4232	59.22	7.094	67.73	8.656
18.21	0.4892	60.49	7.331	69.00	8.886
19.13	0.5633	61.77	7.570	70.28	9.117
20.05	0.6450	63.04	7.805	71.59	9.353
20.99	0.7364	64.32	8.035	72.91	9.593
21.96	0.8427	65.61	8.269	74.25	9.835
22.95	0.9573	66.89	8.504	75.60	10.08
23.94	1.071	68.18	8.740	76.98	10.33
24.92	1.202	69.48	8.977	78.37	10.58
25.90	1.332	70.77	9.209	79.77	10.83
26.86	1.446	72.07	9.441	81.19	11.09
27.81	1.576	73.38	9.671	82.63	11.35
28.74	1.719	74.69	9.905	84.08	11.61
29.68	1.861	76.00	10.14	85.54	11.86
30.67	2.016	77.31	10.37	87.02	12.13
31.74	2.186	78.63	10.61	88.51	12.39
32.88	2.367	79.96	10.84	90.02	12.65
34.05	2.564	81.29	11.07	91.54	12.91
35.26	2.764	82.62	11.29	93.07	13.17
36.48	2.973	83.96	11.50	94.61	13.43
37.72	3.185	85.30	11.71	96.17	13.69
38.97	3.401	86.64	11.98	97.75	13.95
40.23	3.618	88.00	12.24	99.33	14.21
41.49	3.834	89.36	12.50	100.93	14.47
42.75	4.045	90.73	12.75	101.71	14.58
44.02	4.273	92.11	12.99	103.72	14.91
45.28	4.504	93.49	13.24	105.74	15.22
46.55	4.735	94.88	13.48	107.76	15.54
47.81	4.975	57.50	6.772	109.78	15.85
49.08	5.213	58.52	6.955	111.79	16.16

Table 3.4: (continued)

$\frac{T_{\mathrm{av}}}{\mathrm{K}}$	$\frac{C_{p,\mathrm{m}}}{R}$	$\frac{T_{\mathrm{av}}}{\mathrm{K}}$	$\frac{C_{p,\mathrm{m}}}{R}$	$\frac{T_{\mathrm{av}}}{\mathrm{K}}$	$\frac{C_{p,\mathrm{m}}}{R}$
113.79	16.48	191.68	25.35	288.19	30.75
115.78	16.79	194.09	25.56	291.16	30.88
117.76	17.09	196.52	25.74	294.15	31.00
119.74	17.38	198.97	25.93	297.15	31.12
121.72	17.69	201.43	26.09	300.17	31.20
123.71	17.99	203.90	26.27	303.20	31.27
125.71	18.25	206.39	26.44	306.25	31.40
127.72	18.54	208.90	26.59	309.32	31.52
129.75	18.83	211.42	26.74	312.40	31.61
131.78	19.10	213.94	26.97	315.49	31.74
133.83	19.39	216.49	27.12	318.61	31.83
135.89	19.64	219.05	27.32	321.73	31.95
137.96	19.92	221.63	27.48	324.88	32.08
140.05	20.17	224.22	27.65	328.04	32.18
142.14	20.45	226.83	27.78	331.22	32.27
144.25	20.68	229.46	27.94	334.41	32.38
146.37	20.97	232.10	28.09	337.61	32.48
148.51	21.23	234.76	28.22	340.84	32.57
150.66	21.45	237.43	28.38	344.07	32.70
152.82	21.71	240.12	28.57	347.33	32.78
154.99	21.94	242.83	28.70	350.60	32.85
157.18	22.19	245.55	28.84	353.88	32.92
159.38	22.41	248.28	29.01	357.18	33.08
161.59	22.65	251.03	29.17	360.50	33.15
163.82	22.88	253.79	29.32	363.83	33.22
166.07	23.10	256.57	29.38	367.18	33.30
168.32	23.31	259.37	29.56	370.54	33.38
170.59	23.53	262.18	29.74	373.92	33.48
172.88	23.75	265.01	29.81	377.31	33.59
175.18	23.96	267.85	30.00	380.72	33.67
177.49	24.15	270.71	30.08	384.15	33.78
179.82	24.38	273.58	30.20	387.59	33.87
182.16	24.58	276.47	30.28	391.04	33.97
184.52	24.78	279.38	30.40	394.51	34.07
186.89	24.96	282.30	30.53	398.00	34.15
189.28	25.17	285.24	30.68	401.50	34.25

3.2.2 Standard thermodynamic functions

Standard thermodynamic functions of $La_3Ni_2O_{7.091}$ crystal were evaluated with the obtained heat capacity data according to the basic equations (3.4)-(3.6) on the assumption that $H(0) = 0$ and $S(0) = 0$. Heat capacity values below 13 K were then estimated by extrapolating the values below 20 K in terms of an odd-order polynomial function as follows:

$$C_{p,\mathrm{m}}/(\mathrm{JK^{-1}mol^{-1}}) = 9.401 \times 10^{-4}(T/\mathrm{K})^3 - 1.503 \times 10^{-6}(T/\mathrm{K})^5 + 2.088 \times 10^{-9}(T/\mathrm{K})^7. \tag{3.8}$$

The evaluated values of standared thermodynamic functions are tabulated in Table 3.5.

3.2.3 Glass transition due to freezing-in of rearrangement motion of excess oxygen atoms

Figure 3.14 shows spontaneous-temperature drift rates observed in the range 150-300 K. Solid and open circles represent the values obtained on heating the samples precooled at 20 $\mathrm{Kmin^{-1}}$ from 300 K to 90 K and at 20 $\mathrm{mKmin^{-1}}$ from 240 K to 200 K, respectively. The former sample showed heat evolution effect from 200 K to 260 K and absorption effect then up to 275 K. The latter sample showed heat absorption effect from 220 K to 275 K. Such heat evolution and absorption effects dependent on the cooling rate are characteristic of a glass transition, of course, due to freezing-in of rearrangement motion of excess oxygen atoms. The glass transition temperature was determined from the empirical relation to be 260 K.

3.3 $La_2CuO_{4+\delta}$ system

3.3.1 Magnetic susceptibilities of stoichiometric crystal

Magnetic susceptibility measurements of $La_2CuO_{4.002}$ crystal were carried out under 50 Oe in order to determine the temperature of antiferromagnetic phase transition. Figure 3.15

Table 3.5: Standard thermodynamic functions of $La_3Ni_2O_{7.091}$; R=8.31451 $JK^{-1}mol^{-1}$

$\frac{T_{av}}{K}$	$\frac{C^\circ_{p,m}}{R}$	$\frac{\Delta_0^T H^\circ_m}{R \cdot K}$	$\frac{\Delta_0^T S^\circ_m}{R}$	$\frac{\Phi^\circ_m}{R}$ [a]
0	0	0	0	0
10	0.0975	0.2557	0.0344	0.0088
20	0.6408	3.398	0.2318	0.0619
30	1.911	15.68	0.7124	0.1898
40	3.579	42.98	1.486	0.4117
50	5.384	87.60	2.474	0.7224
60	7.240	150.7	3.620	1.108
70	9.066	232.3	4.874	1.555
80	10.84	331.9	6.202	2.053
90	12.60	448.9	7.578	2.590
100	14.31	583.8	8.997	3.159
110	15.89	734.8	10.44	3.755
120	17.42	901.5	11.88	4.372
130	18.86	1083	13.34	5.006
140	20.18	1278	14.78	5.653
150	21.38	1486	16.22	6.309
160	22.48	1706	17.63	6.973
170	23.48	1935	19.03	7.641
180	24.39	2175	20.39	8.311
190	25.22	2423	21.74	8.983
200	25.99	2679	23.05	9.653

[a] $\Phi^\circ_m/R = (\Delta_0^T S^\circ_m - \Delta_0^T H^\circ_m/T)/R$

(to be continued)

Table 3.5: (continued)

$\frac{T_{\mathrm{av}}}{\mathrm{K}}$	$\frac{C^{\circ}_{p,\mathrm{m}}}{R}$	$\frac{\Delta^T_0 H^{\circ}_{\mathrm{m}}}{R \cdot \mathrm{K}}$	$\frac{\Delta^T_0 S^{\circ}_{\mathrm{m}}}{R}$	$\frac{\Phi^{\circ}_{\mathrm{m}}{}^{a}}{R}$
210	26.69	2943	24.33	10.32
220	27.35	3213	25.59	10.99
230	27.97	3489	26.82	11.65
240	28.55	3772	28.02	12.31
250	29.10	4060	29.20	12.96
260	29.59	4354	30.35	13.61
270	30.05	4652	31.48	14.25
280	30.45	4955	32.58	14.88
290	30.83	5261	33.65	15.51
298.15	31.12	5514	34.51	16.02
300	31.19	5571	34.70	16.13
310	31.54	5885	35.73	16.75
320	31.89	6202	36.74	17.36
330	32.23	6523	37.73	17.96
340	32.56	6847	38.69	18.56
350	32.85	7174	39.64	19.14
360	33.12	7504	40.57	19.73
370	33.38	7836	41.48	20.30
380	33.66	8171	42.37	20.87
390	33.94	8509	43.25	21.43
400	34.20	8850	44.12	21.99

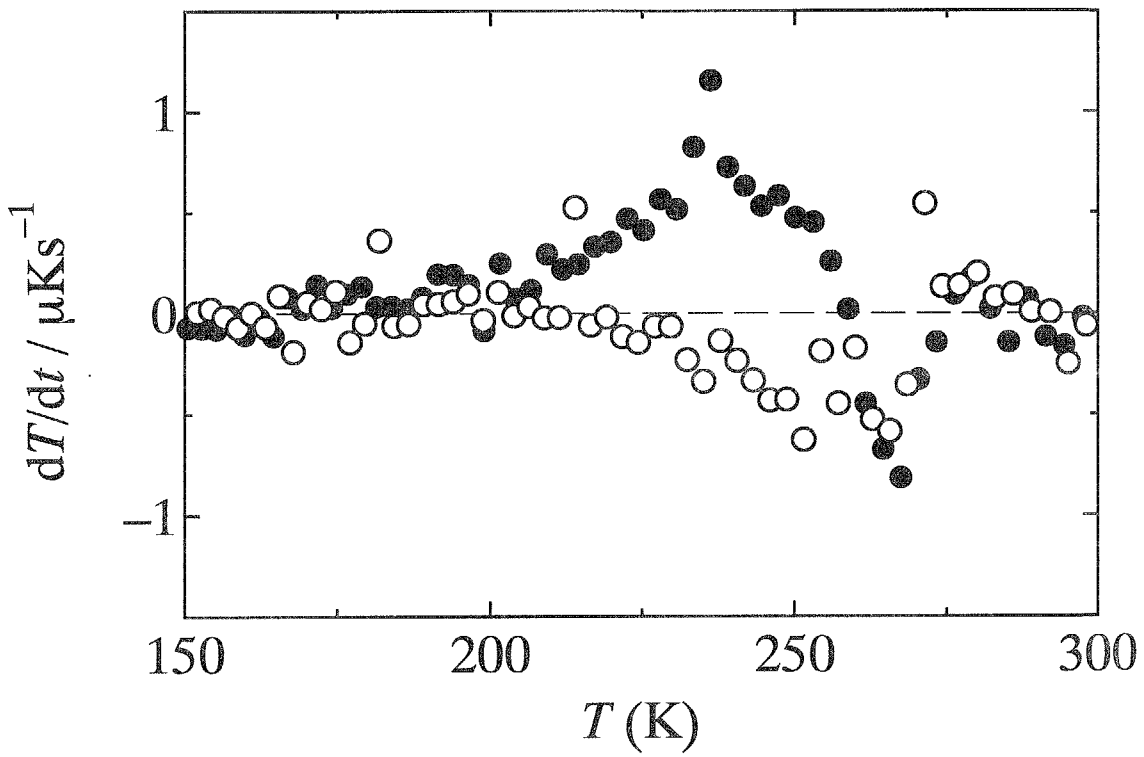

Figure 3.14: Spontaneous temperature-drift rates observed during the heat capacity measurements of $La_3Ni_2O_{7.091}$ crystal: ○, precooled slowly at 20 $mKmin^{-1}$ from 250 K to 200 K; ●, precooled rapidly at 20 $Kmin^{-1}$ from 300 K to 100 K.

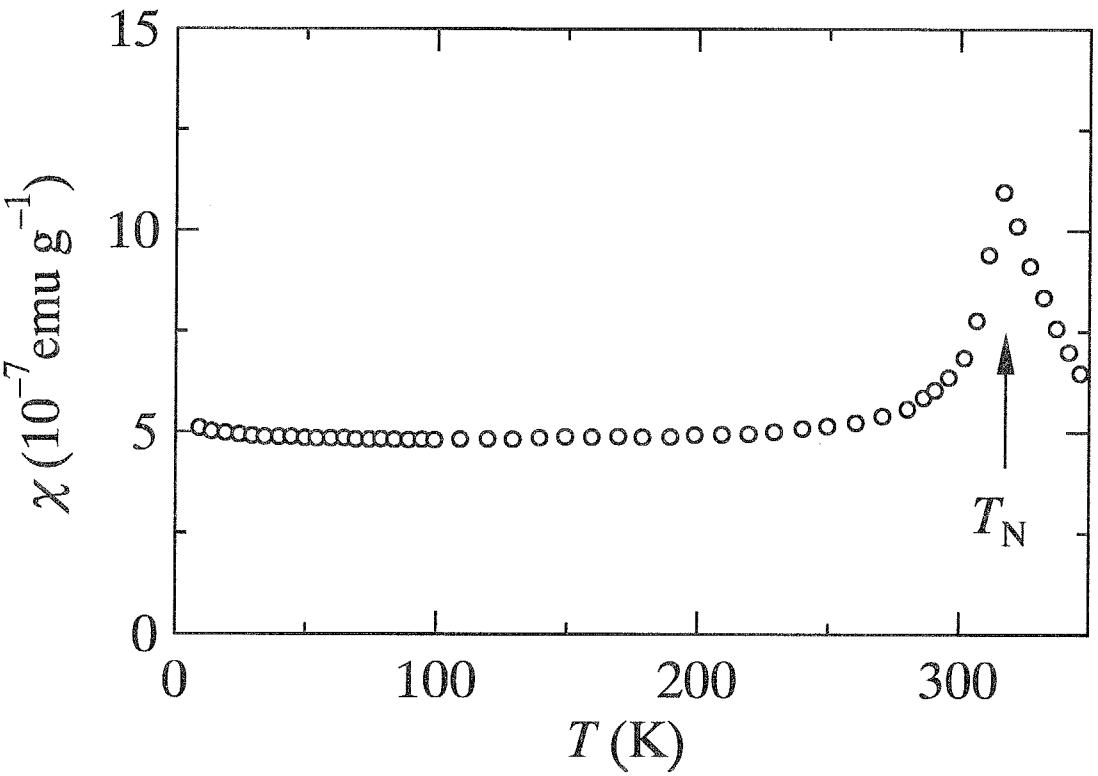

Figure 3.15: Magnetic susceptibilities of $La_2CuO_{4.002}$ crystal under $\boldsymbol{H} = 50$ Oe $\perp$ ab-plane. T_N denotes a Neel temperature.

shows the experimental magnetic susceptibilities of $La_2CuO_{4.002}$ crystal in the temperature range 5-350 K. A magnetic susceptibility anomaly was observed at 316 K due to the antiferromagnetic phase transition.

3.3.2 Heat capacities of stoichiometric crystal

Experimental molar heat capacities of $La_2CuO_{4.002}$ crystal are tabulated in Table 3.6 and shown graphically in Fig. 3.16 in the temperature range 13-330 K. The heat capacity curve is relatively smooth and no heat capacity anomaly was found at the temperature, 316 K, of antiferromagnetic phase transition. The polynomial function derived by being fitted to the experimental heat capacities was used below as a base line for estimation of excess heat capacities of nonstoichiometric crystals $La_2CuO_{4+\delta}$.

3.3.3 Standard thermodynamic functions of stoichiometric crystal

Standard thermodynamic functions of a $La_2CuO_{4.002}$ single crystal were evaluated with the obtained heat capacity data according to the basic equations (3.4)-(3.6) on the assumption that $H(0) = 0$ and $S(0) = 0$. Heat capacity values below 13 K were then estimated by extrapolating the values below 20 K in terms of an odd-order polynomial function as follows:

$$C_{p,\mathrm{m}}/(\mathrm{JK^{-1}mol^{-1}}) = 1.922 \times 10^{-4}(T/\mathrm{K})^3 + 1.435 \times 10^{-6}(T/\mathrm{K})^5 - 2.019 \times 10^{-9}(T/\mathrm{K})^7. \tag{3.9}$$

The evaluated values of standard thermodynamic functions are tabulated in Table 3.7.

3.3.4 Magnetic susceptibilities of nonstoichiometric crystal

Magnetic susceptibility measurements of the nonstoichiometric crystals $La_2CuO_{4+\delta}(\delta = 0.011, 0.035, \text{and } 0.07)$ were carried out under the magnetic field of 50 Oe. Figure 3.17 shows magnetic susceptibilities of $La_2CuO_{4.035}$ single crystal under the field $\boldsymbol{H} \perp ab$-plane in the range 5-320 K. Two anomalies were observed at $T_N = 265$ K and $T_c = 33$ K due to an

Table 3.6: Molar heat capacities of $La_2CuO_{4.002}$; R=8.31451 $JK^{-1}mol^{-1}$

$\frac{T_{av}}{K}$	$\frac{C_{p,m}}{R}$	$\frac{T_{av}}{K}$	$\frac{C_{p,m}}{R}$	$\frac{T_{av}}{K}$	$\frac{C_{p,m}}{R}$	$\frac{T_{av}}{K}$	$\frac{C_{p,m}}{R}$
13.51	0.1185	64.94	5.541	151.56	12.97	250.24	16.88
14.27	0.1382	66.67	5.749	153.93	13.10	252.43	16.95
15.09	0.1721	68.45	5.953	156.31	13.24	254.73	17.01
16.82	0.2490	70.27	6.153	158.72	13.36	256.81	17.07
17.91	0.3063	72.14	6.372	161.14	13.49	259.00	17.12
19.74	0.4124	74.04	6.581	163.58	13.61	261.19	17.17
20.95	0.4953	75.99	6.802	166.03	13.74	263.38	17.21
22.53	0.6243	77.97	7.012	168.51	13.88	265.57	17.27
23.76	0.7250	79.98	7.230	171.00	14.00	267.50	17.33
24.99	0.8353	82.03	7.450	172.73	14.09	269.96	17.40
26.20	0.9530	84.11	7.664	174.78	14.19	272.15	17.46
27.32	1.061	86.22	7.887	176.82	14.28	273.74	17.52
28.46	1.173	88.37	8.101	178.85	14.38	275.10	17.54
29.46	1.278	90.55	8.314	180.87	14.48	277.13	17.55
30.47	1.386	92.75	8.520	182.28	14.55	279.16	17.60
31.49	1.485	94.99	8.734	184.86	14.66	281.19	17.63
32.52	1.606	97.29	8.959	187.46	14.79	283.21	17.67
33.66	1.743	99.35	9.139	190.08	14.89	285.23	17.71
34.90	1.885	101.41	9.318	192.71	15.00	287.25	17.74
36.17	2.020	103.48	9.503	195.37	15.13	288.46	17.78
37.87	2.231	105.56	9.681	198.05	15.25	290.50	17.84
39.46	2.419	107.65	9.861	200.75	15.36	292.55	17.85
41.19	2.640	109.75	10.03	203.36	15.45	294.59	17.87
42.42	2.795	111.86	10.21	205.87	15.54	296.63	17.87
43.50	2.922	113.97	10.39	208.39	15.63	298.67	17.88
44.67	3.063	116.07	10.55	210.91	15.71	300.71	17.89
45.85	3.212	118.18	10.72	213.59	15.79	304.27	17.97
47.02	3.365	120.31	10.88	216.05	15.88	306.28	17.95
48.19	3.505	122.28	11.03	218.50	15.98	308.29	17.98
49.37	3.649	124.44	11.18	220.96	16.05	310.31	18.01
50.55	3.794	126.61	11.34	223.42	16.14	312.32	17.99
51.75	3.945	128.80	11.50	225.87	16.21	316.35	18.05
52.94	4.100	131.00	11.66	228.33	16.29	318.36	18.08
54.15	4.244	133.22	11.81	230.78	16.39	320.37	18.10
55.35	4.396	135.45	11.95	233.23	16.48	322.39	18.16
56.57	4.522	137.70	12.10	235.68	16.52	324.41	18.19
57.78	4.685	139.97	12.25	238.13	16.58	326.43	18.22
59.01	4.834	142.26	12.39	240.58	16.65	328.46	18.22
60.23	4.983	144.56	12.54	243.03	16.71	330.49	18.24
61.46	5.131	146.87	12.68	245.48	16.79		
63.26	5.345	149.21	12.82	247.93	16.84		

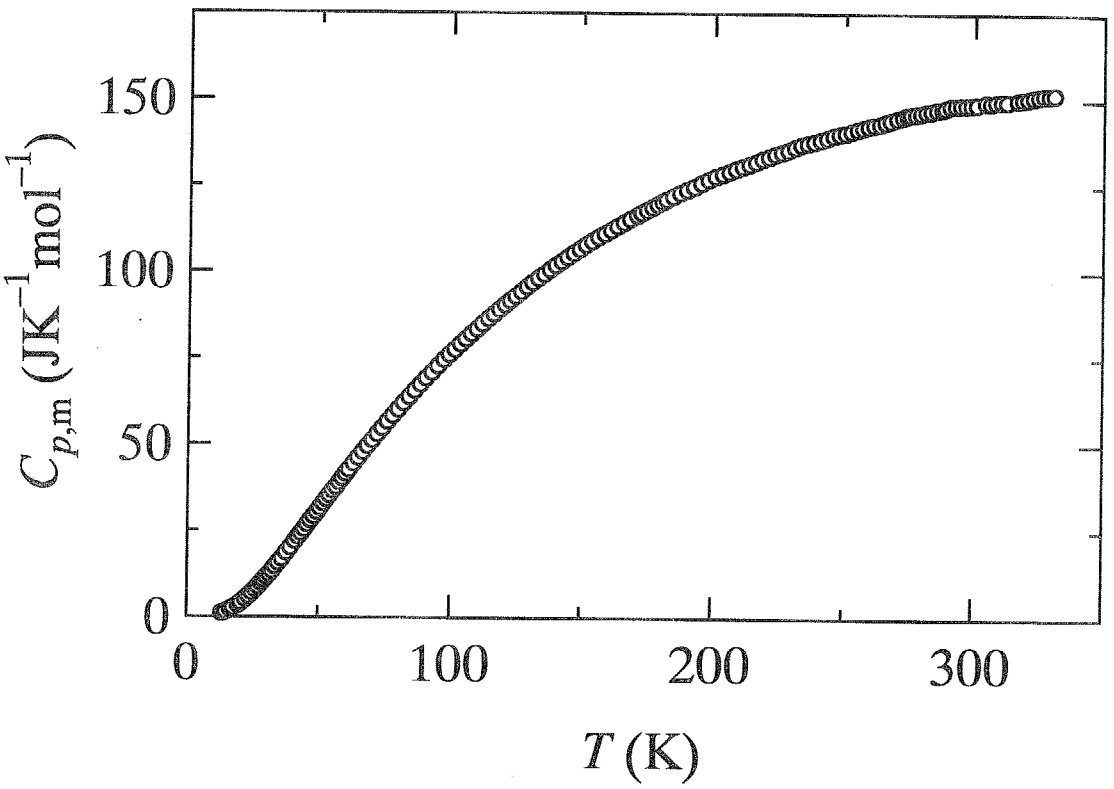

Figure 3.16: Molar heat capacities of $La_2CuO_{4.002}$ crystal.

Table 3.7: Standard thermodynamic functions of $La_2CuO_{4.002}$; R=8.31451 $JK^{-1}mol^{-1}$.

$\frac{T}{K}$	$\frac{\Delta_0^T C^\circ_{p,m}}{R}$	$\frac{\Delta_0^T H^\circ_m}{R \cdot K}$	$\frac{\Delta_0^T S^\circ_m}{R}$	$\frac{\Phi^\circ_m}{R}$ [a]
0	0	0	0	0
10	0.0380	0.084	0.011	0.002
20	0.429	1.989	0.128	0.028
30	1.332	10.51	0.461	0.111
40	2.489	29.48	0.999	0.262
50	3.730	60.57	1.687	0.476
60	4.953	104.0	2.476	0.742
70	6.129	159.5	3.329	1.050
80	7.235	226.4	4.220	1.391
90	8.257	303.9	5.132	1.756
100	9.197	391.2	6.052	2.139
110	10.06	487.6	6.969	2.537
120	10.85	592.2	7.879	2.944
130	11.58	704.4	8.777	3.358
140	12.25	823.7	9.660	3.777
150	12.87	949.3	10.53	4.198
160	13.43	1081	11.38	4.620
170	13.95	1218	12.21	5.042
180	14.44	1360	13.02	5.463
190	14.89	1506	13.81	5.881
200	15.33	1658	14.58	6.297
210	15.68	1813	15.34	6.710
220	16.02	1971	16.08	7.119
230	16.36	2133	16.80	7.524
240	16.64	2298	17.50	7.926
250	16.89	2466	18.19	8.322
260	17.14	2636	18.85	8.715
270	17.40	2809	19.50	9.102
280	17.62	2984	20.14	9.485
290	17.79	3161	20.76	9.863
298.15	17.89	3306	21.26	10.17
300	17.91	3339	21.37	10.24
310	17.99	3519	21.96	10.61
320	18.11	3699	22.53	10.97
330	18.23	3881	23.09	11.33

[a] $\Phi^\circ_m/R = (\Delta_0^T S^\circ_m - \Delta_0^T H^\circ_m/T)/R$

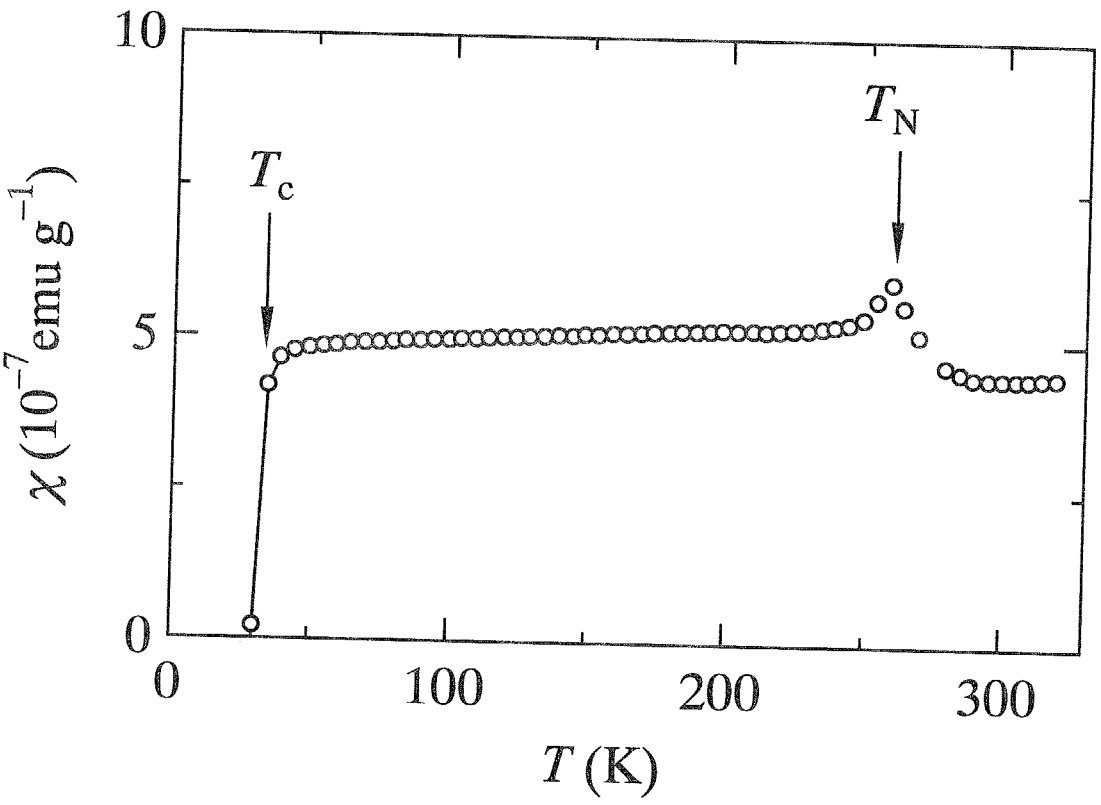

Figure 3.17: Magnetic susceptibilities of $La_2CuO_{4.035}$ crystal under field cooling of $\boldsymbol{H}$ = 50 Oe $\perp$ *ab*-plane.

antiferromagnetic phase transition and a superconducting phase transition, respectively. Figure 3.18 shows magnetic susceptibilities of $La_2CuO_{4.07}$ crystal in the range of 5-55 K. One anomaly was observed at 44 K due to a superconducting phase transition.

It has been reported that the superconducting phase transition temperature is sensitive to the cooling rate or annealing time around 200 K[49, 50] as stated in section 1.2.2. The annealing effects were examined in $La_2CuO_{4.011}$ crystal as follows. Figure 3.19 shows magnetic susceptibilities obtained on heating the $La_2CuO_{4.011}$ powder crystal subjected to following thermal pretreatments. When the sample was quenched at about 25 $Kmin^{-1}$ from 320 K to 5 K (triangles in the figure), the Meissner effect started to appear at around 30 K and increased gradually with decreasing temperature and sharply below around 20 K. The two samples annealed at 250 K and then quenched to 5 K in advance (squares and diamonds in the figure) exhibited the diamagnetic Meissner effect starting at 33 K, and the longer annealing there gave rise to the larger effect while holding the starting temperature at the same 33 K. The samples annealed at 210 K after precooled to 5 K (open and solid circles) showed the Meissner effect starting at 40 K. The difference in the annealing periods between 20 h and 42 h did not make much difference in the Meissner fractions.

3.3.5 Structural phase transitions of a displacive type in $La_2CuO_{4.011}$ and $La_2CuO_{4.035}$ crystals

Figure 3.20 shows experimental molar heat capacities of $La_2CuO_{4.011}$ and $La_2CuO_{4.035}$ crystals in the temperature range 14-360 K. Three heat capacity anomalies were observed at around 290 K, 265 K, and 222 K due to structural phase transitions of a second-order type, a Martensitic type, and a first-order type, respectively, described below in detail.

Figures 3.21(a) and 3.21(b) show excess heat capacities of $La_2CuO_{4.011}$ and $La_2CuO_{4.035}$ crystals, respectively, in the range 13-330 K; the values were evaluated by subtracting the base line estimated by being fitted to the heat capacities of $La_2CuO_{4.002}$ crystal, from the experimental heat capacities. (The values above 330 K could not be evaluated because the heat capacities of $La_2CuO_{4.002}$ crystal were measured only below

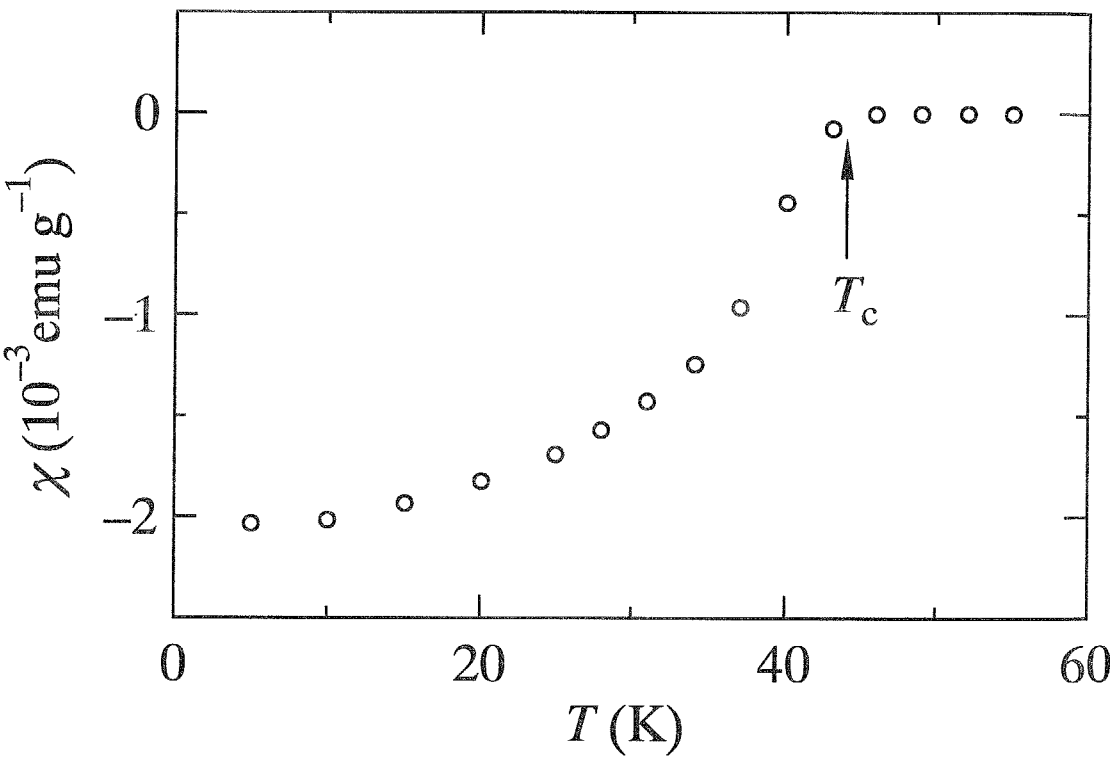

Figure 3.18: Magnetic susceptibilities of $La_2CuO_{4.07}$ crystal in the temperature range of 5-60 K under $H = 50$ Oe.

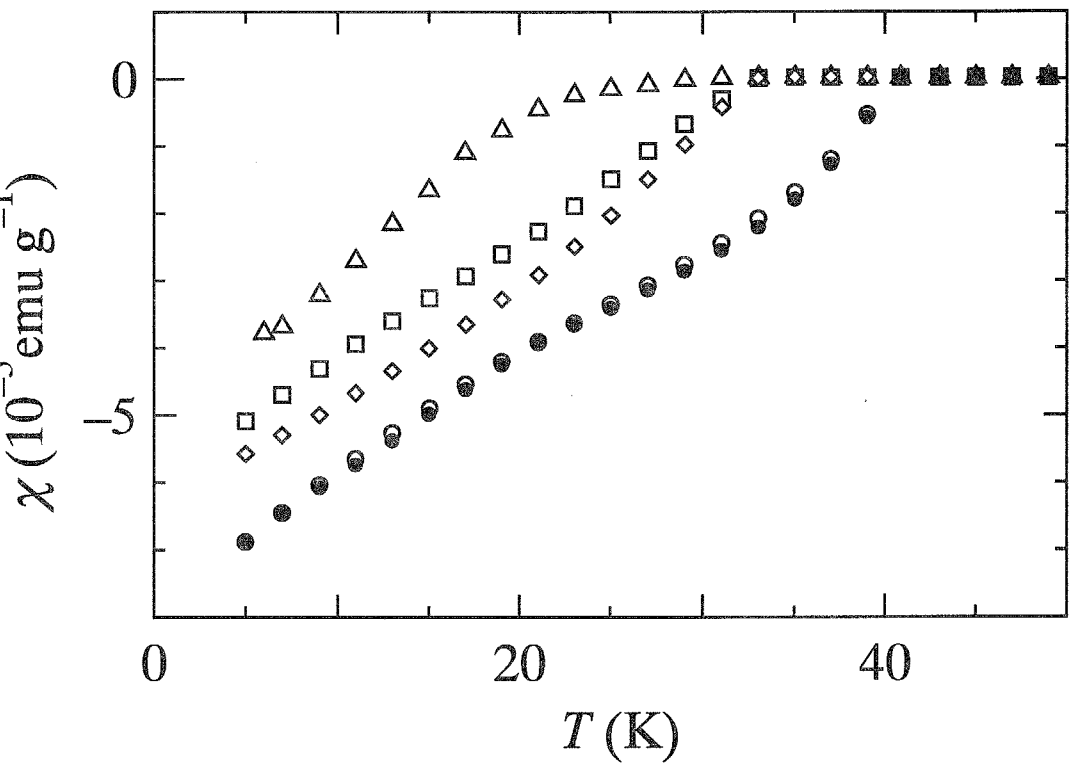

Figure 3.19: Magnetic susceptibilities of $La_2CuO_{4.011}$ crystal in the temperature range of 5-50 K under $H = 50$ Oe: △, quenched at 25 Kmin^{-1} from 320 K to 5 K; □, ◇, annealed at 250 K for 3 and 18 h, respectively, and then quenched; ○, ●, annealed at 210 K for 20 and 44 h, respectively, after the quenching from 320 K to 5 K.

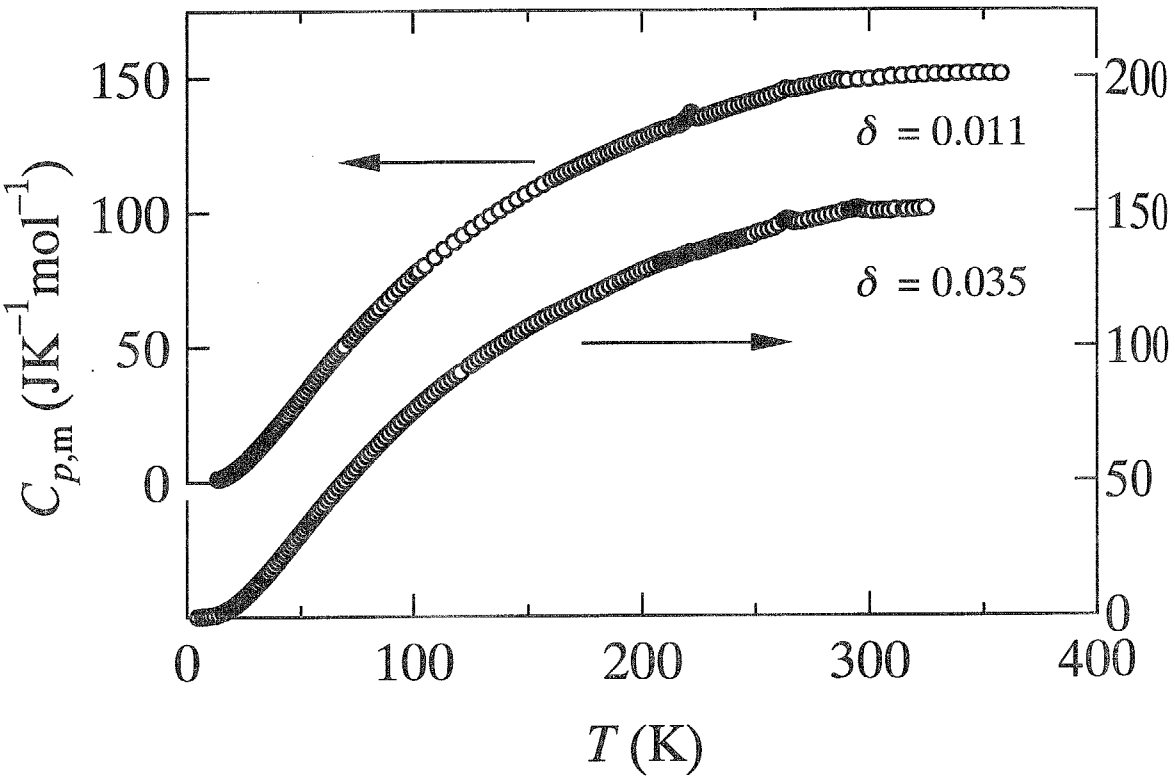

Figure 3.20: Molar heat capacities of $La_2CuO_{4.011}$ and $La_2CuO_{4.035}$ crystals. The ordinate is shifted upwards by 50 $JK^{-1}mol^{-1}$.

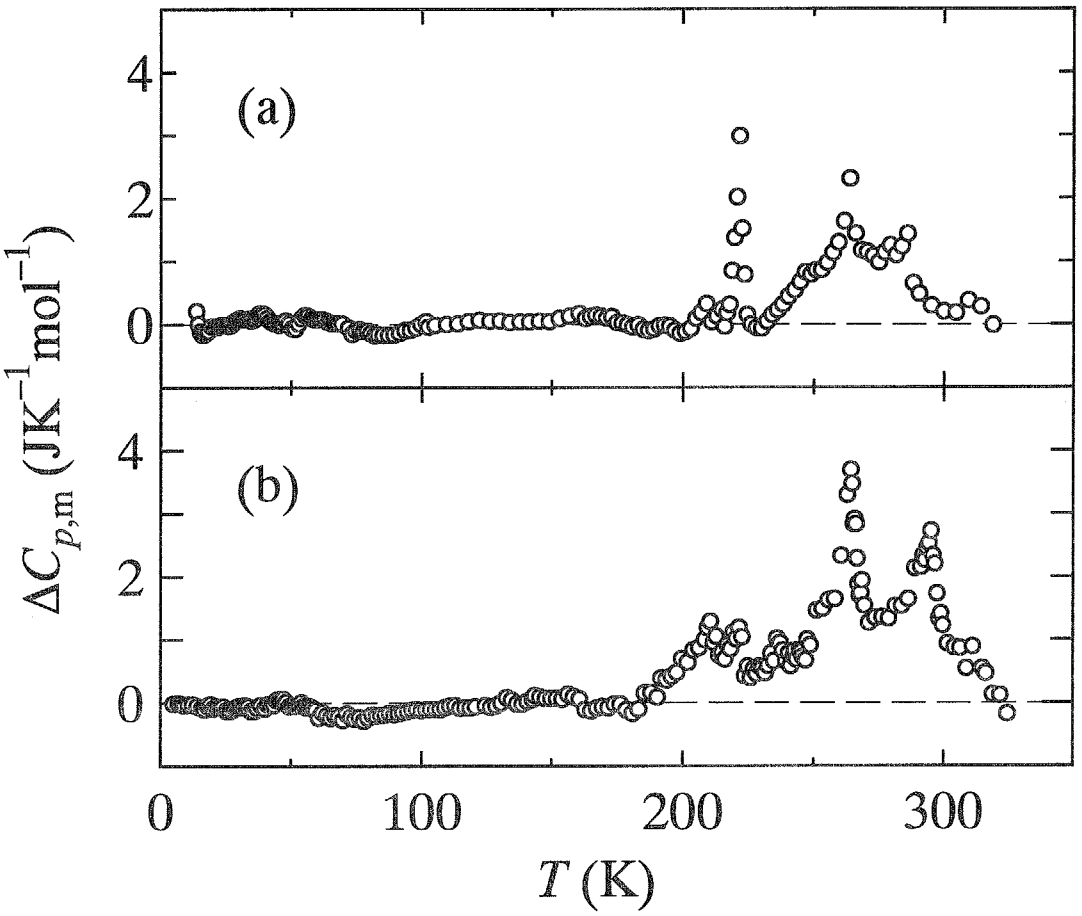

Figure 3.21: Excess heat capacities evaluated by subtracting the base line, derived by being fitted to the data of $La_2CuO_{4.002}$ crystal, from the experimental heat capacities: (a) $La_2CuO_{4.011}$; (b) $La_2CuO_{4.035}$.

330 K.) The excess entropies estimated by using the excess heat capacities between 190 K and 310 K were about 0.3 and 0.5 $JK^{-1}mol^{-1}$ for $La_2CuO_{4.011}$ and $La_2CuO_{4.035}$ crystals, respectively. The smallness of the values suggests that the heat capacity anomalies involve no order-disorder process of excess oxygen atoms.

Figures 3.22(a) and 3.22(b) show the heat capacities around 287 K and 295 K for $La_2CuO_{4.011}$ and $La_2CuO_{4.035}$ crystals, respectively, on enlarged scales. The respective symbols represent the values obtained on heating the samples precooled from 300 K to the temperatures written in the figures. In view of the fact that the respective three sets of data are located on a single curve within their experimental errors and that no spontaneous temperature drift has been observed around the temperatures of the anomalies immediately after the precooling treatments nor during the heat capacity measurements on heating the respective samples, these phase transitions are understood to be of a second-order type.

Figures 3.23(a) and 3.23(b) show the heat capacities of $La_2CuO_{4.011}$ and $La_2CuO_{4.035}$ crystals, respectively, around 265 K on enlarged scales, where the respective symbols represent the values obtained on heating the samples precooled from 280 K to the temperatures written in the figures and dashed lines stand for the base lines used for estimating the anomalous parts of heat capacities. The base lines were estimated by smoothly interpolating the respective data in the ranges 270-280 K and 230-250 K. All of the five sets and the four sets of data, respectively, were located on different curves depending on the low temperature limit of each precooling, and meanwhile no appreciable spontaneous temperature drift was observed even just after the precooling nor during the heat capacity measurements on heating the respective samples. The former indicates that the transition is of a first-order type and the latter that the transition proceeds in a short time to a certain quasi-equilibrium state. These are characteristics of a Martensitic phase transition. Figures 3.24(a) and 3.24(b) show hysteresis loops of the enthalpy of transition between the paths in the heating and cooling directions for $La_2CuO_{4.011}$ and $La_2CuO_{4.035}$ crystals, respectively. The total transition enthalpies and entropies of $La_2CuO_{4.011}$ and $La_2CuO_{4.035}$ crystals were estimated to be about 5 and 14 $Jmol^{-1}$ and 0.02 and 0.05

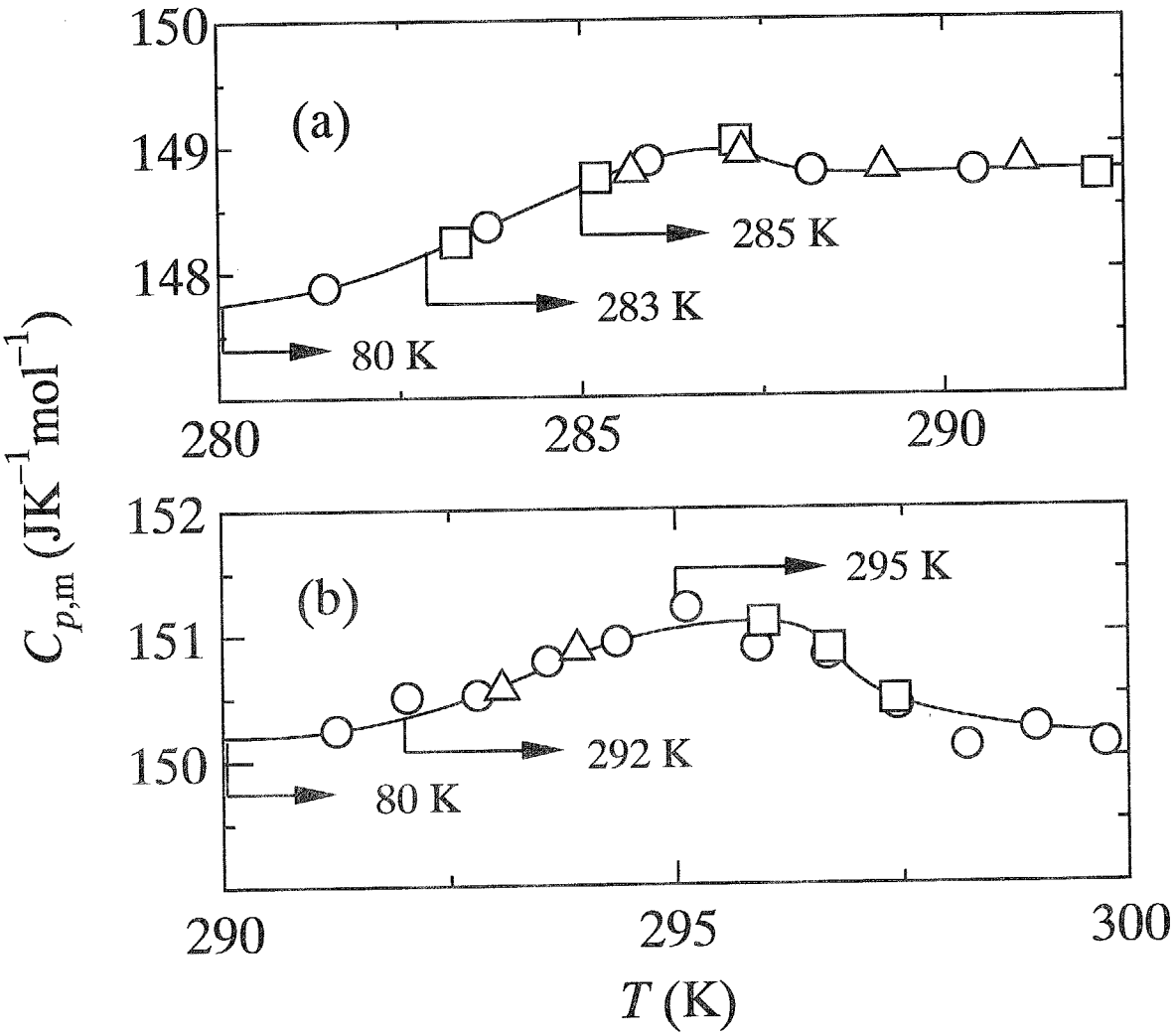

Figure 3.22: Heat capacities of (a) $La_2CuO_{4.011}$ around 287 K and (b) $La_2CuO_{4.035}$ around 295 K, on enlarged scales. Temperatures in the figure indicate the lowest temperatures that each sample has experienced just before the measurements. Solid lines are guides for eyes.

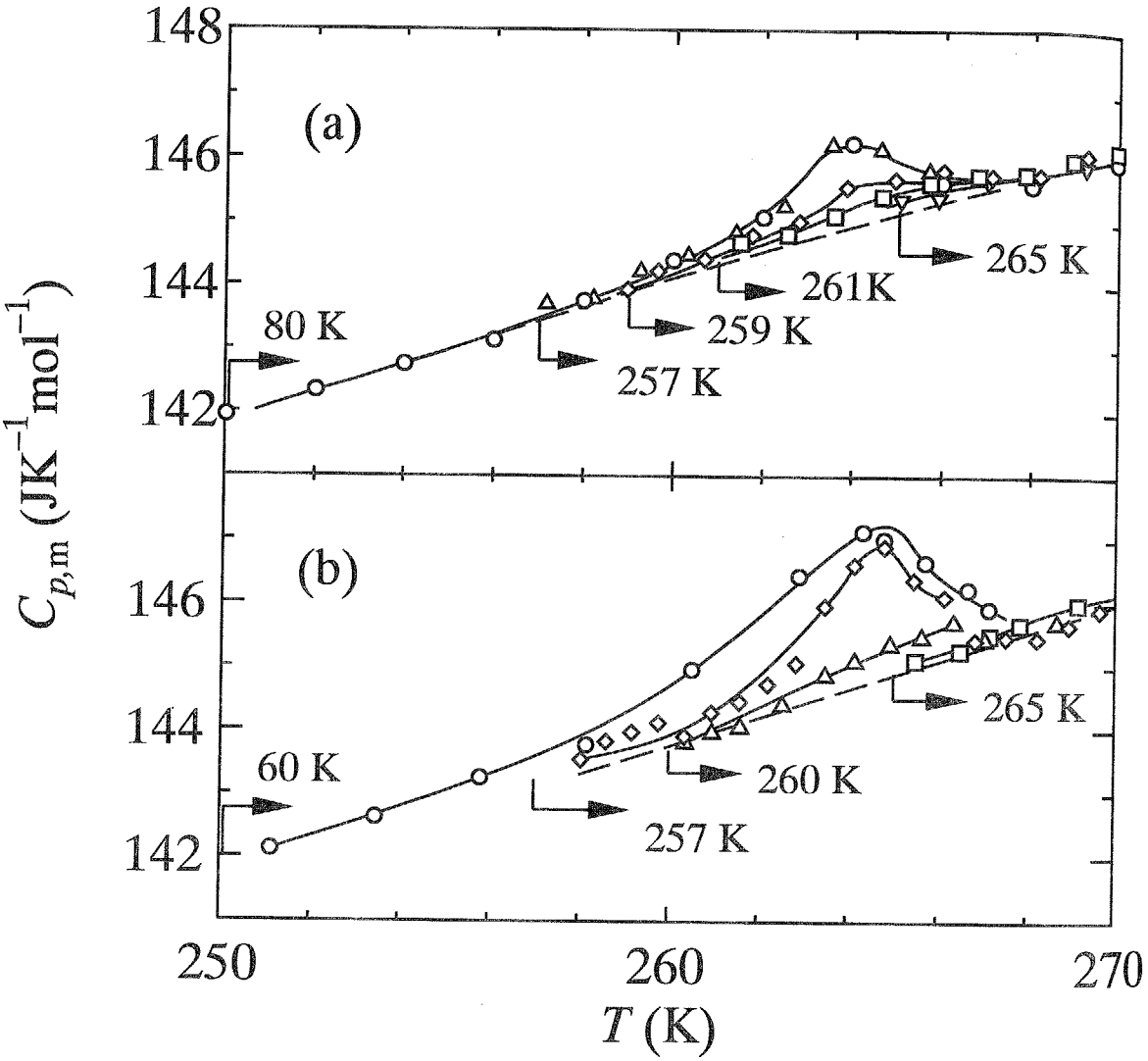

Figure 3.23: Thermal hysteresis in the heat capacities observed around 265 K: (a) $La_2CuO_{4.011}$; (b) $La_2CuO_{4.035}$. Temperatures in the figure indicate the lowest temperatures that each sample has experienced just before the measurements and dashed lines represent the base lines for estimating the excess part of heat capacity. Solid lines are guides for eyes.

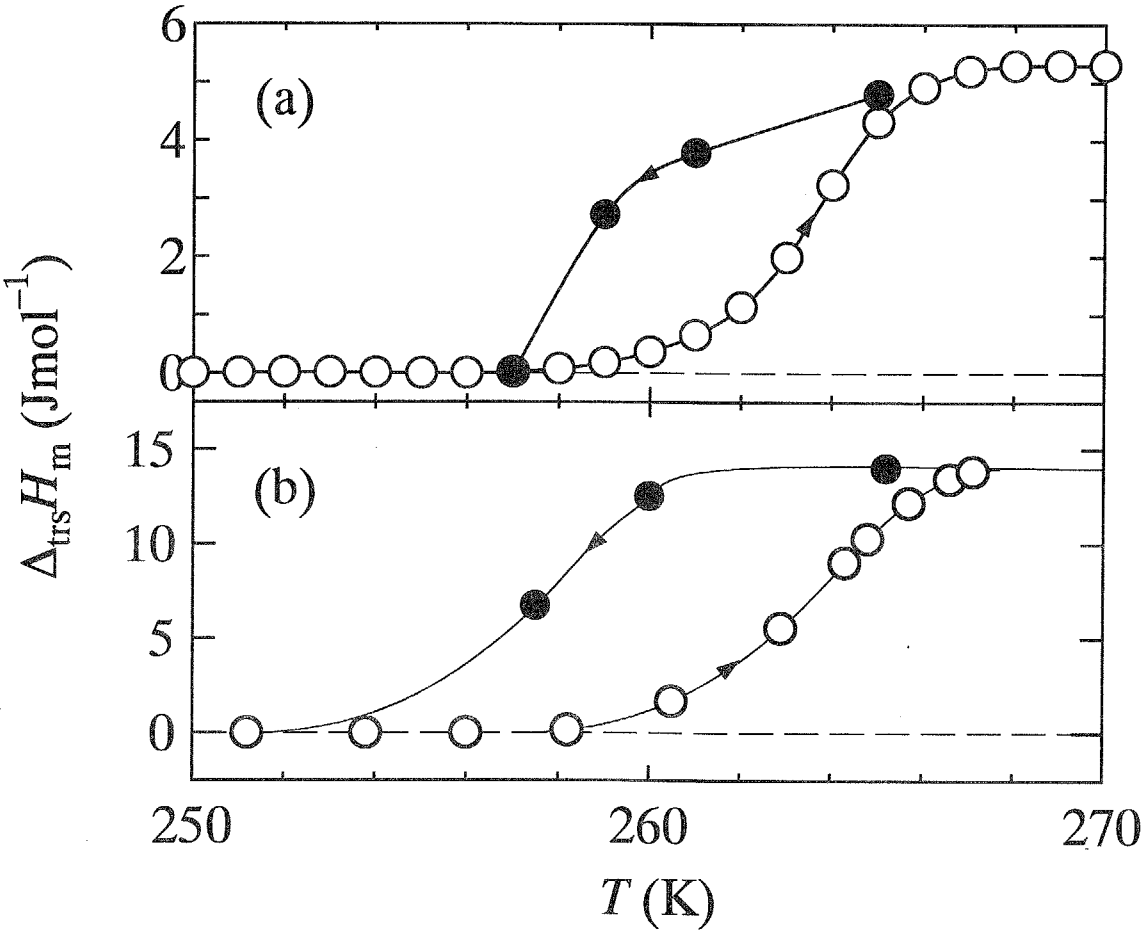

Figure 3.24: Temperature dependence of the enthalpy of transition around 265 K for (a) $La_2CuO_{4.011}$ and (b) $La_2CuO_{4.035}$: ○, in the heating direction; ●, in the cooling direction.

$JK^{-1}mol^{-1}$, respectively.

Figures 3.25(a) and 3.25(b) show the heat capacities and the spontaneous temperature drift rates, respectively, of $La_2CuO_{4.011}$ crystal observed in the temperature-rating periods of the measurements around 222 K. The sample quenched at 20 $Kmin^{-1}$ from 270 K to 150 K (squares in the figure) exhibited heat evolution starting at around 205 K and ceasing at 217 K and subsequently heat absorption in the range between 217 K and 225 K. When annealed at 210 K for 4 h after precooling to 180 K (triangles in the figure), the sample exhibited smaller heat evolution effect around 210 K than, but almost the same magnitude of heat absorption effect around 222 K as the quenched sample did. In the case where the sample was annealed at 210 K for 50 h (open circles in the figure), the heat evolution entirely disappeared and larger heat absorption effect was observed than in the previous cases. Meanwhile the sample precooled from 270 K to 212 K (solid circles in the figure) showed neither heat capacity anomalies nor spontaneous heat evolution or absorption effects around 222 K at all. It is concluded from these that the anomaly in 200-225 K is attributed to a first-order phase transition; namely, the heat evolution around 210 K corresponds to the high-temperature to low-temperature phase transition and the heat absorption effect around 222 K to the opposite process. The observation that the sample precooled from 270 K to 212 K undergoes no transition from the high-temperature to low-temperature phase at 212 K is understood as due to absence of the nucleus of low-temperature phase. The understanding is reasonable in that a first-order transition proceeds with two processes of the nucleation of a new phase and the growth and that the nucleation tends to proceed in the low temperature range (away from the transition point) where the Gibbs energy difference between the two phases becomes large [64, 65]. The enthalpy and entropy of transition were evaluated to be 8 $Jmol^{-1}$ and 0.04 $JK^{-1}mol^{-1}$, respectively. Figures 3.26(a) and 3.26(b) show the heat capacities and the spontaneous temperature-drift rates of $La_2CuO_{4.035}$ crystal observed in the temperature-rating periods of the measurements around 222 K, respectively. The sample was precooled rapidly at 10 $Kmin^{-1}$ from 300 K to 80 K, and exhibited the same heat evolution and absorption effects and the same heat capacity anomaly around 222 K as $La_2CuO_{4.011}$ crystal. Therefore, this

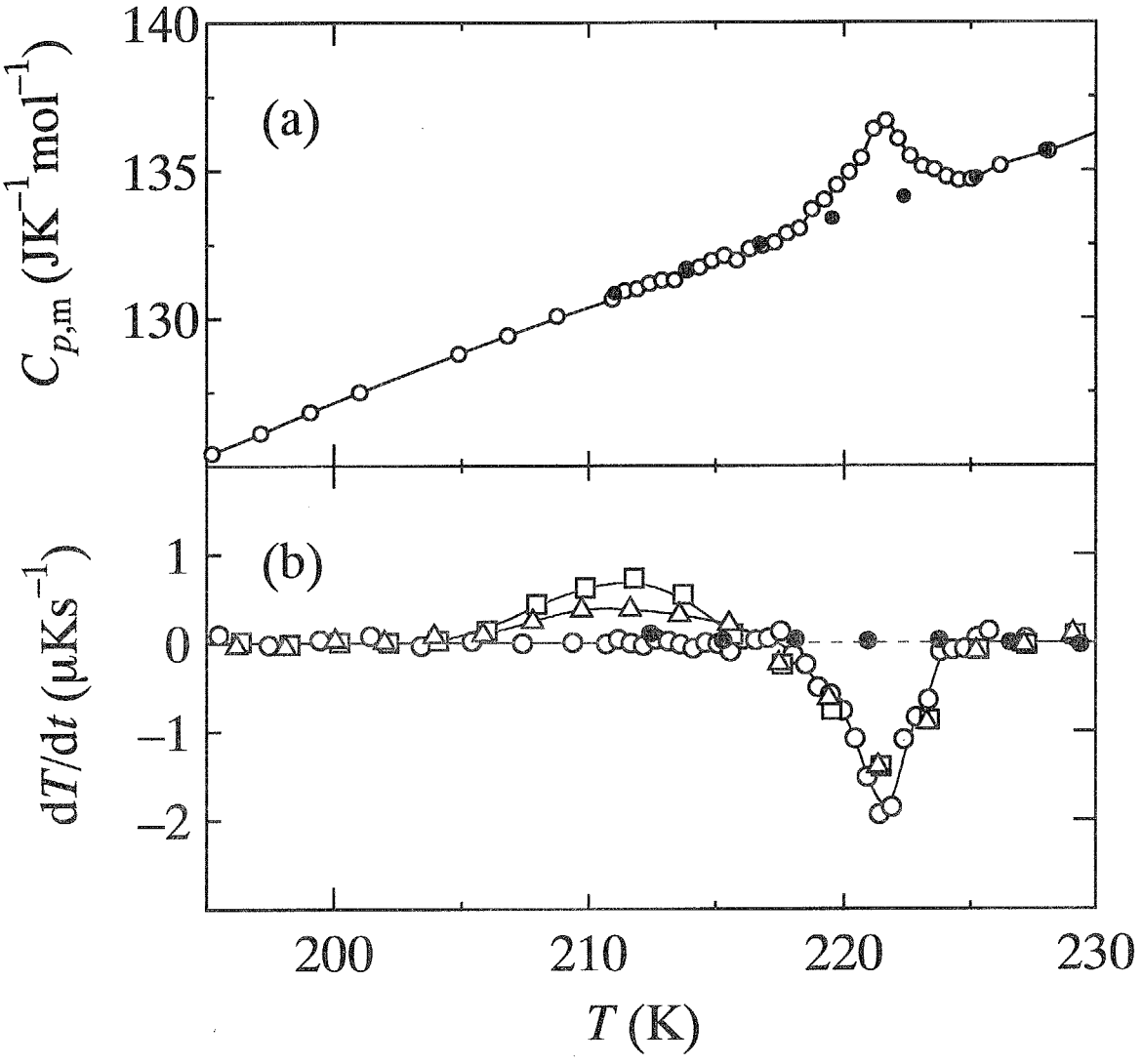

Figure 3.25: Thermal anomalies of $La_2CuO_{4.011}$ observed around 222 K in the intermittent heating process: (a), heat capacities; (b), spontaneous temperature drift rates; ●, precooled from 270 K to 212 K; □, △, ○, annealed at 210 K for 0, 4, and 50 h, respectively, after the precooling from 270 K to 180 K.

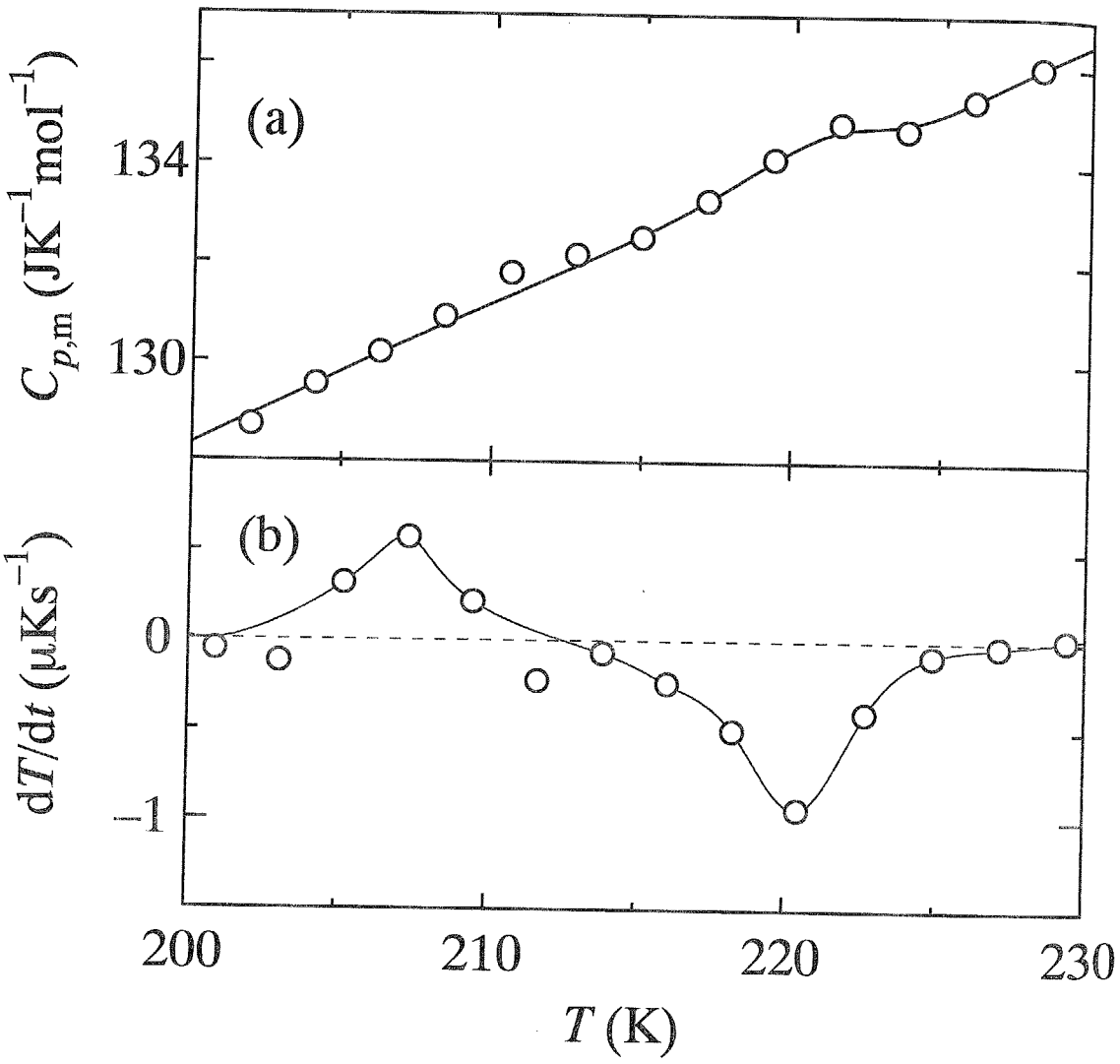

Figure 3.26: Thermal anomalies observed around 222 K in the intermittent heating process for the rapidly cooled sample of $La_2CuO_{4.035}$: (a), heat capacities; (b), spontaneous temperature drift rates.

anomaly is understood to be caused by the same first-order structural phase transition as observed in $La_2CuO_{4.011}$ crystal.

3.3.6 Stabilization phenomenon and structural phase transitions of a displacive type in $La_2CuO_{4.05}$ and $La_2CuO_{4.07}$ crystals

Figures 3.27(a) and 3.27(b) show spontaneous temperature-drift rates observed in the heat capacity measurements of $La_2CuO_{4.05}$ and $La_2CuO_{4.07}$ crystals in the range 300-400 K. Squares represent the values obtained on heating the samples prepared at room temperature by electrochemical oxidation. Both the samples exhibited a heat evolution effect starting at around 330 K. Circles represent the values obtained on heating the samples annealed at 400 K for 60 h and 120 h, respectively. The annealed sample exhibited no heat evolution nor heat absorption effect in the range 300-400 K any more. Therefore, it is indicated that the heat evolution effect observed in the as-prepared sample is due to irreversible stabilization from a quasi-stable (potentially meta-stable) phase to a stable phase. Figure 3.28 shows the spontaneous temperature drift curve of $La_2CuO_{4.05}$ crystal observed at around 400 K immediately after the series of heat capacity measurements for the as-prepared sample were carried out from 300 K to 400 K. The temperature change, ΔT, due to the stabilization amounts to ~1.7 K. The magnitude of heat evolution, ΔH_m, is evaluated as the sum of two contributions as follows. The first contribution is estimated from heat evolution observed during the heat capacity measurements from 300 K to 400 K to be

$$\Delta H_{m,1} = \int C_{total}/n \; (dT/dt) \; dt \approx 0.2 \text{ kJmol}^{-1}, \tag{3.10}$$

where C_{total} and n are gross heat capacity and the quantity of sample, respectively. The second contribution is estimated from the heat evolution observed during the annealing at 400 K to be

$$\Delta H_{m,2} = C_{total}(400 \text{ K})\Delta T/n \approx 0.9 \text{ kJmol}^{-1}. \tag{3.11}$$

The total enthalpy change is thus estimated to be $\Delta H_m = \Delta H_{m,1} + \Delta H_{m,2} \approx 1.1$ kJmol^{-1}.

Figures 3.29(a) and 3.29(b) show molar heat capacities of $La_2CuO_{4.05}$ and $La_2CuO_{4.07}$

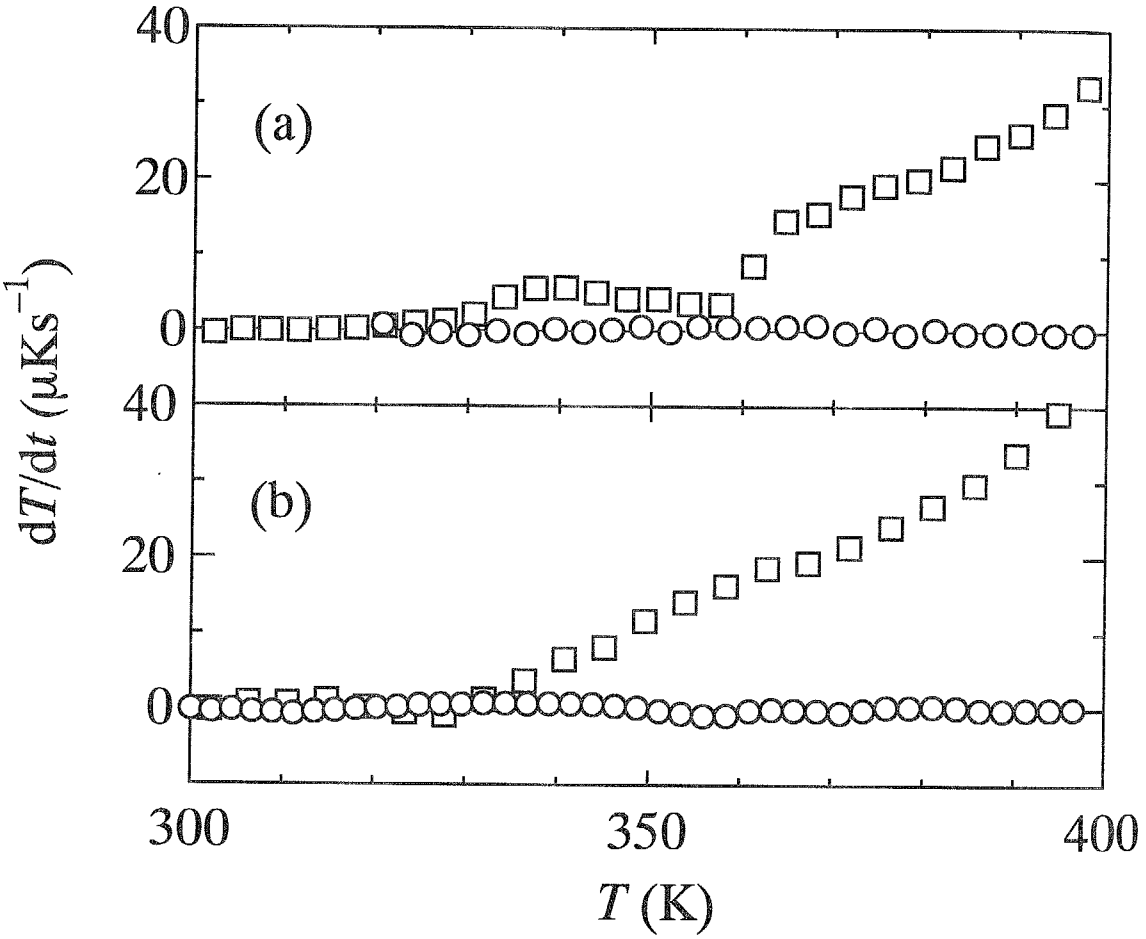

Figure 3.27: Spontaneous temperature-drift rates observed in the heat capacity measurements: □, as-prepared sample; ○, sample annealed at 400 K: (a) $La_2CuO_{4.05}$; (b) $La_2CuO_{4.07}$.

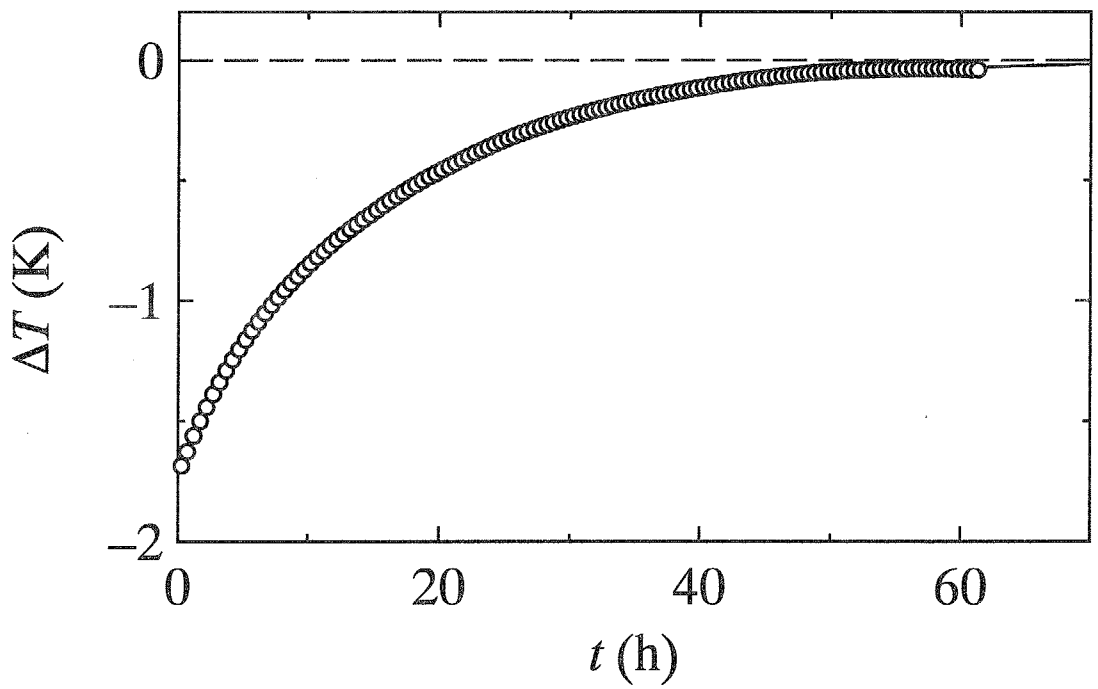

Figure 3.28: Spontaneous temperature-drift curve observed at 400 K immediately after the heat capacity measurements of the as-prepared $La_2CuO_{4.05}$ crystal from 300 K to 400 K.

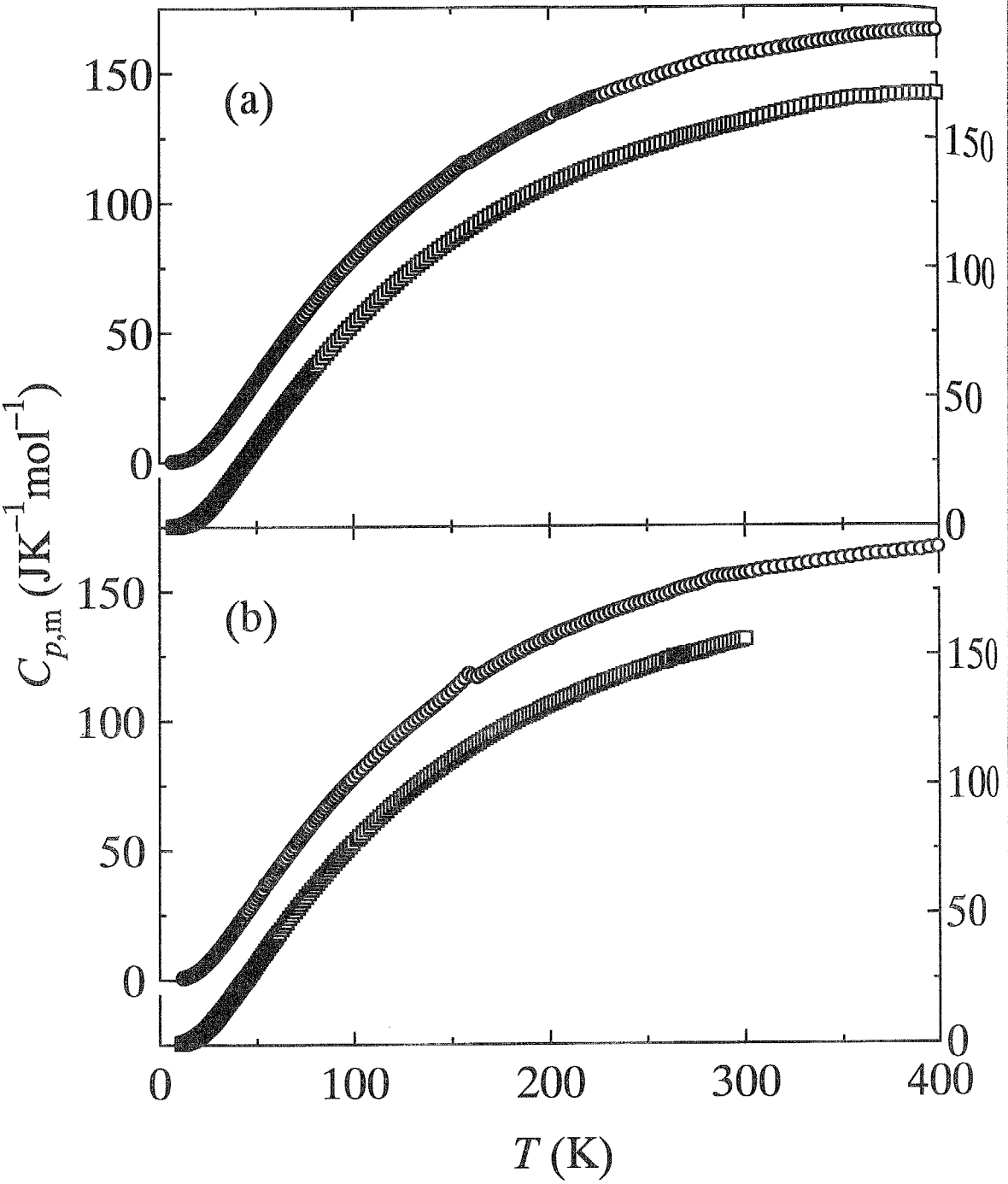

Figure 3.29: Molar heat capacities of (a) $La_2CuO_{4.05}$ and (b) $La_2CuO_{4.07}$: □, as-prepared sample; ○, sample annealed at 400 K. The results of the annealed sample were shifted upwards by 25 JK^{-1}mol^{-1}.

crystals, respectively. Squares and circles represent the values of as-prepared and stabilized samples, respectively. Both the as-prepared and stabilized samples of respective crystals showed a heat capacity anomaly due to a superconducting phase trasnition at around 41 K. The annealed samples of respective crystals showed two more heat capacity anomalies; one is due to a Martensitic phase transition at around 280 K and the other to a second-order phase transition at around 160 K. The two phase transitions were thus realized only through the stabilization above 330 K.

Figure 3.30 shows the heat capacities of the stabilized sample of $La_2CuO_{4.05}$ crystal in the range 250-310 K on an enlarged scale. The respective symbols in the figure represent the values obtained on heating the samples precooled from 320 K to the temperatures written in the figure. All of the five sets of data were located on different curves depending on the lowest temperature to which the sample was precooled before the measurements, and meanwhile no appreciable spontaneous temperature-drift was observed even just after the precooling nor during the heat capacity measurements on heating. It is therefore concluded that the phase transition is of a Martensitic type. The dashed line in the figure stands for a base line evaluated by interpolating the values in the ranges 200-250 K and 300-320 K. The enthalpy and the entropy of transition were estimated by using the base line to be 24 $Jmol^{-1}$ and 0.096 $JK^{-1}mol^{-1}$, respectively. In view of the smallness of the values, the transition is concluded to be of a displacive type.

Figures 3.31(a) and 3.31(b) show the heat capacities of stabilized samples of $La_2CuO_{4.05}$ and $La_2CuO_{4.07}$ crystals, respectively, in the range 140-170 K on an enlarged scale, where the respective symbols represent values obtained on heating the samples precooled from 200 K to the temperatures written in the figure.

Two or four series were located on the same curve independently of the lowest temperature to which the sample was precooled beforehand, and there was no spontaneous temperature-drift observed in the temperature range. The phase transition is thus concluded to be of a second-order type. The dashed line in the figure stands for a base line evaluated by interpolating the values in the ranges 50-100 K and 165-180 K. The enthalpy and the entropy of transition were estimated by using the base line to be 15 and 37 $Jmol^{-1}$

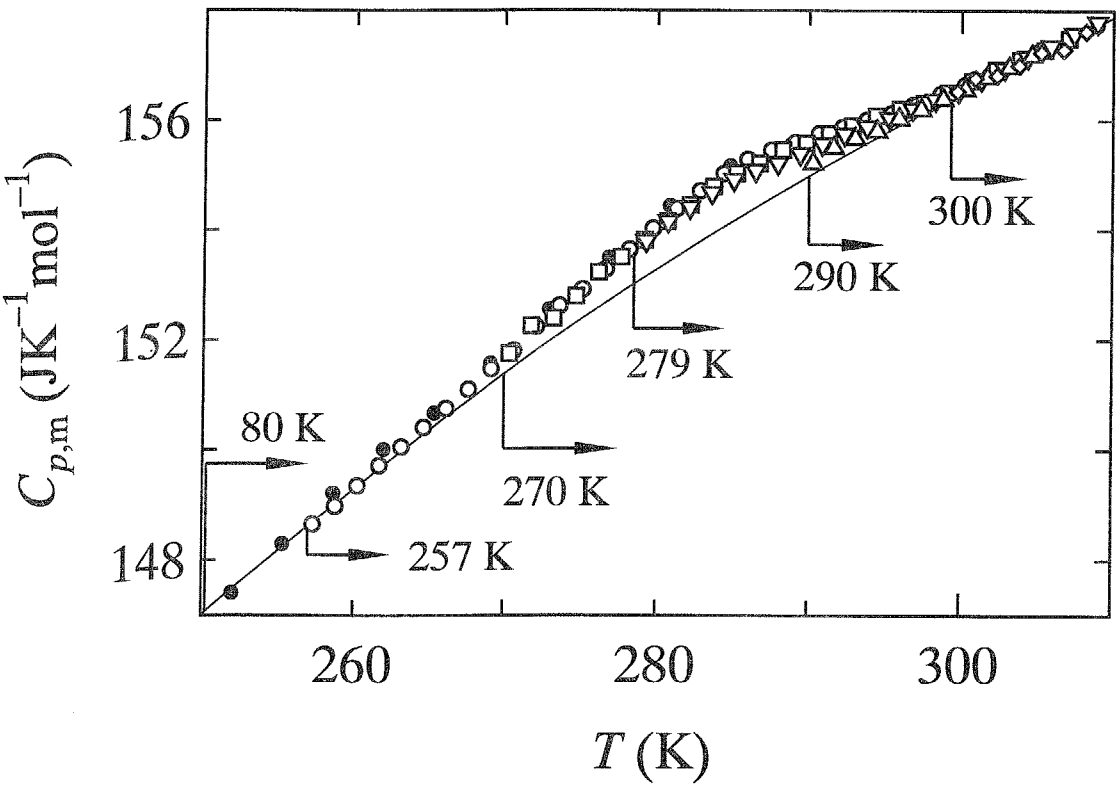

Figure 3.30: Molar heat capacities of $La_2CuO_{4.05}$ crystal plotted on an enlarged scale around 280 K. Temperatures written in the figure represent the lowest temperatures to which the samples were precooled from 320 K before each series of measurements.

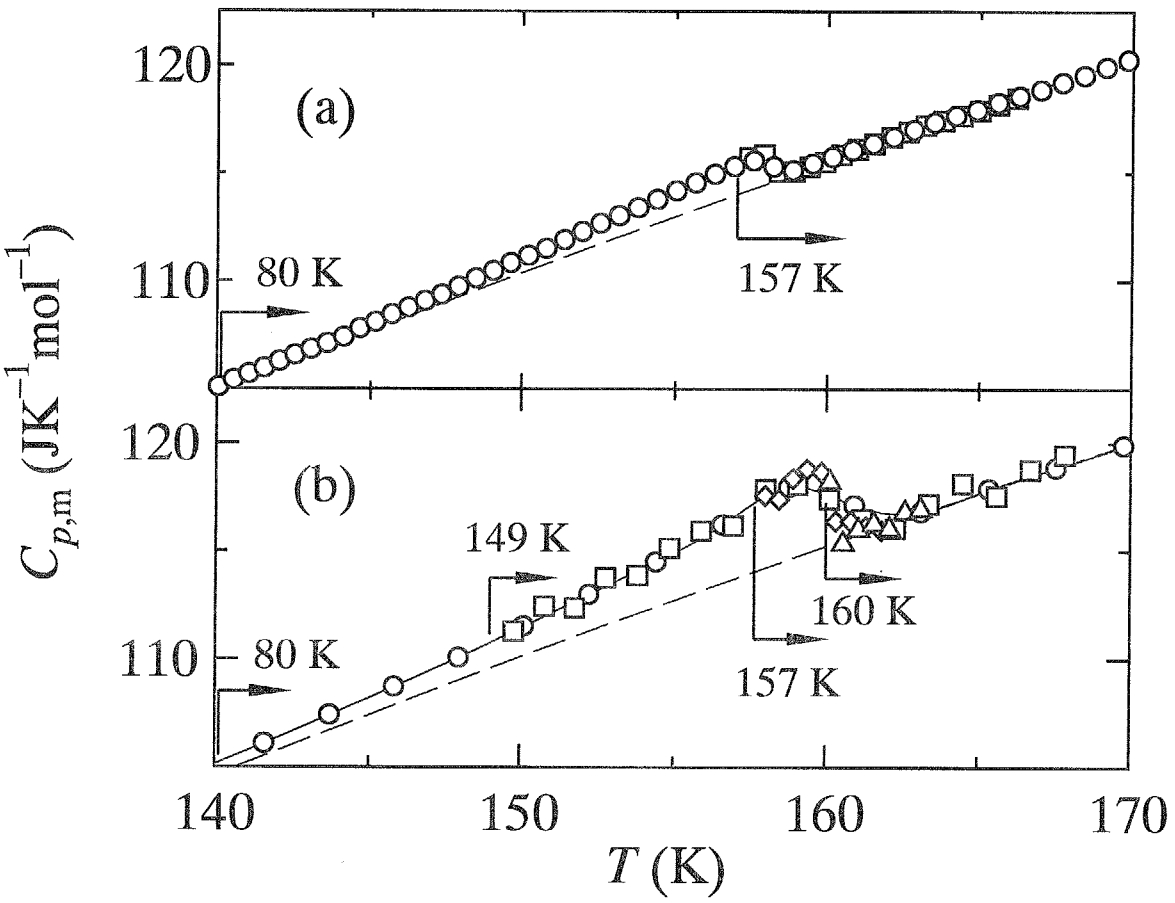

Figure 3.31: Molar heat capacities plotted on an enlarged scale around 160 K: (a) $La_2CuO_{4.05}$; (b) $La_2CuO_{4.07}$. Temperatures written in the figure represent the lowest temperatures to which the samples were precooled from 200 K before each series of measurements.

and 0.10 and 0.23 $JK^{-1}mol^{-1}$, respectively. Considering that the values are small, the transition is concluded also to be of a displacive type.

3.3.7 Superconducting phase transitions

No heat capacity anomaly was detected within the experimental error in the superconducting-transition temperature region in $La_2CuO_{4.011}$ and $La_2CuO_{4.035}$ crystals, but, on the other hand, the heat capacity anomalies were detected around 40 K in $La_2CuO_{4.05}$ and $La_2CuO_{4.07}$ crystals. This is understood to be due to the difference in the fraction of superconductive carriers.

This understanding is reasonable in view of the results of the magnetic susceptibility measurements; the magnitude of Meissner effect at 5 K of $La_2CuO_{4.07}$ crystal is about a hundred times larger than $La_2CuO_{4.011}$ crystal. In order to estimate the heat capacity jump, $\Delta_{trs}C_{p,m}$, associated with a superconducting phase transition, excess heat capacities, $\Delta C_{p,m}$, were calculated by subtracting the heat capacities of $La_2CuO_{4.002}$ crystal from the observed values. Squares and circles in Figs. 3.32(a) and 3.32(b) represent the excess encratics, $\Delta_{trs}C_{p,m}/T$, as the excess heat capacities divided by temperature for the as-prepared and stabilized samples, respectively, in the range 20-50 K. The superconducting phase transition was observed as showing a jump at around 41 K in the both samples. The magnitudes of the encraty jump of $La_2CuO_{4.05}$ and $La_2CuO_{4.07}$ crystals are estimated to be 10 and 18 $mJK^{-2}mol^{-1}$ for the as-prepared samples and 5 and 8 $mJK^{-2}mol^{-1}$ for the stabilized samples, respectively. The values of as-prepared samples are similar to those, 1.73~7.67 $mJK^{-2}mol^{-1}$, of $La_{2-x}Sr_xCuO_4(0.10 \leq x \leq 0.16)$ crystals,[67] but, on the other hand, the values of annealed samples are relatively large.

3.3.8 Glass transition due to freezing-in of rearrangement of excess oxygen atoms and activation energy for the positional jump of the oxygen atom

Solid and open circles in Fig. 3.33 represent the values of spontaneous temperature-drift rates observed in two series of measurements of $La_2CuO_{4.05}$ crystal for the sample stabi-

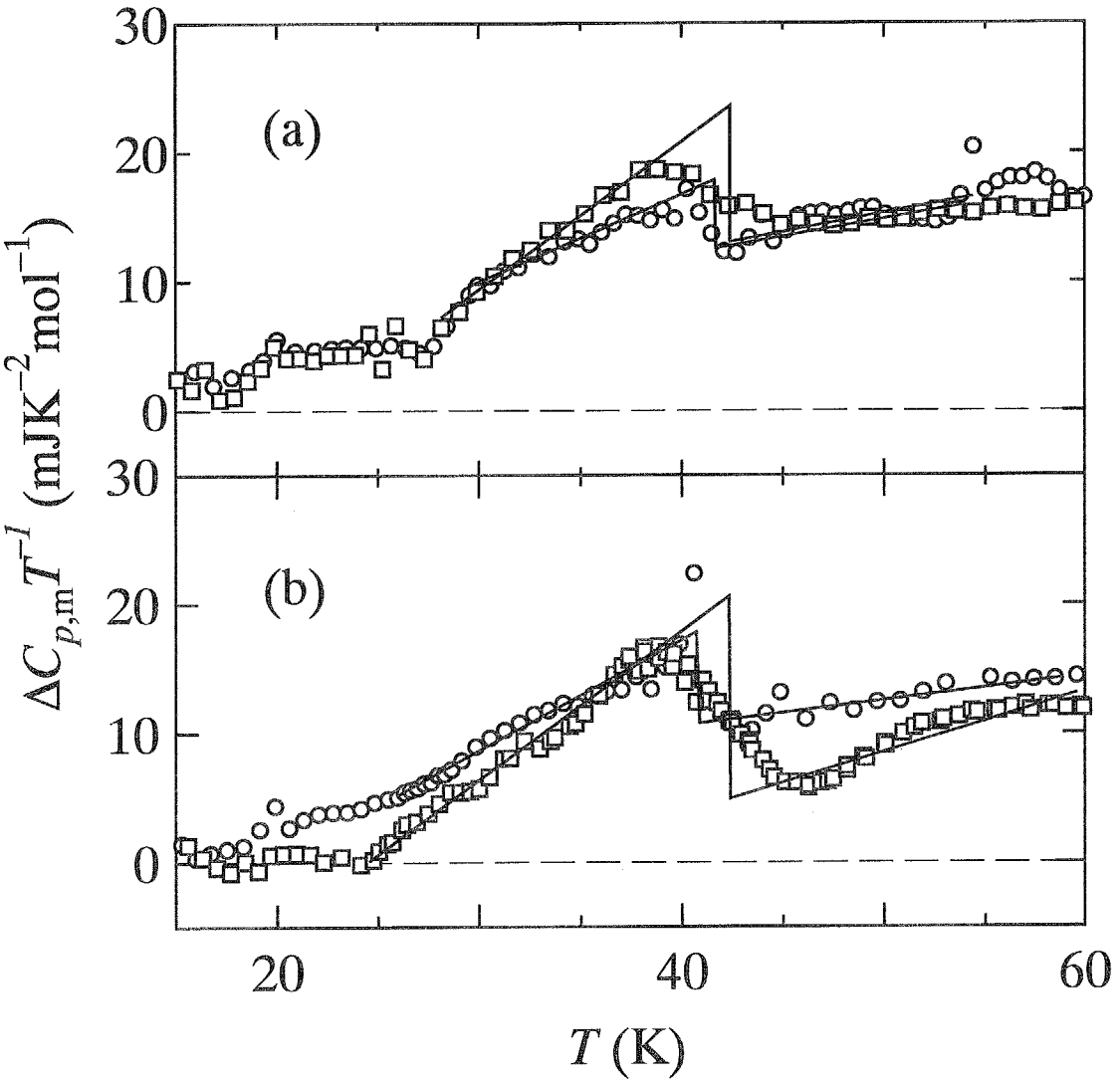

Figure 3.32: Excess encraties around superconducting phase transition temperatures for (a) $La_2CuO_{4.05}$ and (b) $La_2CuO_{4.07}$: □, as-prepared sample; ○, sample annealed at 400 K.

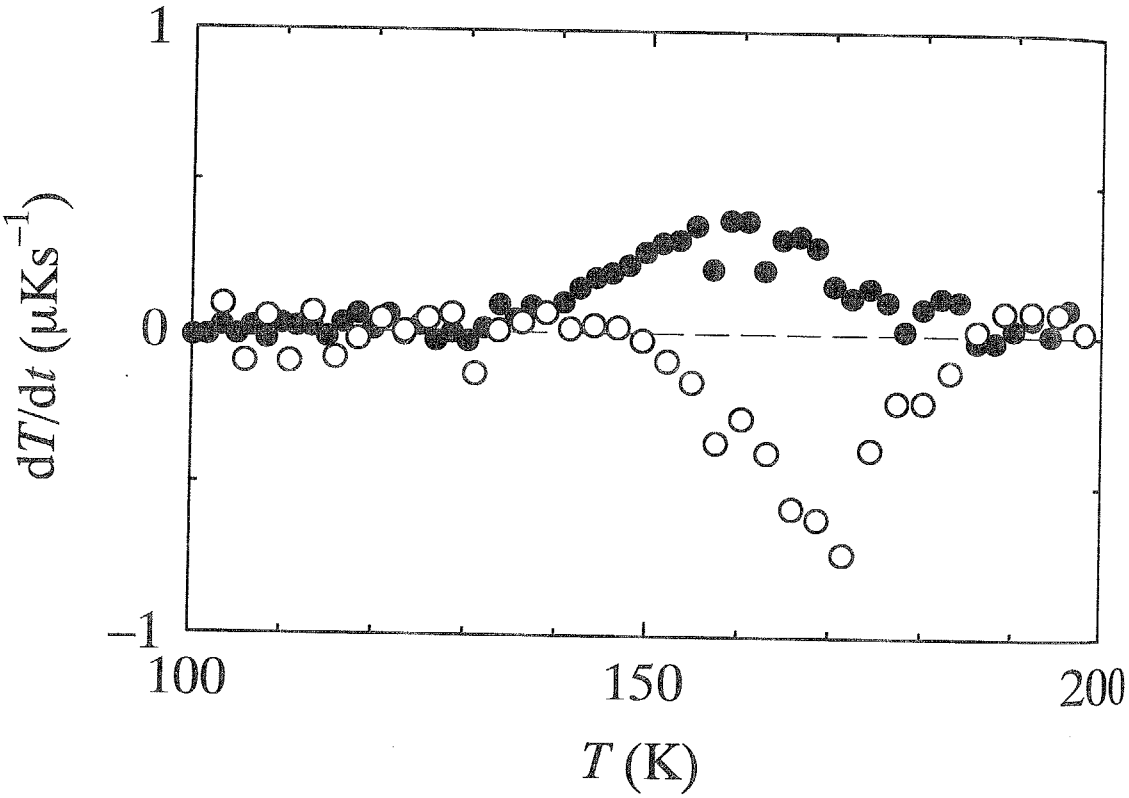

Figure 3.33: Spontaneous temperature-drift rates observed in the series of heat capacity measurements for the $La_2CuO_{4.05}$ crystal stabilized at 400 K: ●, sample precooled rapidly at 1 $Kmin^{-1}$; ○, sample precooled slowly at 20 $mKmin^{-1}$.

lized at 400 K and subjected to precooling treatment at 1 $Kmin^{-1}$ and at 20 $mKmin^{-1}$, respectively, from 200 K to 100 K. The rapidly precooled sample exhibited a heat evolution effect starting at 140 K and ending at around 190 K, and the slowly precooled sample a heat absorption effect starting at 145 K and ending at around 190 K. The heat evolution and absorption effects are not associated with the phase transition at 158 K, because the temperature of the heat absorption peak, 170 K, is clearly separate from the transition temperature. The fact that a heat evolution effect observed in the rapidly precooled sample changed to a heat absorption effect in the slowly precooled sample leads to a conclusion that the heat evolution and absorption effects are due to a glass transition. The glass transition temperature, T_g, at which the relaxation time is 10^3s was determined to be 170 K from an empirical relation, according to which the slowly precooled sample exhibited a heat absorption peak.

The activation energy, $\Delta\varepsilon_a$, for the positional jump of excess oxygen atom is estimated as follows. The relaxation time, τ, and frequency, f, for the jump are connected by the relation

$$f = 1/2\pi\tau. \tag{3.12}$$

The jump frequency is expressed by

$$f = \nu \exp(\Delta S_a/R) \exp(-\Delta\varepsilon_a/RT). \tag{3.13}$$

where ν, ΔS_a, and R are frequency of translational vibration of excess oxygen atoms, activation entropy and gas constant, respectively. Both of the $\Delta\varepsilon_a$ and ΔS_a are usually considered to be independent of temperature. ν is expected to be close to the Debye frequency, 1.02×10^{13} Hz, which was estimated from the molar heat capacity value at the glass transition temperature by assuming the crystal as a continuous solid composed of $7.05 \times N_A$ atoms, where N_A is Avogadro number. ΔS_a can be estimated according to Zener theory;[68, 69]

$$\Delta S_a \approx -\Delta\varepsilon_a \frac{d(B/B_0)}{dT}, \tag{3.14}$$

where B and B_0 are bulk moduli at T and 0 K, respectively. Average value of $d(B/B_0)/dT$ between 47 K and 310 K is calculated to be -4.21×10^{-5} from the data of bulk modulus.[70]

Using these values of $d(B/B_0)/dT$ and ν and considering the fact that the relaxation time at T_g is 10^3s, the activation energy for the jump of excess oxygen atom is estimated according to eqs. (3.12)-(3.14) to be $\Delta\varepsilon_a = 55.1$ kJmol^{-1}, and the relaxation time is expressed by

$$\tau = \tau_0 \exp(\Delta\varepsilon_a/RT) \tag{3.15}$$

with $\tau_0 = 1.18 \times 10^{-14}$s which is reasonable from the values hitherto found.[71]

Chapter 4

Discussion

4.1 $La_2NiO_{4+\delta}$ system

4.1.1 Structural phase transitions of a successive type in $La_2NiO_{4.00}$ crystal

First, let us number the respective phases of $La_2NiO_{4.00}$ crystal in the order of decreasing temperature for clarity;

$$\text{V}\ (T_2 = 80\ \text{K})\ \text{IV}\ (T_1 = 150\ \text{K})\ \text{III}\ (T_\text{N} = 330\ \text{K})\ \text{II}\ (T_0 = 650\ \text{K})\ \text{I}.$$

T_0 represents the temperature of $I4/mmm$-to-$Bmab$ phase transition stated in section 1.1.2. The V-to-IV and IV-to-III phase transitions would be interpreted as due to variation in the tilts of NiO_6 octahedra as stated in section 1.1.2. The successive (V-to-IV and IV-to-III) phase transitions displayed a heat capacity curve and characters, as shown in Fig. 3.3, quite similar to those of a type of (locked-in commensurate)-to-incommensurate-to-(normal commensurate) phase sequence.[72, 73, 74, 75] The first transition is known to have a first-order character, showing the mixed phases around T_2[23, 24, 59, 60] and a relatively sharp heat capacity peak. The second transition, on the other hand, showed a heat-capacity anomaly of a second-order type as described above. Such a successive type of anomalies has been found in some systems such as Rb_2ZnCl_4,[72, 73] thiophene[74, 75] and chlorocyclohexane.[57] In most of the systems, a remarkable impurity-doping effect has been observed with respect to the (locked-in commensurate)-to-incommensurate phase

transition; namely, the heat capacity anomaly due to the transition broadens and then disappears with doping with a small amount of impurity: The reason is that a number of different configurational structures are allowed as the incommensurately modulated states only with a little difference in the energies and thus different structures can be pinned easily by the presence of impurities. In this respect, it is noticed that no structural phase transition at T_2 has been observed in $La_2NiO_{4.02}$ crystal with only a little amount of excess oxygen atoms.[76] Therefore, the interpretation that the successive (V-to-IV and IV-to-III) phase transitions are classified as of a type of (locked-in superstructural commensurate)-to-incommensurate-to-(normal commensurate) phase sequence is reasonable at the present. The similar incommensurate phase has been observed in a compound, $(C_3H_7NH_3)_2MnCl_4$ with the same K_2NiF_4-type structure at high temperatures.[77]

In view of the facts that the IV-to-III phase transition is of the second order and that the space group of phase III is *Bmab*,[20] the only possible choice of the space group for the phase IV is *Pccn*, a subgroup of *Bmab* in the symmetry elements. There are two possibilities for the space group of phase V; *Pccn* and $P4_2/ncm$. The conclusive choice for that is difficult only from the present data, but considering that the transition at T_2 disappears in $La_2NO_{4.02}$,[76] the phase V is rather likely to be in the space group *Pccn*. The reason is that the transition between the phases in the incommensurate *Pccn* and $P4_2/ncm$ should have large jumps in the arrangements of tilts of NiO_6 octahedra and thus in the energies, in comparison with the transition between the phases in the incommensurate *Pccn* or superstructural *Pccn*, and the former is expected not to allow the emergence of incommensurate pinning effects by impurities and thus of fading-out of the locked-in commensurate-to-incommensurate phase transition. The interpretation is rather consistent with the experimental result by Hayashi *et al.*.[24] Therefore the following sequence of successive space groups is indicated in La_2NiO_4;

Locked-in superstructural *Pccn* (T_2) incommensurate *Pccn* (T_1) *Bmab*.

4.1.2 Phase relation in nonstoichiometric region

The δ-T phase diagram deduced from the present results is shown in Fig. 4.1. α designates the high-temperature phase in which excess oxygen atoms would be essentially in the disordered state as discussed in section 4.1.2. β, γ, ε, ζ and η designate the low-temperature phases with $\delta < 0.047$, $\delta \approx 0.07$, $\delta \approx 0.10$, $\delta \approx 0.14$, and $\delta > 0.154$, respectively. ε' designates the intermediate phase which appeared in between ε and α phases. The excess oxygen atoms would be arranged in the somehow ordered way in the low-temperature phases except for β phase as discussed in section 4.1.2

In the range $0.067 \leq \delta \leq 0.098$, rather sharp heat capacity peaks were observed at around 247 K as shown in Figs. 3.7(a), 3.9(a), and 3.11(a). The peak temperatures were essentially independent of the composition of excess oxygen atoms. A little difference observed in reality is within the experimental error in view of the aspect that equilibration time in the phase transition region was too long to obtain exact equilibrium heat capacities and thus the temperature of heat capacity peak. The magnitude of the peak was largest in $\delta = 0.073$ crystal and smallest in $\delta = 0.098$ crystal among the three. In addition, heat capacity anomalies were observed as shoulders at around 255 K and 270 K in $\delta = 0.067$ and 0.073 crystals, respectively, and as a sharp peak at 278 K in $\delta = 0.098$ crystal; namely, the anomalies became remarkable and the temperatures increased as the excess oxygen composition increased. The heat capacity peak at 250 K in $\delta = 0.116$ crystal seemed to correspond to that at 278 K in $\delta = 0.098$ crystal, but the temperature of peak is definitely lower at $\delta = 0.116$ than at $\delta = 0.098$. These observations are interpreted as characteristic of phase separation of a peritectoid type proceeding in the range $0.067 \leq \delta \leq 0.098$: Low-temperature-stable ε phase is formed at around $\delta = 0.10$ and peritectoid compound showing γ phase is produced at around $\delta = 0.07$. The sample with δ in between 0.07 and 0.10 is expected to be composed of the two crystals in the γ and ε phases at low temperatures. The γ-phase crystal decomposes at 247 K into high-temperature disordered α and low-temperature ordered ε phases. As the temperature increases, both the fraction and the composition δ of the α phase increase through the transition from ε to α phases.

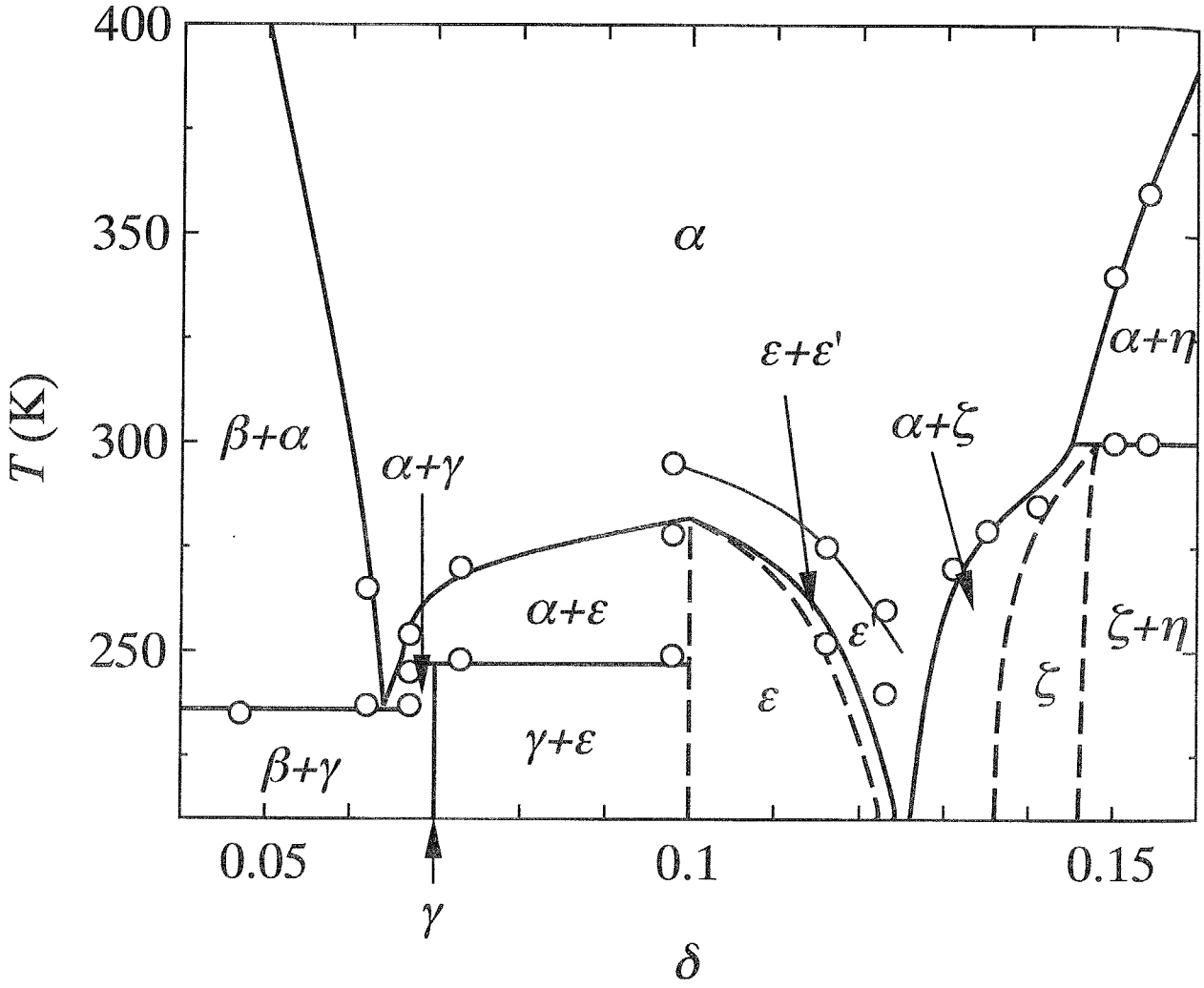

Figure 4.1: δ-T phase diagram of $La_2NiO_{4+\delta}$ crystal system deduced from the present calorimetric results. α denotes the high-temperature phase with excess oxygen atoms in the disordered arrangement, and β, γ, ε, ζ and η the low-temperature phases with the oxygen atoms arranged somehow in the ordered way.

In the range $0.047 \leq \delta \leq 0.067$, appreciably sharp peaks were observed at around 236 K as shown in Figs. 3.7(a), 3.9(a), and 3.11(a). The temperatures were essentially independent of the composition δ of excess oxygen atoms in the range. The magnitude of the peak appeared to be largest in $\delta = 0.062$ crystal among the three samples. The peaks are interpreted as attributed to a eutectoid reaction between the low-temperature β and γ phases. Heat capacity shoulder at 265 K in $\delta = 0.062$ crystal would be due to a phase separation between α and β phases. The eutectoid composition δ_e of excess oxygen atoms is expected potentially to be located in between $\delta = 0.062$ and 0.067, and in view of the fact that the heat capacities of $\delta = 0.047$ crystal in the range 235-340 K are larger than those of $\delta = 0.062$ crystal as seen from Fig. 3.9(a), the phase-separation temperature at $\delta = 0.047$ would be above 340 K. The latter of the understanding is consistent with the results of Tranquada *et al.*[29] and Tamura *et al.*[15] The crystals in the composition range $\delta_e < \delta < 0.07$ such as $\delta = 0.067$ crystal are expected to undergo following phase transitions: The two, β and γ, phases present at low temperatures show a eutectoid reaction at 236 K to transform to two, α and γ, phases. The γ phase transforms at 247 K into α and ε phases through a peritectoid decomposition, and the whole crystal becomes α phase with uniform composition δ of excess oxygen atoms at some temperature above 247 K.

In the range $0.098 \leq \delta \leq 0.123$, heat capacity anomalies were observed as a sharp peak at 278 K, 250 K, and 240 K and as a shoulder at around 290 K, 270 K, and 260 K in $\delta = 0.098$, 0.116, and 0.123 crystals, respectively, as shown in Figs. 3.7(b), 3.9(b), and 3.11(b). Though the two successive phase transitions are similar to those observed in $\delta = 0.073$ crystal, the sharp anomalies observed in this region are not peritectoid or eutectoid transition because the both temperatures depend on the excess oxygen composition. The successive α-to-ε' and ε'-to-ε phase transitions are discussed in section 4.1.3.3. In the range $0.131 \leq \delta \leq 0.141$, relatively broad heat capacity anomalies were observed at 270 K and 278 K in $\delta = 0.131$ and 0.135 crystals, and relatively sharp anomaly was observed at 285 K in $\delta = 0.141$ crystal as shown in Figs. 3.7(b), 3.9(b), and 3.11(b). In view of the fact that, with increasing the excess oxygen composition, the temperatures of phase transitions

in the range $0.098 \leq \delta \leq 0.123$ decrease, but, on the other hand, the temperatures of those in the range $0.131 \leq \delta \leq 0.141$ increase, it is indicated that the phase diagram in the range $0.10 < \delta < 0.14$ is a eutectoid type. But a eutectoid reaction the temperature of which should be independent of the excess oxygen composition was not observed in the present study. This observation is reasonable provided that the temperature of eutectoid reaction is lower than the glass transition temperature and thus the reaction does not occur within the experimental time scale. This understanding is consistent with the fact that the heat capacity anomalies observed in $\delta = 0.131$ and 0.135 crystals tail on the low temperature side. On the other hand, the heat capacity anomalies observed in $\delta = 0.116$, 0.123, and 0.141 crystals are relatively sharp. According to the above understanding, it follows that the δ values of these crystals are beyond the phase separation region at low temperatures; namely, the low temperature states of $\delta = 0.116$ and 0.123 crystals are composed of only ε phase, the low temperature state of $\delta = 0.141$ crystal is composed of only ζ phase, and thus the ε and ζ phases show nonstoichiometry as shown in Fig. 4.1.

In the range $0.150 \leq \delta \leq 0.154$, sharp anomalies were observed at 300 K which is independent of excess oxygen composition, and broad anomalies were observed at around 340 K and 360 K in $\delta = 0.150$ and 0.154 crystals, respectively, as shown in Figs. 3.7(b), 3.9(b), and 3.11(b). These anomalies have a typical shape of phase transition of a peritectoid or eutectoid type. Considering that the temperature of phase transition does not show a maximum in the range $0.131 \leq \delta \leq 0.154$, it is plausible that the phase diagram in the range $\delta \leq 0.150$ is of a peritectoid type as shown in Fig. 4.1.

4.1.3 Ordering processes and positional arrangements of excess oxygen atoms

4.1.3.1 α phase

There are $2N_A$ interstitial sites per mole of La_2NiO_4, where N_A is Avogadro's number. Provided that excess oxygen atoms are arranged in the disordered way among the interstitial sites, the entropy due to permissible positional arrangements of excess oxygen atoms

in the completely disordered state is expressed by

$$\begin{aligned} S_{\mathrm{O},1} &= k_{\mathrm{B}} \ln\{{}_{2N_{\mathrm{A}}}\mathrm{C}_{\delta N_{\mathrm{A}}}\} \\ &\approx -2R\left\{\frac{\delta}{2}\ln\frac{\delta}{2} + \left(1-\frac{\delta}{2}\right)\ln\left(1-\frac{\delta}{2}\right)\right\}, \end{aligned} \tag{4.1}$$

where k_{B} and R are Boltzmann constant and gas constant, respectively. The values at different δ's are tabulated in Table 4.1. They are much larger than the observed entropies of phase transition tabulated in Table 3.3. This means that the excess oxygen atoms are not completely disordered in the α phase and/or not completely ordered in the γ, ε, and ζ phases. However, in view of the facts that the δ values in the crystals used in the present study correspond only to the occupation fractions of 0.03~0.08 to the whole interstitial sites accessible to the excess oxygen atoms in the α phase and that a high-temperature tail of the anomalous heat capacities due to the phase transitions was not observed as seen from Figs. 3.7 or 3.9, the excess oxygen atoms are expected to be rather in the completely disordered state in the α phase. It follows therefore that the excess oxygen atoms are not arranged in the completely ordered way in the γ, ε, and ζ phases.

4.1.3.2 γ phase

Tranquada *et al.*[29] have observed $(0,1,\frac{1}{3})$ superlattice peaks based on the γ phase in $\delta = 0.074$ crystal in addition to $(0,1,\frac{1}{2})$ superlattice peaks based on the ε' or ε phase owing to the phase separation. They suggested from the analysis of the superlattice peaks that excess oxygen atoms are arranged to form stage-3 structure of the orthorhombic system in the γ phase. The structure was denoted as intercalated *Bmab* the unit cell of which is shown in Fig. 4.2. The NiO_6 octahedra rotate without their deformation about a-axis similarly to *Bmab* structure as shown in Fig. 1.3, but the phase of the tilt modulation in the c-direction reverses at every layer in which excess oxygen atoms are accomodated. Accessible sites to the excess oxygen atoms in the stage-3 structure are represented by open circles in the figure. As seen from the figure, within a layer in which the excess oxygen atoms are accomodated, the apical oxygen and lanthanum atoms located nearest to the accessible site move away from the accessible site along the b-axis, and consequently

Table 4.1: Entropies evaluated with respect to the permissible arrangements of excess oxygen atoms in completely disordered state for $La_2NiO_{4+\delta}$ crystals

δ	$S_{O,1}$ ($JK^{-1}mol^{-1}$)
0.062	2.30
0.067	2.44
0.073	2.61
0.098	3.25
0.116	3.68
0.123	3.84
0.131	4.02
0.135	4.11
0.141	4.24
0.150	4.43
0.154	4.51

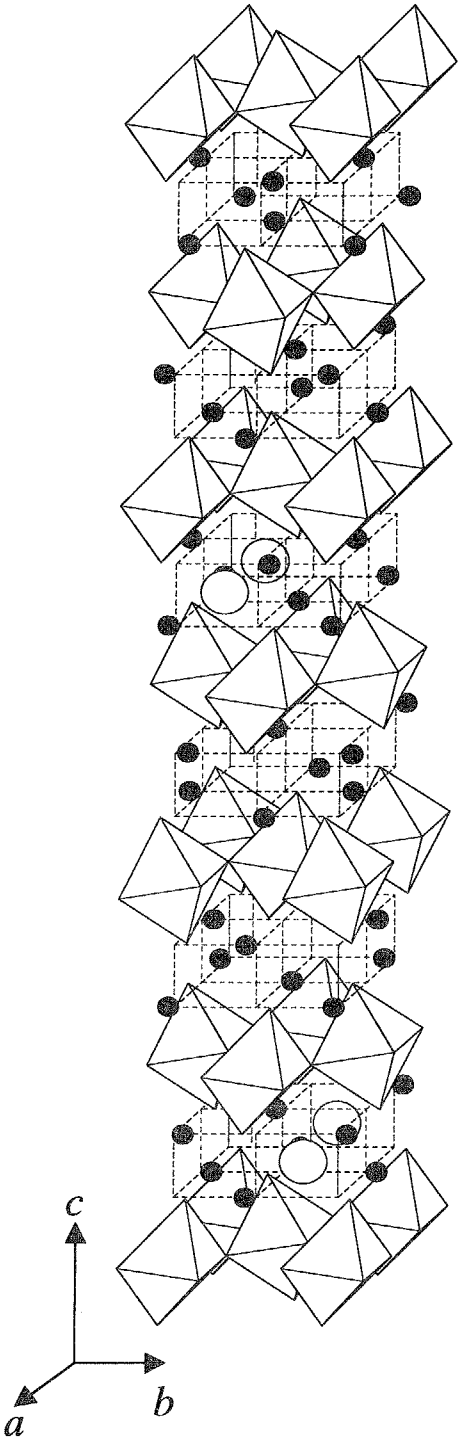

Figure 4.2: Unit cell of stage-3 intercalated *Bmab* structure. Octahedra, solid and open circles represent NiO_6 octahedra, lanthanum, and excess oxygen atoms, respectively. Nickel atoms are omitted in the figure for clarity. The accessible sites to excess oxygen atoms form lines along the a-axis, and the excess oxygen atoms are expected to be arranged rather randomly among the sites in the line. The occupation fraction of the excess oxygen atoms to the accessible sites is about 0.2.

these atoms come close to the next interstitial site, along the b-axis, otherwise accessible to excess oxygen atom. This makes it impossible for excess oxygen atoms to be accomodated into the interstitial sites; namely, the accessible sites to excess oxygen atoms form a line along the a-axis and only every alternate, along the b-axis, line of the sites can be available to the excess oxygen atoms. Thus, according to their structural model, the number of accessible sites to the excess oxygen atoms is subjected to the restriction to amount to $N_{\rm A}/3$ in the stage-3 structure per mole of La_2NiO_4. Provided that the excess oxygen atoms are arranged in the disordered way among the restricted accessible sites, the entropy based on permissible positional arrangements of excess oxygen atoms in the stage-3 structure is expressed by

$$\begin{aligned} S_{\rm O,3} &= k_{\rm B} \ln\{{}_{N_{\rm A}/3}{\rm C}_{\delta N_{\rm A}}\} \\ &\approx -\frac{R}{3}\{3\delta \ln(3\delta) + (1-3\delta)\ln(1-3\delta)\}\,. \end{aligned} \tag{4.2}$$

The phase transition in $\delta = 0.073$ crystal is recognized rather to be of the γ to α phases. The entropy of $S_{\rm O,3}$ amounts to 1.46 $\rm JK^{-1}mol^{-1}$ for $\delta = 0.073$ crystal. The expected entropy of γ-to-α phase transition for the $\delta = 0.073$ crystal is evaluated, by subtracting $S_{\rm O,3}$ from $S_{\rm O,1}$, to be around 1.15 $\rm JK^{-1}mol^{-1}$. The experimentally observed value is larger by 0.20 $\rm JK^{-1}mol^{-1}$ than the evaluated one. This means that the excess oxygen atoms are arranged in a somewhat ordered way in the short range. $\delta = 0.073$ corresponds to the occupation fraction of about 0.2 to the whole accessible interstitial sites within the layer in which the excess oxygen atoms are accommodated together; namely, the atoms are arranged every five sites on an average along the a-axis. Such an arrangement would exist as a rather preferred short-range order in the γ phase. The arrangement of atoms in the long range is, of course, essentially in the disordered state.

In order to estimate the effect of short-range order in the arrangement of excess oxygen atoms on the entropy of the γ phase, the following problem is considered here; When n atoms are arranged on the sites of a ring in which there are N sites as shown in Fig. 4.3(a), what is the number of permissible arrangements of atoms under the restriction (a) that any atom can not be located at nearest-neighbor sites of the other atoms? The

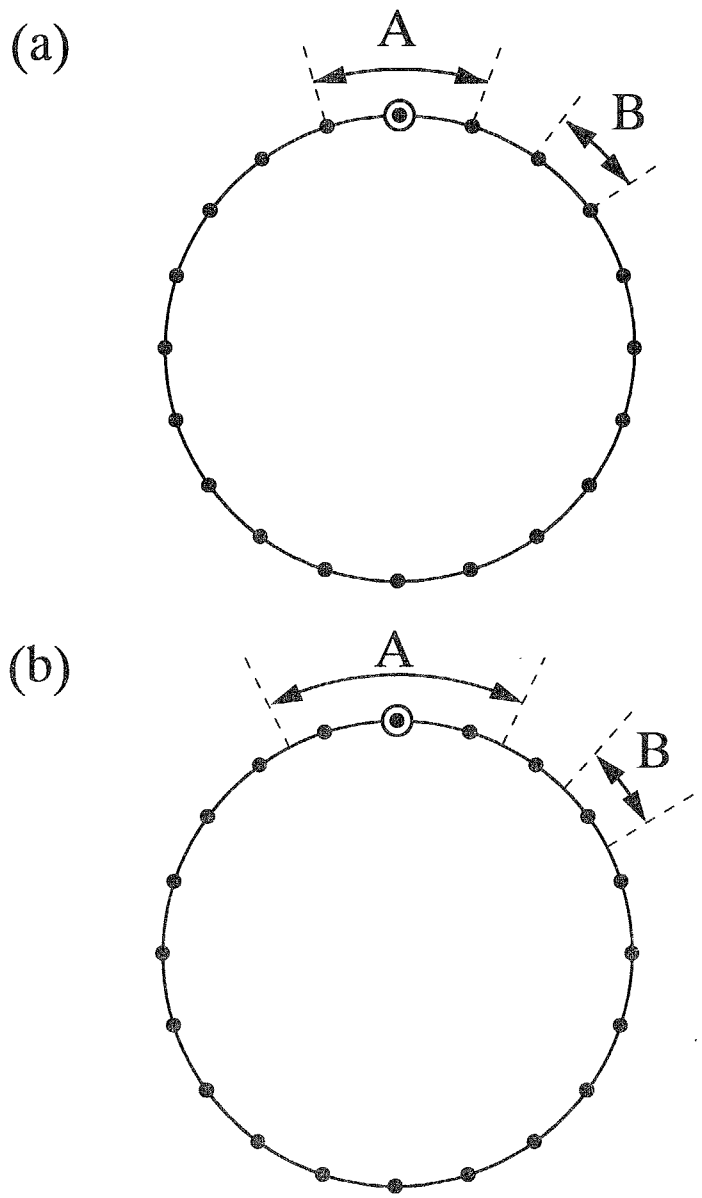

Figure 4.3: Model for estimating short-range order present in the arrangement of n atoms distributed among N accessible sites: (a), no atom can occupy the nearest-neighbor sites to that occupied by the other atoms; (b), no atom can occupy the next nearest-neighbor as well as the nearest neighbor sites to that occupied by the other atoms. In (a), the ring composed of N accessible sites, represented by dots, is recognized to be composed of N elemental line-segments represented by arrow B. Arrow A represents a line segment composed of two successive elemental line-segments, and indicates that a site represented by a circle with dot is occupied by an atom. In (b), the ring composed of N accessible sites is recognized to be composed of N elemental line-segments represented by arrow B. Arrow A represents a line segment composed of three successive elemental line segments, and indicates that a mid site, represented by a circle with dot, in the line segment is occupied by an atom.

restriction (a) is plausible for the case of $La_2NiO_{4+\delta}$ crystal because repulsive coulomb interaction should act between excess oxygen atoms(O^{2-} ions). The number of arrangements under the restriction (a) is evaluated exactly as follows. It is considered that the ring is composed of N elemental line-segments (of type B), each line-segment being made by linking the two nearest neighbor sites on the ring, as represented by arrow B in Fig. 4.3(a). When an atom is located on a certain site of the ring as indicated by an open circle in Fig. 4.3(a), the situation is defined by the line-segment (of type A) composed of two successive elemental line-segments linked to the site occupied by the atom, as represented by arrow A in Fig. 4.3(a). The two elemental line-segments included in the arrow A are never overlapped by the segments due to the other atoms under the restriction (a), because any atom can not occupy the nearest-neighbor site of the atom. It is thus considered that the ring is composed of n line-segments of type A and $(N-2n)$ elemental line-segments of type B. The above problem is then reduced to counting the number of permissible arrangements, in the ring, of n line segments of type A and $(N-2n)$ elemental line-segments of type B. The number is expressed by ${}_{N-n}C_n$. Next, imagine the three-dimensional lattice composed of $(2N_A)^{\frac{1}{3}} \times (2N_A)^{\frac{1}{3}} \times (2N_A)^{\frac{1}{3}}$ lattice points which correspond to interstitial sites for excess oxygen atoms in $La_2NiO_{4+\delta}$ crystal. In the stage-3 structure of the γ phase, a line of the interstitial sites along the a-axis in the lattice form the accessible sites to excess oxygen atoms, and the line may be considered as an above-stated ring with $N = (2N_A)^{\frac{1}{3}}$ and $n = 3\delta(2N_A)^{\frac{1}{3}}$ if the problem of the ends of the line is ignored. Because there are $(2N_A)^{\frac{2}{3}}/6$ lines of the accessible interstitial sites in the lattice for the stage-3 structure, the entropy based on the permissible positional arrangements of excess oxygen atoms is expressed by,

$$\begin{aligned} S_{O,3}^{(a)} &= k_B \ln \left\{ {}_{(1-3\delta)(2N_A)^{\frac{1}{3}}}C_{3\delta(2N_A)^{\frac{1}{3}}} \right\}^{(2N_A)^{\frac{2}{3}}/6} \\ &\approx -\frac{1-3\delta}{3} R \left\{ \left(\frac{3\delta}{1-3\delta} \right) \ln \left(\frac{3\delta}{1-3\delta} \right) + \left(\frac{1-6\delta}{1-3\delta} \right) \ln \left(\frac{1-6\delta}{1-3\delta} \right) \right\}. \end{aligned} \quad (4.3)$$

The evaluated value $S_{O,3}^{(a)}$ for $\delta = 0.073$ is 1.28 $JK^{-1}mol^{-1}$, and the transition entropy is evaluated, by subtracting this value from $S_{O,1}$, to be 1.33 $JK^{-1}mol^{-1}$, which is very close

to the experimental value. Therefore, it is concluded that there exists a short-range order of excess oxygen atoms in the γ phase to the extent that the atoms do not approach the nearest-neighbor accessible sites one another.

4.1.3.3 ε' and ε phases

Tranquada *et al.*[29] have observed $(0,1,\frac{1}{2})$ superlattice peaks below 290 K in $\delta = 0.105$ crystal, though not observed successive α-to-ε'-to-ε phase transitions discovered in the present study. They suggested that the excess oxygen atoms are arranged to form stage-2 structure in the low-temperature phase as shown in Fig. 4.4, the tilt pattern of which within each layer of accessible sites to the excess oxygen atoms is the same as that in the stage-3 structure. Thus, provided that the excess oxygen atoms are arranged in the disordered way among the accessible sites, the entropy based on permissible positional arrangements of excess oxygen atoms in the stage-2 structure is expressed by

$$\begin{aligned} S_{\mathrm{O},2} &= k_{\mathrm{B}} \ln\{{}_{N_{\mathrm{A}}/2}\mathrm{C}_{\delta N_{\mathrm{A}}}\} \\ &\approx -\frac{R}{2}\{2\delta \ln(2\delta) + (1-2\delta)\ln(1-2\delta)\}\,. \end{aligned} \tag{4.4}$$

The phase transitions in $\delta = 0.098$ crystal are recognized rather to be of the ε through ε' to α phases. The entropy of $S_{\mathrm{O},2}$ amounts to 2.06 $\mathrm{JK^{-1}mol^{-1}}$ for $\delta = 0.098$ crystal. The expected entropies of (stage-2 phase)-to-α for the $\delta = 0.098$ crystal is evaluated, by subtracting $S_{\mathrm{O},2}$ from $S_{\mathrm{O},1}$, to be around 1.19 $\mathrm{JK^{-1}mol^{-1}}$. The experimentally observed value is larger by 0.58 $\mathrm{JK^{-1}mol^{-1}}$ than the evaluated one.

Two potential reasons would be considered for the difference between the experimental and above-evaluated transition entropies, as follows. First reason is because the presence of short-range order in the arrangement of excess oxygen atoms in the low-temperature phase is responsible similarly to that discussed in the case of γ(stage-3) phase. Suppose the lattice composed of $(2N_{\mathrm{A}})^{\frac{1}{3}} \times (2N_{\mathrm{A}})^{\frac{1}{3}} \times (2N_{\mathrm{A}})^{\frac{1}{3}}$ lattice points as in the discussion for the stage-3 structure. For the stage-2 structure, the line, along the a-axis, of accessible sites to excess oxygen atoms is also represented as the ring shown in Fig. 4.3(a) with $N = (2N_{\mathrm{A}})^{\frac{1}{3}}$ and $n = 2\delta(2N_{\mathrm{A}})^{\frac{1}{2}}$, and there are $(2N_{\mathrm{A}})^{\frac{2}{3}}/4$ lines of accessible

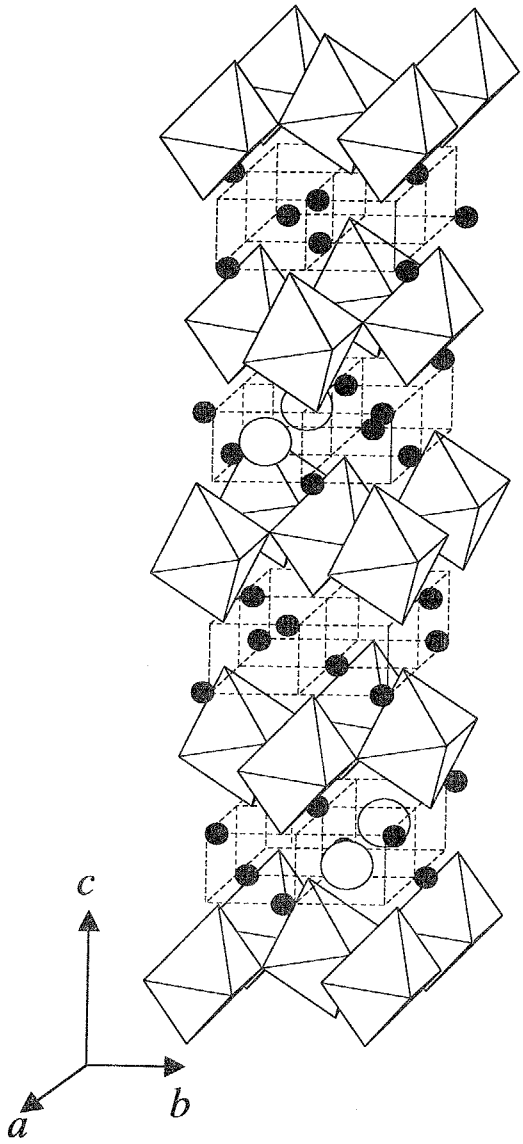

Figure 4.4: Unit cell of stage-2 intercalated *Bmab* structure. The occupation fraction of the excess oxygen atoms is about 0.2 which is the same as in the stage-3 structure.

sites in the lattice for the stage-2 structue. As one case, assume that the excess oxygen atoms are arranged on the lines under the restriction (a) as in the stage-3 structure. The entropy based on the permissible positional arrangements of excess oxygen atoms under the restriction (a) is expressed by

$$\begin{aligned} S_{\mathrm{O},2}^{(\mathrm{a})} &= k_{\mathrm{B}} \ln \left\{ {}_{(1-2\delta)(2N_{\mathrm{A}})^{\frac{1}{3}}}\mathrm{C}_{2\delta(2N_{\mathrm{A}})^{\frac{1}{3}}} \right\}^{(2N_{\mathrm{A}})^{\frac{2}{3}}/4} \\ &\approx -\frac{1-2\delta}{2} R \left\{ \left(\frac{2\delta}{1-2\delta} \right) \ln \left(\frac{2\delta}{1-2\delta} \right) + \left(\frac{1-4\delta}{1-2\delta} \right) \ln \left(\frac{1-4\delta}{1-2\delta} \right) \right\}. \end{aligned} \tag{4.5}$$

The evaluated $S_{\mathrm{O},2}^{(\mathrm{a})}$ for $\delta = 0.098$ is 1.86 $\mathrm{JK^{-1}mol^{-1}}$, and the transition entropy is calculated, by subtracting this value from $S_{\mathrm{O},1}$, to be 1.39 $\mathrm{JK^{-1}mol^{-1}}$, which is still smaller by 0.38 $\mathrm{JK^{-1}mol^{-1}}$than the experimental value. From the aspect that the interaction between excess oxygen atoms in the c-direction should be larger in the stage-2 structure than in the stage-3 structure (because the layers in which excess oxygen atoms are accomodated are closer to one another in the former structure), however, it is reasonable to consider that the short-range order develops more in the stage-2 structure than in the stage-3 structure. As another case for the potential short-range order, therefore, let us assume the restriction (b) that any excess oxygen atom can not occupy, in addition to the nearest neighbor, the next-nearest-neighbor sites of the other atoms. The ring is recognized to be composed of N elemental line-segments as represented by arrow B in Fig. 4.3(b). The elemental line-segment(type B) is made by linking the two neighboring points, each point being given by the mid point between the two neighboring sites. (It should be noted that the definition of the elemental line-segment is different from that in Fig. 4.3(a).) In this case, when an atom is located on a certain site of the ring, as indicated by an open circle in Fig. 4.3(b), the situation with the restriction (b) is defined by the line segment(type A) composed of three successive elemental line-segments as represented by arrow A in Fig. 3.4(b). Thus, the ring in which n atoms are arranged is composed of n line segments of type A and $(N-3n)$ elemental line-segments of type B. The number of permissible arrangements of two types of line segments is expressed by

${}_{N-2n}\mathrm{C}_n$. Therefore, entropy of stage-2 structure under the restriction (b) is expressed by

$$\begin{aligned} S_{\mathrm{O},2}^{(\mathrm{b})} &= k_{\mathrm{B}} \ln \left\{ {}_{(1-4\delta)(2N_{\mathrm{A}})^{\frac{1}{3}}}\mathrm{C}_{2\delta(2N_{\mathrm{A}})^{\frac{1}{3}}} \right\}^{(2N_{\mathrm{A}})^{\frac{2}{3}}/4} \\ &\approx -\frac{1-4\delta}{2} R \left\{ \left(\frac{2\delta}{1-4\delta} \right) \ln \left(\frac{2\delta}{1-4\delta} \right) + \left(\frac{1-6\delta}{1-4\delta} \right) \ln \left(\frac{1-6\delta}{1-4\delta} \right) \right\}. \end{aligned} \tag{4.6}$$

The evaluated $S_{\mathrm{O},2}^{(\mathrm{b})}$ for $\delta = 0.098$ is 1.59 $\mathrm{JK^{-1}mol^{-1}}$, and the transition entropy is calculated, by subtracting this value from $S_{\mathrm{O},1}$, to be 1.66 $\mathrm{JK^{-1}mol^{-1}}$, which is rather close to the experimental value, 1.77 $\mathrm{JK^{-1}mol^{-1}}$. Second potential reason why the transition entropy evaluated by subtracting $S_{\mathrm{O},2}$ from $S_{\mathrm{O},1}$ is smaller than experimental value is that there exists another long-range order in the arrangement of excess oxygen atoms in the ε phase besides that corresponding to the superlattice peaks $(0,1,\frac{1}{2})$ observed by Tranquada *et al.*[29] The base of this consideration is that successive phase transitions were observed in the present study, while only one transition was observed in the neutron diffraction study by Tranquada *et al.* The successive α-to-ε' and ε'-to-ε phase transitions may be two-step ordering of excess oxygen atoms. That is, the ε' phase has the stage-2 structure as suggested by Tranquada *et al.*, and some equivalent accessible sites to excess oxygen atoms in the ε' phase of stage-2 structure would be divided into non-equivalent ones in the ε phase. It can not be concluded at present which of the two reasons stated above is reasonable.

By the way, it was found that the transition entropy of α through ε' to ε phases takes a maximum value around $\delta = 0.10$ as shown in Fig. 3.12. The transition entropy always increases as increasing δ around $\delta \approx 0.10$, when the entropy of ε phase is evaluated by using the expressions of $S_{\mathrm{O},2}$, $S_{\mathrm{O},2}^{(\mathrm{a})}$, or $S_{\mathrm{O},2}^{(\mathrm{b})}$. Such entropies of ε phase were evaluated under the assumption that the excess oxygen atoms are arranged among only the above-stated accessible sites in the both ranges of $\delta \leq \delta_\varepsilon$ and $\delta > \delta_\varepsilon$, where δ_ε is the stoichiometric content of ε phase. However, the fact that the transition entropy decreases with increasing δ above $\delta = 0.098$ indicates that the assumption is not adequate at least in the range $\delta > \delta_\varepsilon$. Thus, it is reasonable to assume that in the range $\delta > \delta_\varepsilon$, $\delta_\varepsilon N_{\mathrm{A}}$ excess oxygen atoms are arranged among the sites which are accessible in the range $\delta \leq \delta_\varepsilon$, and, on

the other hand, $(\delta - \delta_\varepsilon)N_A$ excess oxygen atoms remaining are arranged among the sites which are not accessible in the range $\delta \leq \delta_\varepsilon$. The entropy of ε phase in the range $\delta > \delta_\varepsilon$ is thus expressed by

$$S_{O,2} = k_B \ln\{{}_{N_A/2}C_{\delta_\varepsilon N_A}\} + k_B \ln\{{}_{3N_A/2}C_{(\delta-\delta_\varepsilon)N_A}\} \tag{4.7}$$

under the condition that the ε phase has simple stage-2 structure without short-range nor another long-range order discussed above as two potential orders present in the phase. The compositional dependence of the transition entropies evaluated by subtracting the values from $S_{O,1}$ is shown in Fig. 4.5. It is found that the entropies decrease as increasing the δ in the range $\delta > \delta_\varepsilon$($\delta_\varepsilon$ is assumed to be 0.10 in the figure), which is qualitatively consistent with the experimental results. This indicates that, when the occupation fraction in the line of accessible sites exceeds ~0.2, the Gibbs energy of the system is rather stabilized by locating the extra excess oxygen atoms on the sites unaccessible ordinarily in the ε phase than on the accessible sites more densely.

4.1.3.4 ζ phase

Tranquada *et al.*[30] have observed two kinds of superlattice peaks $(0,\frac{1}{3},1)$ and $(\frac{4}{5},0,\frac{4}{5})$ corresponding to $5a \times 3b \times 5c$ unit cell with respect to $F4/mmm$ notation below room temperature in $\delta = 0.125$ and 0.136 crystals. (Note that the definition of a and b axes is taken opposite to that by Tranquada *et al.* in order to coincide presently with stage-2 and stage-3 phases. The adoption of different axes causes no problem because which of a and b axes is longer was not determined without detection of orthorhombic splitting by them.) They reported that the peak intensities can not be explained by the rotation of NiO_6 octahedra as rigid, differently from the cases of stage-2 and stage-3 structures, and thus the NiO_6 octahedra should be deformed. The deformation pattern of NiO_6 octahedra was determined by analyzing the intensities of superlattice peaks on the assumption that the scattering comes only from La_2NiO_4 lattice with lanthanum, apical oxygen and planar oxygen atoms with displacement from the respective positions in the high-temperature $F4/mmm$ phase and nickel atoms without displacement. Then, they

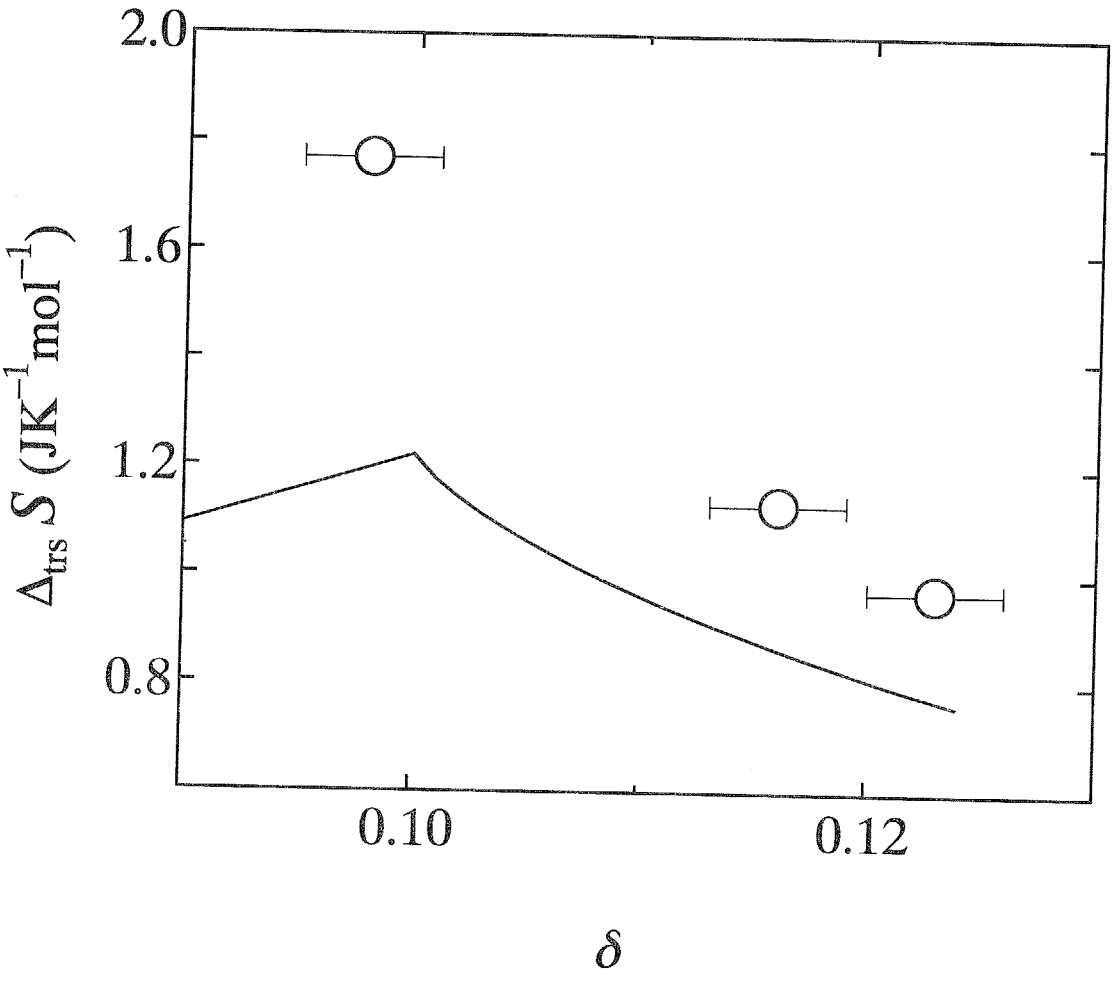

Figure 4.5: The whole entropy of ε-to-ε' and ε'-to-α phase transitions as a function of excess oxygen atom composition. Circles with error bar in the composition δ represent the experimental data. Solid line represents the dependence evaluated by subtracting the quantities derived according to eq. (4.7) from those according to eq. (4.1).

determined the locations of excess oxygen atoms among the interstitial sites having largest space. The projections onto the *bc* and *ac* planes of the three-dimensional arrangement of excess oxygen atoms are shown in Figs. 4.6(a) and 4.6(b) corresponding to $(0,\frac{1}{3},1)$ and $(\frac{4}{5},0,\frac{4}{5})$ superlattice peaks, respectively. According to their model, the composition of excess oxygen atoms is $\delta = 2/15(\approx 0.133)$ and the phase transition is of (completely-disordered)-to-(completely-ordered) phases with respect to the excess oxygen atoms; The transition entropy should be expressed by eq. (4.1). The entropy, as tabulated in Table 4.1, is much larger than and can not explain the experimental value as stated in section 4.1.3.1. Tranquada *et al.* have, in fact, observed weak diffuse scattering at 10 K and mentioned that a small fraction of the excess oxygen atoms do not participate in the three-dimensional ordering. The disorder, however, must not be due to incompleteness of the long-range order of arrangement suggested by Tranquada *et al.*, because, if that is in the case, the heat capacity jump due to the glass transition should be rather large. Therefore, the model suggested by Tranquada *et al.* is not quite compatible with the present calorimetric result, and the disorder rather similar to those discussed in the γ, ε' and ε phases should remain also in the ζ phase according to the calorimetric results. The picture of excess oxygen atom arrangement in the ζ phase, which explains the results by neutron diffractometry and calorimetry consistently, has not been established and is open to a question.

4.1.4 Three-dimensional antiferromagnetic phase transition and two-dimensional antiferromagnetic short-range-order in $La_2NiO_{4.00}$ crystal

The two-dimensional antiferromagnetic properties have been studied in detail in K_2NiF_4 crystals by neutron diffraction technique[42, 41] as stated in section 1.2.1. Heat capacities of K_2NiF_4 crystal were measured by Salamon and Ikeda [78] and the curve showed a small peak at the transition temperature, 97 K, and a broad hump rather on the high temperature side, as is consistent with the results of the neutron diffraction experiments.[42, 41] Circles and squares in Fig. 3.4 represent the heat capacities due to magnetic ordering in

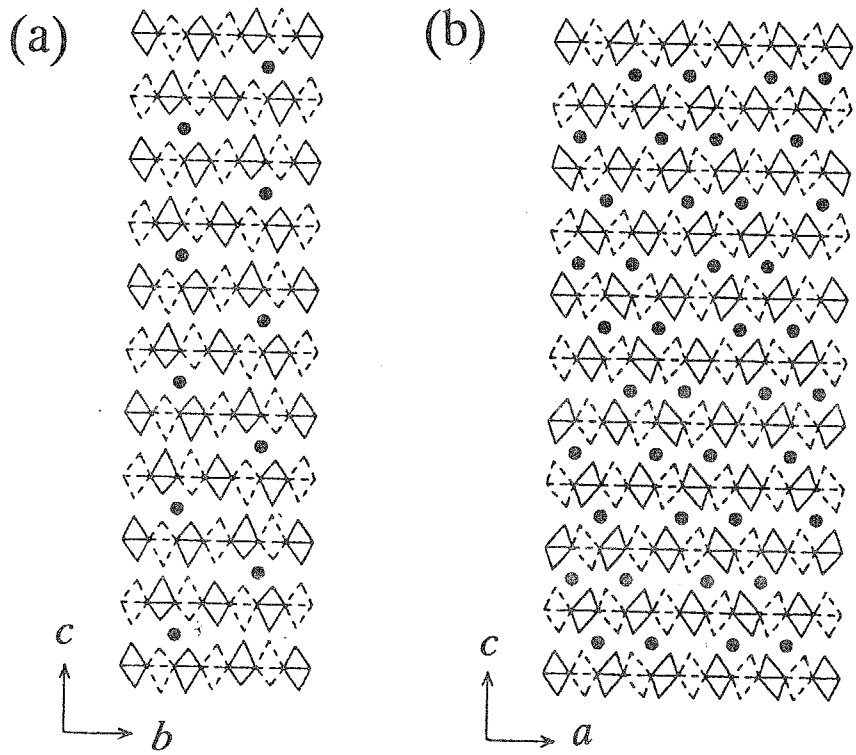

Figure 4.6: Unit cell, suggested by Tranquada *et al.*,[30] of the arrangement of excess oxygen atoms and the deformation pattern of NiO_6 octahedra in the low-temperature phase with $\delta = 2/15$, as projected onto (a) bc plane and (b) ac plane corresponding to $(0,\frac{1}{3},1)$ and $(\frac{4}{5},0,\frac{4}{5})$ superlattice peaks, respectively: Solid circles, excess oxygen atoms; diamonds, NiO_6 octahedra.

La_2NiO_4 and K_2NiF_4 crystals, respectively, for the normalization of the three-dimensional antiferromagnetic transition temperature, T_N. Both results show a small peak at T_N and a hump on the high temperature side of the peak. The two results are thus quite similar to each other, indicating that the magnetic properties of La_2NiO_4 crystal is of a K_2NiF_4 type. It is concluded that two-dimensional short-range order remains up to rather high temperatures above 500 K. The total entropy estimated from the heat capacities in Fig. 3.4 below 500 K is about 10 $JK^{-1}mol^{-1}$. Even if the heat capacity tail on the high temperature side is taken into the evaluation, the entropy would not exceed 15 $JK^{-1}mol^{-1}$. Considering the presence of some ambiguity that the baseline of heat capacities was derived from the phonon density of states by neutron scattering experiment,[61] it is concluded that the value is rather close to $R \ln 3$ expected from the spin of nickel ion.

4.1.5 Interrelation among orderings of holes, spins, and excess oxygen atoms

The temperature of three-dimensional antiferromagnetic phase transition decreased as the excess oxygen composition increased; 335 K, 60 K and 40 K for stoichiometric $\delta = 0$, γ and ε phases, respectively. This is understandable on the consideration that the holes doped into NiO_2 planes disturb the development of the short-range and correspondingly long-range order of spins within NiO_2 planes. This understanding is consistent with the results that a hump in the excess heat capacity curve found around 430 K in the stoichiometric crystal as shown in Fig. 3.3 was observed at lower temperature around 200 K in the nonstoichiometric crystals as shown in Fig. 3.9. However, the transition temperature abruptly increased, with further increase in the excess oxygen composition, up to 100 K in the ζ phase. This is remarkable according to the above understanding. The reason for the abrupt increase is discussed here in relation to orderings of holes and excess oxygen atoms.

As stated in section 1.2.3, Tranquada *et al.*[52] have observed stripe ordering of holes around 220 K and cooperative antiferromagnetic ordering at 110 K in $\delta = 0.125$ and 0.136 crystals. They suggested that the holes are located at the oxygen sites of NiO_2 planes

above 110 K, and arranged every three sites along the b-axis but still at random along the a-axis as shown in Fig. 1.6. The stripe ordering of holes creates the regions, where there is no hole, extending in the a- and c-directions. In each of the regions, the short-range order of spins within NiO_2 plane can develop along the a-axis and inter-plane interaction along the c-axis is not disturbed owing to the presence of holes, and thus three-dimensional antiferromagnetic phase transition would occur at relatively high temperature.

According to the results of Tranquada *et al.*, the superlattice peaks corresponding to the stripe order of holes were observed below 220 K and the magnitude increased exponentially as the temperature decreased. In addition to this, considering that no heat capacity anomaly was observed around 220 K in $\delta = 0.131$ and 0.135 crystals in the present study, it is concluded that the charge ordering does not proceed through its own phase transition. Judging from the fact that the magnitude of superlattice peaks corresponding to the stripe order become too small to be observed above the temperature, 220 K, where the heat capacity curves of $\delta = 0.131$ and 0.135 crystals rise up due to disordering of excess oxygen atoms, it follows that the hole ordering is strongly correlated with the ordering of excess oxygen atoms. It is thus expected that the holes are trapped at the neighbors of excess oxygen atoms at low temperatures, and that the stripe order of holes should reflect the arrangement of excess oxygen atoms in the ζ phase. The fact that the antiferromagnetic phase transition did not occur in the supercooled α phase of $\delta = 0.131$, 0.135, and 0.141 crystals as shown in Fig. 3.10 is understandable from that the stripe order of holes could not be achieved because the holes were trapped coupling with the excess oxygen atoms arranged randomly.

In view of the reasonable expectation that the arrangement of excess oxygen atoms along the a-axis and the positional correlation between hole and excess oxygen atom would be essentially same among γ, ε and ζ phases, one may consider that also in the γ and ε phases the stripe ordering should occur and the temperature of three-dimensional antiferromagnetic phase transition should be correspondingly high. However, the transition temperatures are lower in the γ and ε phases. This may be undestood on the consideration that the period of accessible sites to the holes in the b-direction is small and there is

no wide region, where there is no hole, extending in the c-direction in the γ and ε phases in comparison with the ζ phase as shown in Figs. 4.2, 4.4 and 4.6, respectively.

The heat capacity anomaly due to the antiferromagnetic phase transition collapsed in $\delta = 0.141$ crystal compared with those in $\delta = 0.131$ and 0.135 crystals. This is understood as due to the disturbance by the presence of extra excess oxygen atoms arranged among the unaccessible, ordinarily in the ζ phase, sites and thus holes arranged between the stripes. This result also supports the view that $\delta = 2/15$ is the stoichiometric composition for the ζ phase.

4.2 $La_2CuO_{4+\delta}$ system

4.2.1 Phase relation

4.2.1.1 Phase separation in the range $0.01 < \delta < 0.04$

Phase separation phenomena have been reported by many research groups in the composition range including $\delta = 0.011$ and 0.035. Considering that the phase transition temperatures, 265 K and 222 K, are same between $La_2CuO_{4.011}$ and $La_2CuO_{4.035}$ crystals, the compositions of two crystals are expected to be located within the same phase separation region at the relevant temperatures. On the other hand, the transition temperatures of the second-order phase transitions, 287 K and 295 K, are different between the two crystals. One would consider two possible reasonings for that: One is that the phase separation with respect to the excess oxygen composition occurs between 265 K and 287 K in $La_2CuO_{4.011}$ or between 265 K and 295 K in $La_2CuO_{4.035}$ crystal. When the phase separation newly occurs, a large heat evolution effect should be observed as in the case of $La_2NiO_{4+\delta}$ crystal. However, such a relaxation phenomenon was not observed at all below 300 K both in $La_2CuO_{4.011}$ and $La_2CuO_{4.035}$ crystals. Therefore, this reasoning must be wrong. The other reasoning is that the phase separation phenomena with respect to excess oxygen composition take place above 300 K in both crystals. Then, the difference in the temperatures of the second-order phase transition can be understood as follows. If the grain size of the phase in which the second-order phase transition occurs

is small, the cooperative effect causing the phase transition becomes weaker, and thus the transition temperature is lowered. Figure 4.7 shows the compositional dependence of the temperature of second-order phase transition determined from the electric resistivity measurements carried out by Itoh *et al.*[66] The transition temperature rises up to $\delta \approx 0.015$, but remains constant above 0.015. This phenomenon is consistent with the above understanding that the second-order phase transition occurs in the oxygen rich phase: The grain size is large enough above $\delta = 0.015$ to undergo the transition at the same temperature as that of bulk sample.

On the other hand, many research groups have reported that the phase separation phenomenon takes place at around 320 K,[6] 290 K,[36, 32] 280 K,[40] and 265 K.[37, 38, 39] The above interpretation seems to be inconsistent with these reports. It should be noted that the conclusion of "phase separation phenomenon" taking place was based on the results of neutron diffraction or electron microscopic techniques. The techniques are hard to monitor rearrangement processes of excess oxygen atoms. The situation happening would be understood as follows: The homogeneous single-phase crystal concerning both the excess oxygen composition and the crystal structure first separates to two phases only concerning the composition at a certain high temperature above 300 K, but the two phases separated have the same crystal structure, probably *Bmab* structure. The phase separation concerning excess oxygen composition can not be detected there by diffraction or microscopic techniques. As the temperature decreases, one of the two phases separated undergoes a structural transformation to another phase at around room temperature. Then the diffraction or microscopic techniques can detect the structural phase transition. The previous research groups must have accordingly misunderstood the structural transition to be a "phase separation phenomenon". Actually, all the reports concerning the phase separation can be understood from the viewpoint that three structural phase transitions occur in the oxygen-rich phase as stated in the following.

The evidences from which phase separation was concluded to occur are the results of neutron diffraction studies of $La_2CuO_{4+\delta}(\delta \approx 0.03)$ crystals carried out by Jorgensen *et al.*[6] and by Zolliker *et al*;[36] new reflection peaks were observed below 320 K or 290

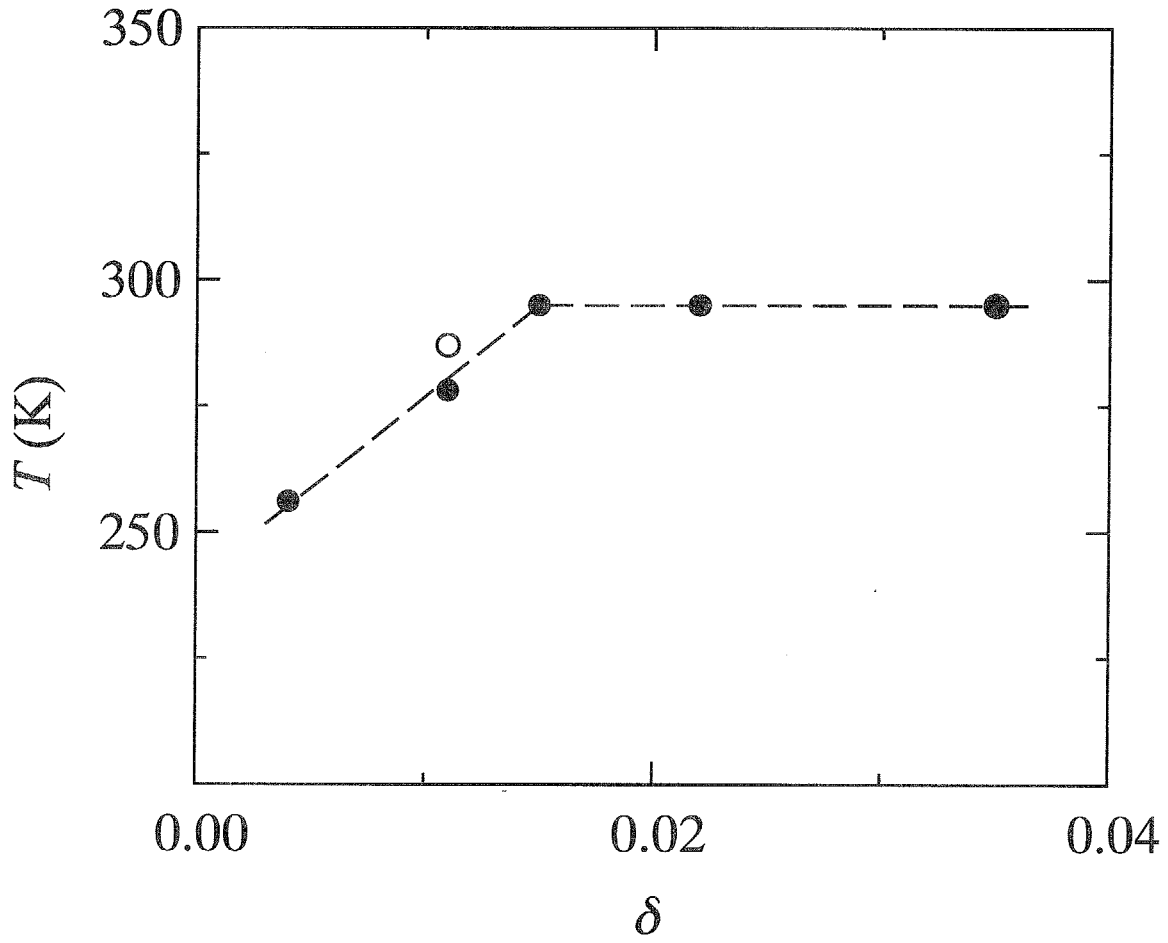

Figure 4.7: Composition dependence of the temperature of the second-order structural phase transition within a phase separation region: ●, Itoh *et al.*; ○, present results.[66]

K, respectively, together with the peaks observed above the temperatures. Figures 4.8 and 4.9 shows the temperature dependence of lattice constants taken from the results of Jorgensen *et al.* and Zolliker *et al.*, respectively. The two results are nearly same except for the phase separation temperature; *I*4/*mmm*-to-*Bmab* phase transition takes place at around 430 K, and phase separation into *Bmab* and *Fmmm* phases occurs at around 320 K or 290 K. The temperature, 290 K, is close to the temperature of the second-order structural phase transition at 295 K observed in the present study. On the other hand, the temperature, 320 K, reported by Jorgensen *et al.* is much higher than the temperature of second-order transition. It may be due to difficulty in the two-phase analysis. Wells *et al.*[33] also reported by neutron diffraction measurements that the phase separation occurs around 290 K in $\delta \approx 0.03$ crystal which is close to the results of present calorimetric study and neutron study by Zolliker *et al.*

Ryder *et al.*[40] also indicated the phase separation by using a microscopic technique. They worked on $La_2CuO_{4+\delta}$ polycrystal at room temperature, 200 K, and 100 K, and observed two separated phases at 200 K and 100 K, suggesting that the phase separation proceeded between room temperature and 200 K. (The sample was prepared by annealing under 1800 atm of oxygen atmosphere at 823 K for 24 h, and the excess oxygen composition would be $\delta \approx 0.03$.) The separation temperature was determined to be 280 K based on their results that the resistivity and Seebeck coefficient were reproducible and independent of cooling/heating rate above 280 K. However, this hysteresis phenomena can be explained as due to the first-order nature of the phase transitions at 265 K and at 222 K.

A few anomalies have been reported so far around 265 K in relation to phase separation but without any direct evidence. Vaknin *et al.*[37] observed, by using a neutron diffraction technique, an abrupt broadening of the (006) peak, and indicated the phenomenon to be due to a phase separation. (They did not observe the similar results to those by Jorgensen *et al.* and Zolliker *et al.* because of their lower resolution.) This phenomenon can be understood by taking the presence of the Martensitic phase transition at 265 K into consideration; a Martensitic phase transition usually produces microcrystalline particles due to the presence of the interfacial energies between the mother and daughter

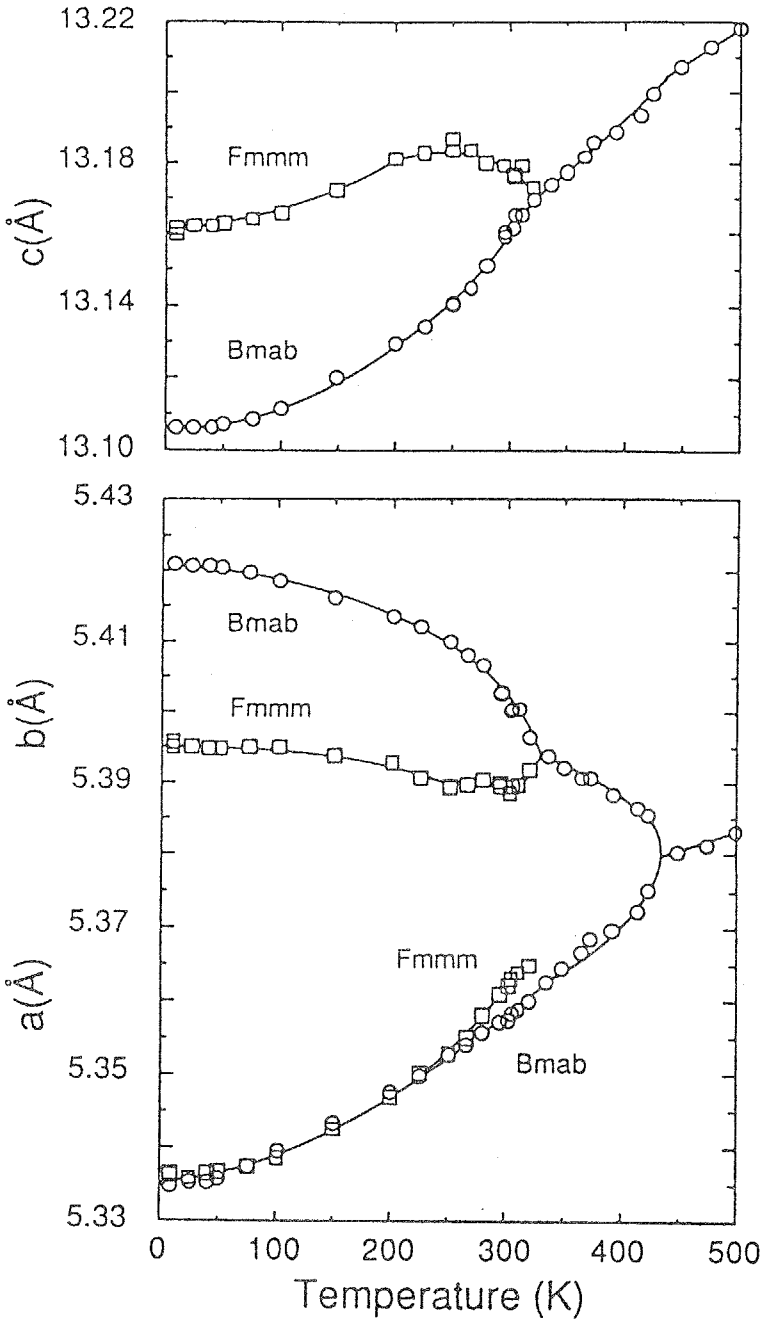

Figure 4.8: Temperature dependences of lattice constants of $La_2CuO_{4.03}$ crystal in the $I4/mmm$, $Fmmm$, and $Bmab$ phases reported by Jorgensen *et al.*[6]

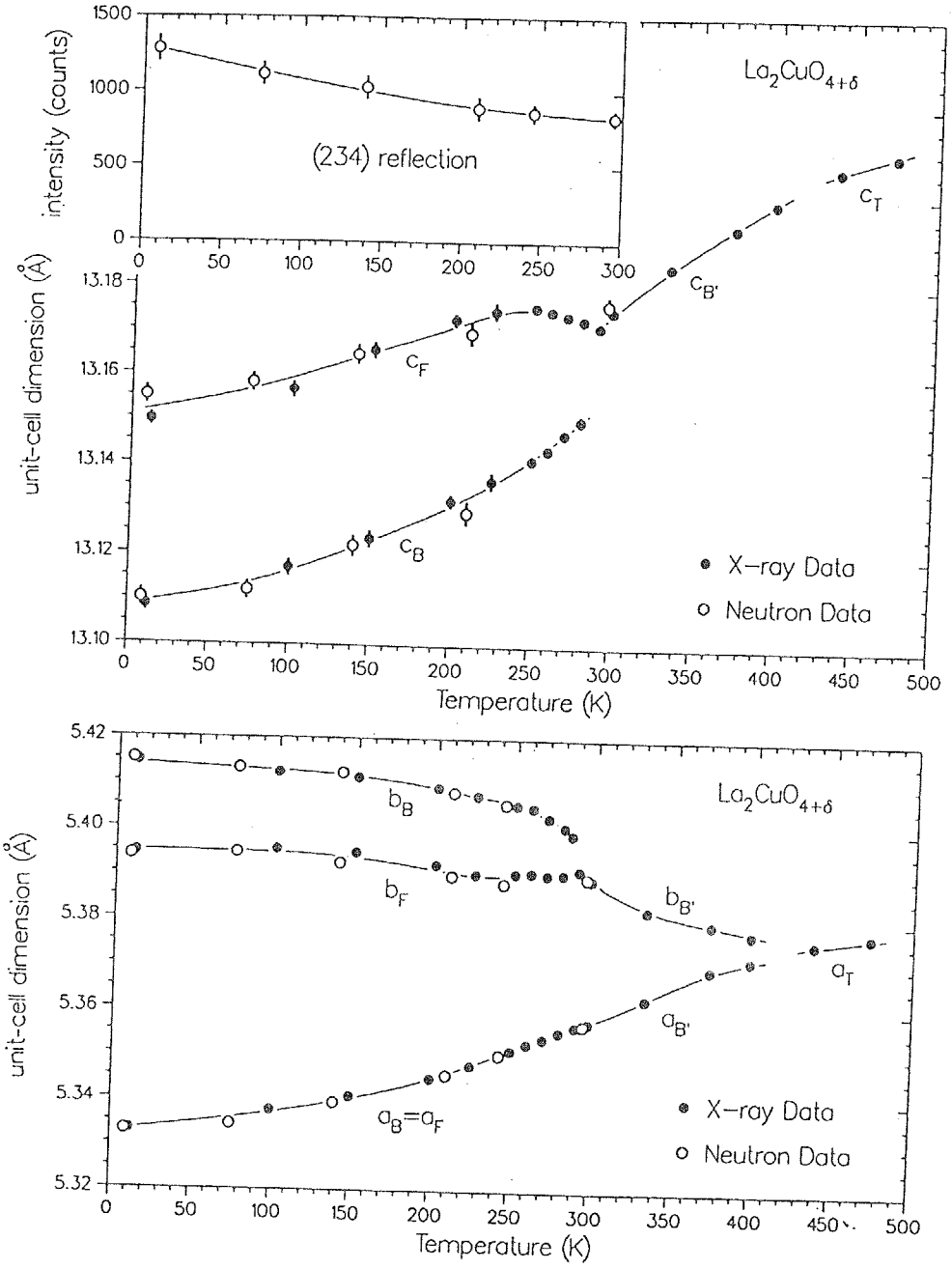

Figure 4.9: Temperature dependences of lattice constants of $La_2CuO_{4.03}$ crystal in the $I4/mmm$, $Fmmm$, and $Bmab$ phases reported by Zolliker *et al.*[36]

phases in the course of transition. Further, Hundley *et al.*[38] observed hysteresis phenomena around 265 K in resistivity, magnetic susceptibility, and thermoelectric power, and indicated those as due to the phase separation. These results are also understood to be due to the character of Martensitic phase transition.

The $La_2CuO_{4+\delta}$ crystals with $\delta \leq 0.035$ prepared by high pressure oxygen treatment show three displacive phase transitions.[66, 79, 80] The relation between these phase transitions and those at around 280 K and 160 K observed in $La_2CuO_{4.05}$ and $La_2CuO_{4.07}$ crystals, is not clear at present. However, the temperatures of transitions in $La_2CuO_{4.05}$ and $La_2CuO_{4.07}$ crystals are clearly different from those in $La_2CuO_{4+\delta}$ crystals with $0.015 \leq \delta \leq 0.035$. It is concluded that $\delta = 0.05$ and 0.07 are beyond a region of the phase separation relevant to $\delta \leq 0.035$ crystals and that the phase separation line is around $\delta \approx 0.04$.

4.2.1.2 Origin of stabilization phenomena observed in $\delta = 0.05$ and 0.07 crystals

Two possibilities are considered as the origin of the stabilization observed above 330 K in $\delta = 0.05$ and 0.07 crystals prepared by electrochemical oxidation: One is homogenization of excess oxygen content in the crystal in which excess oxygen atoms were incorporated heterogeneously by electrochemical oxidation at room temperature, and the other is a phase transition from a quasi-stable (potentially meta-stable) phase to a stable phase. If this is in the former case, in view of the fact that the heat evolution due to freezing-out of rearrangement motion of excess oxygen atoms was observed at above 140 K, the heat evolution phenomenon due to the stabilization should be observed at low temperatures much below 330 K. Considering that the heat evolution phenomenon started to be observed only at above 330 K, it is concluded that the stabilization is not only attributed to rearrangement of excess oxygen atoms but to a phase transition in which a new-phase nucleation is prerequisite. The reason why the as-prepared sample was in the quasi-stable phase but not in the stable phase is considered to be because the samples before and after the electrochemical oxidation at room temperature have different stable phases and

because the phase transition between them did not proceed during the oxidation due to any difficulty in the new-phase nucleation and glowth processes. In view of the fact that no heat evolution was observed in $La_2CuO_{4+\delta}$ (δ = 0.011 and 0.035) crystals prepared by high pressure oxygen annealing above 400 K,[66, 79] the processes could proceed only above room temperature and the δ = 0.011 and 0.035 crystals would have undergone the transition at high temperatures. Judging from the large heat-evolution effect observed, enthalpy and entropy of the transition are supposed to be rather large. This indicates that the transition (stabilization) would involve an ordering process of excess oxygen atoms.

4.2.2 Character of antiferromagnetic ordering in $La_2CuO_{4.002}$ crystal

Heat capacity anomaly was observed at 330 K in $La_2NiO_{4.00}$ crystal based on the three-dimensional antiferromagnetic phase transition as shown in Fig. 3.1. It was understood to be the same transition as observed in K_2NiF_4 crystal as discussed in section 4.1.1. On the other hand, no appreciable heat capacity anomaly was observed in $La_2CuO_{4.002}$ crystal at 315 K which is clearly the temperature of three-dimensional antiferromagnetic phase transition as found from the magnetic susceptibility measurements as shown in Fig. 3.15. This will be understood as follows from the fact that the in-plane Cu-Cu exchange interaction constant, $J \approx 1300$ K, is much larger than the temperature, 315 K, of three-dimensional antiferromagnetic phase transition. The large in-plane interaction means that correlation length within CuO_2 plane is very large and two-dimensional antiferromagnetic short-range order within CuO_2 plane rather develops even just above the transition temperature. Thus, the entropy change at the transition should be unobservable because no appreciable change in the magnitude of spin order occurs at the transition.

4.2.3 Annealing effects at 210 K and 250 K on the structural phase transitions and superconductivity in $La_2CuO_{4.011}$ crystal

Let us number the respective phases for the crystal with $\delta \approx 0.04$ in the order of decreasing temperature for clarity;

V (222 K) IV (265 K) III (295 K) II ($\sim$ 400 K) I.

The structural phase transition around 400 K is the $I4/mmm$-to-$Bmab$ phase transition.

Annealing effects around 200 K were examined in $La_2CuO_{4.011}$ crystal as shown in Fig. 3.25. The annealing at 210 K enhances the IV-to-V phase transition as seen in Fig. 3.25 (b); therefore, the annealed samples (open and solid circles in Fig. 3.19) are in the phase V, and the other samples are in the phase IV. The most remarkable point of the results is that the phases IV and V give definitely different superconducting-phase transition temperatures, 33 K and 40 K, respectively. The first-order phase transition at 222 K takes place undoubtedly in the oxygen-rich $\delta \approx 0.04$ metallic phase in the crystal. It is noted that the superconducting-transition temperature would change with small structural modifications of atoms under essentially the same arrangement of excess oxygen atoms.

Another interesting feature in the $La_2CuO_{4.011}$ crystal is concerned with the annealing effect at 250 K after cooling from 320 K. Since the anomaly around 265 K is ascribed to the Martensitic phase transition, the transition is expected to proceed relatively fast but to produce microcrystalline particles due to the presence of the interfacial energies between the mother and daughter phases in the course of transition. Then at 250 K which is below the transition temperature region, the whole sample is necessarily in the low temperature phase IV. In fact, the enthalpy of Martensitic phase transition did not depend on the annealing period below 257 K as shown in Fig. 3.23 (a). The annealing at 250 K is thus considered only to have enhanced the grain growth of the crystals. The annealing effects observed on the superconducting-transition temperature T_c and on the Meissner fraction are consistent with the above understanding. The T_c was independent

of the annealing period: This is reasonable since the crystalline particles with the sizes above a certain magnitude give the same T_c. If the annealing at 250 K enhanced the diffusion of excess oxygen atoms and the establishment of equilibrium δ at the temperature, on the other hand, the T_c would change with the annealing. The Meissner fraction increased with the annealing period is increased: This is reasonable since the fraction depends on the grain size of the crystals. Namely, the annealing at 250 K is understood to help removal of the defects, dislocations, and/or grain boundaries produced through the Martensitic phase transition.

4.2.4 Potential reasoning for the difference between some features of phase transitions in $La_2NiO_{4+\delta}$ and $La_2CuO_{4+\delta}$ systems

The difference in transition-metal elements affects the ordering process of excess oxygen atoms. The cooperative positional ordering of excess oxygen atoms was observed in $La_2NiO_{4+\delta}$ system around room temperature above $\delta \approx 0.06$, but, on the other hand, in $La_2CuO_{4+\delta}$ system it was expected to take place above 400 K even in $\delta = 0.07$ crystal. The temperatures of the cooperative positional ordering are thus different by at least 100 K between $La_2CuO_{4+\delta}$ and $La_2NiO_{4+\delta}$ systems. Here, the factors determining the temperature of cooperative positional ordering is considered. The first factor is coulomb repulsion among excess oxygen atoms. The interaction would be screened by holes in MO_2 planes. The screening effect may be relatively strong in $La_2CuO_{4+\delta}$ crystal rather than $La_2NiO_{4+\delta}$ crystal, because the holes are itinerant in the former crystal but localized in the latter crystal. The second factor is interaction among excess oxygen atoms in operation through the lattice deformation due to the presence of excess oxygen atoms themselves. Considering that Cu-O(2)(apical oxygen) bond length is much longer than Ni-O(2) bond length, it is supposed that elastic properties of MO_6 octahedra and thus interaction among excess oxygen atoms in operation through deformation or tilt of MO_6 octahedra would be different from each other. The third factor is the effect of electronic energy based on holes. The long-range ordering of excess oxygen atoms would lower the

electronic energy in addition to lattice energy, particularly in $La_2CuO_{4+\delta}$ crystal with itinerant holes for the following reason. When excess oxygen atoms are arranged in the disordered way, the band structure of the nonstoichiometric crystal is same essentially as one of the stoichiometric crystal because the disordered arrangement does not change the crystal symmetry, and thus holes occupy the edge of the valence band. On the other hand, if the excess oxygen atoms are ordered in the long range, a new band structure is formed in accordance with the new crystal symmetry, and the holes would occupy the lower energy states than before the ordering. This consideration is similar to Hume-Rothery rule in alloy. According to the rule, the crystal structure of disordered alloy appeared just below the melting point is determined so as to lower the energy of free electrons. Similarly to alloy, the excess oxygen atoms may be ordered so as to lower the energy of itinerant holes in $La_2CuO_{4+\delta}$ system. On the other hand, the electronic energy of localized holes in $La_2NiO_{4+\delta}$ system does not appreciably depend on whether the arrangement of excess oxygen atoms are ordered or disordered, because the energy state of the localized holes is not essentially related to translational symmetry of crystal unless charge ordering occurs. Thus, the effect of lowering in energy of holes due to the ordering of excess oxygen atoms raises the ordering temperature in $La_2CuO_{4+\delta}$ system rather than $La_2NiO_{4+\delta}$ system.

In relation to this, the both systems seem to show different behavior in the coupling between lattice deformation and positional ordering of excess oxygen atoms: In $La_2NiO_{4+\delta}$ system, the coupling is rather strong, the lattice deformation and the long range ordering of excess oxygen atoms taking place simultaneously, namely cooperatively. In $La_2CuO_{4+\delta}$ system, on the other hand, the ordering takes place at high temperatures and structural phase transitions due to lattice deformation of CuO_2 planes occur below room temperature probably in some coupling with the change of electronic state in CuO_2 planes. This will reflect the aspect that NiO_6 octahedron is rather tight so that the displacement of apical oxygen atom would lead to the tilt of the octahedron constituting the NiO_2 lattice while the apical oxygen atom of CuO_6 octahedron is rather loosely bonded with the central metal copper ion so that the positional ordering of excess oxygen atoms would occur rather independently of phase transitions due to the lattice deformation of CuO_2 planes.

4.3 Freezing-in process of rearrangement motion of excess oxygen atoms

4.3.1 Proposition of relaxation time expression for the rearrangement process of excess oxygen atoms and effective diffusion distance

A relaxation time of the process (one-step jump process) that an excess oxygen atom surmounts a potential barrier is expressed by eq. (1.2) as demonstrated in section 1.3. Because the relaxation time is a mean time which it takes for an excess oxygen atoms to surmount one potential barrier, it should take n times of the relaxation time of the one-step jump process in the process (n-step process) that an excess oxygen atom surmounts n potential barriers successively. The relaxation time, τ_n, of the n-step jump process would be thus written as

$$\tau_n = n\ \tau_0 \exp(\Delta\varepsilon_a/RT). \tag{4.8}$$

Here the $\Delta\varepsilon_a$ is supposed to be more or less constant for all the jump processes within the crystal. If the temperature of the system composed of many excess oxygen atoms is changed, each atom would need to surmount plural potential barriers to reach the equilibrium state of the system corresponding to the changed temperature. In the case where the crystal is homogeneous with respect to excess oxygen composition, each atom needs to surmount only several potential barriers to reach the equilibrium state. On the other hand, in the case where phase separation occurs in the crystal with respect to excess oxygen composition and that the equilibrium composition of at least one of two phases separated depends on the temperature, each atom needs to surmount many potential barriers in the rearrangement process required through the temperature change because the atom must diffuse over so long distance that the excess oxygen compositions of two phases separated should change. Heat evolution or heat absorption due to the positional jump of excess oxygen atom occurs, of course, in the cases whether the atoms surmount one potential barrier or many potential barriers. Thus, the heat evolution or heat absorption can be detected at temperatures in which any relaxation time expressed

by eq. (4.8) with $1 \leq n \leq n_{\max}$ overlaps the experimental time scale of calorimetry, where $n_{\max}$ corresponds to a maximum number of the potential barriers which each excess oxygen atom needs to surmount in the rearrangement/ordering process. Of course, $n_{\max}$ is an ambiguous quantity.

If there is no gradient in the potential curve for excess oxygen atoms in a crystal, the atom jumps at random in any directions, and the effective diffusion distance, l, after n-step jumps is expressed on consideration of the random walk problem to be,

$$l = \sqrt{n}\, a, \tag{4.9}$$

where a corresponds to the jump distance of one-step.[69] Of course, there is a gradient in the potential curve in the phase-separated crystal such as $La_2NiO_{4+\delta}$. However, it would be valid to estimate the order of the effective diffusion distance by eq. (4.9). In the case where phase separation occurs in the crystal with respect to exces oxygen composition, the effective diffusion distance corresponding to $n_{\max}$ would correspond to the distance between oxygen rich and poor phases in the order of magnitude. According to the results of electron microscopy and neutron diffraction studies of $La_2CuO_{4+\delta}$ crystals carried out by Ryder *et al.*[40] and Jorgensen *et al.*[6], oxygen rich and poor phases are located alternately with a periodicity of ~300 Å and ~3000 Å, respectively. These values correspond to $\sim 10^4$ and $\sim 10^6$ in the values of $n_{\max}$, respectively, because a is about 3 Å. On the other hand, in the homogeneous crystal the effective diffusion distance would be about a several angstrom at longest, corresponding to 10 in the value of $n_{\max}$. The solid lines (a), (b) and (c) in Fig. 4.10 represent the temperature dependences expressed by eq. (4.8) with $n = 1$, 10, and 10^4, respectively. The experimental time scale of calorimetry is represented by the region between two dotted holizontal lines. The region represented by the arrows (d) and (e) show the glass transition temperature region in the cases of $n_{\max} = 10$ and $n_{\max} = 10^4$, respectively. It is clearly seen from the figure that the glass transition temperature regions are wide and relatively narrow in the cases with and without long-distance diffusion of excess oxygen atoms, respectively.

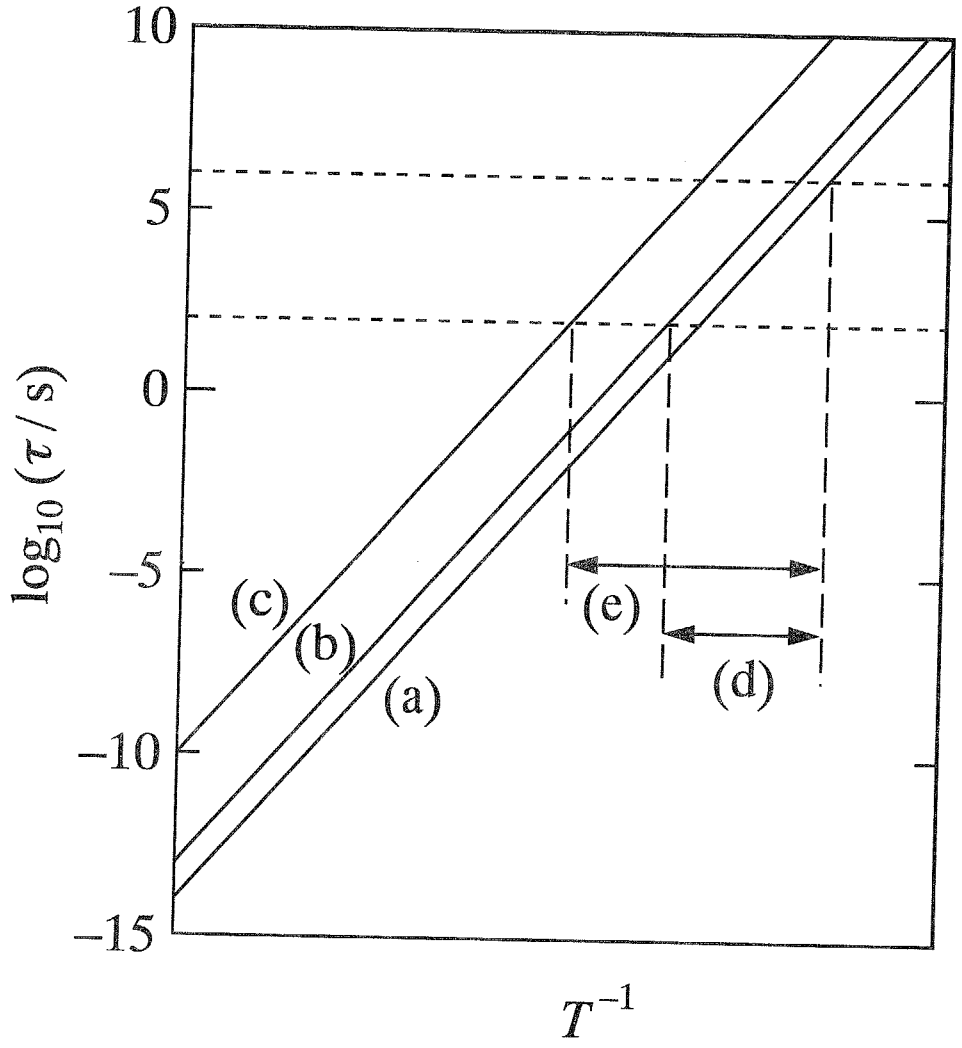

Figure 4.10: Arrhenius plots of relaxation times of eq. (4.8): line (a), one-step jump process; line (b), 10-step jump process; line (c), 10^4-step jump process. Two horizontal dashed lines represent the boundaries of the range of experimental time scale, 10^2-10^6 s, by a precise adiabatic calorimetry. Arrows (d) and (e) represent the glass transition temperature regions involving 1∼10-step processes and 1∼10^4-step processes, respectively. See text for detail.

4.3.2 Freezing-in processes in $La_2NiO_{4+\delta}$ crystals

4.3.2.1 Freezing-in of long-distant diffusion of excess oxygen atoms

Figure 4.11 shows Arrhenius plots of the relaxation times of $La_2NiO_{4.062}$ crystal, estimated from the temperature range where heat evolution or absorption effect was observed. The activation energy of the one-step jump process corresponding to $n = 1$ in eq. (4.8) is estimated from the relaxation data at low temperatures. In view of the fact that the exothermic drift starts to be observed at around 160 K, the relaxation time of the process is in the order of magnitude of 10^6 s there, as plotted by an open circle. The straight line (a) represents the temperature dependence of the relaxation times for the one-step process according to the Arrhenius eq. (4.8) assuming that $\tau_0 = 10^{-14}$ s. The activation energy, $\Delta\varepsilon_a$, of the one-step jump process is estimated from the slope of the line (a) to be 61 $kJmol^{-1}$.

In view of the fact that the endothermic drift could not be detected above around 250 K, the relaxation time of n_{max}-jump process is in the order of magnitude of 10^2 s there, as plotted by a open square. The straight line (b) represents the temperature dependence of the relaxation times for the n_{max}-jump process, which is drawn as the data of open square is located on. The suitable value of n_{max} is $\sim 10^{3.5}$. This indicates that each excess oxygen atom needs to surmount $\sim 10^{3.5}$ potential barriers in the order of magnitude until the crystal reaches new equilibrium state by each temperature jump. It follows from the above consideration of random-walk problem that the effective diffusion-distance of excess oxygen atoms in the equilibrium process is $\sim$150 Å more or less in one direction. The effective diffusion distance is not inconsistent with the value, $\sim$300 Å expected from the structural data of related crystal $La_2CuO_{4+\delta}$.[40]

$\delta = 0.067$ and 0.073 crystals also showed a glass transition phenomenon in the wide temperature range(from 150 K to $\sim$230 K) as shown in Fig. 3.6(a), which gives an evidence of the occurrence of phase separation with respect to excess oxygen composition in the range.

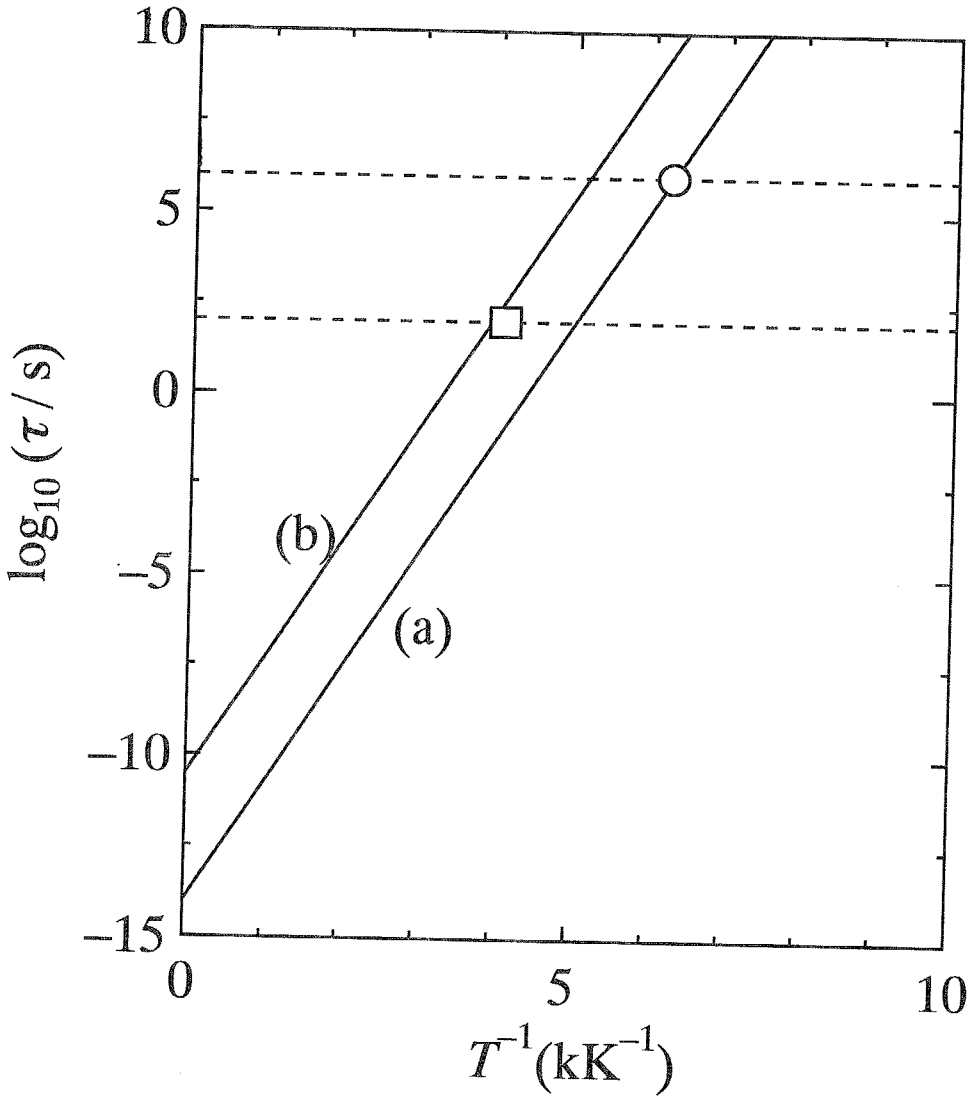

Figure 4.11: Arrhenius plots of relaxation times in $La_2NiO_{4.062}$ crystal: line (a), one-step jump process; line (b), $10^{3.5}$-step jump process. Open circle and square represent the data corresponding to the lowest and highest temperatures beyond which no heat evolution nor absorption was observed. Two horizontal dashed lines represent the boundaries of the range of experimental time scale, 10^2-10^6 s, by a precise adiabatic calorimetry.

4.3.2.2 Freezing-in of short-distant rearrangement of excess oxygen atoms in ε phase

The glass transitions were also observed in homogeneous ε phase in $\delta = 0.098$, 0.116 and 0.123 crystals as shown in Fig. 3.8. They should be due to the short-distant rearrangement of excess oxygen atoms. Two origins of the freezing-in process are considered as follows: One is the development of long-range order(in other words, the partial disorder remaining) of the arrangement of excess oxygen atoms along the b- and c-axes with respect to α-to-ε'-to-ε successive phase transitions, and the other is short-range ordering with respect to the arrangement of excess oxygen atoms along the a-axis in the ε phase. Which is responsible for the observed glass transition is not clear at present. Judging from the facts that glass transition was observed in $\delta = 0.131$ crystal but that no appreciable heat evolution nor absorption effect due to glass transition was observed in $\delta = 0.135$ and 0.141 crystals, the glass transition observed in $\delta = 0.131$ crystal would be owing to larger amount of the α phase remaining even at low temperatures as compared with $\delta = 0.135$ and 0.141 crystals.

4.3.3 Freezing-in of short-distant rearrangement of excess oxygen atoms observed in $La_2CuO_{4.05}$ crystal

It is found that the rearrangement motion of excess oxygen atoms is frozen-in at around 170 K in $La_2CuO_{4.05}$ crystal. The temperature, 140 K, at which the heat-evolution effect was started to be observed for the rapidly precooled sample is close to that, 160 K, for the $La_2NiO_{4.062}$ crystal. The temperature region of the glass transition, 140-190 K, is however narrower than 160-250 K in the case of $La_2NiO_{4.062}$ crystal as stated in the last section. The narrow temperature region of the glass transition indicates that it is not associated with a phase separation but with freezing-in of short-distant rearrangement motion of excess oxygen atoms in homogeneous phase. The same plot of relataxtion times for $La_2CuO_{4.05}$ crystal as is shown in Fig. 4.11 is given in Fig. 4.12. The $n_{max} \approx 10^{1.5}$ was obtained from the plot, which is consistent with the interpretation of the glass transition as due to the freezing-in of the short-range rearrangement.

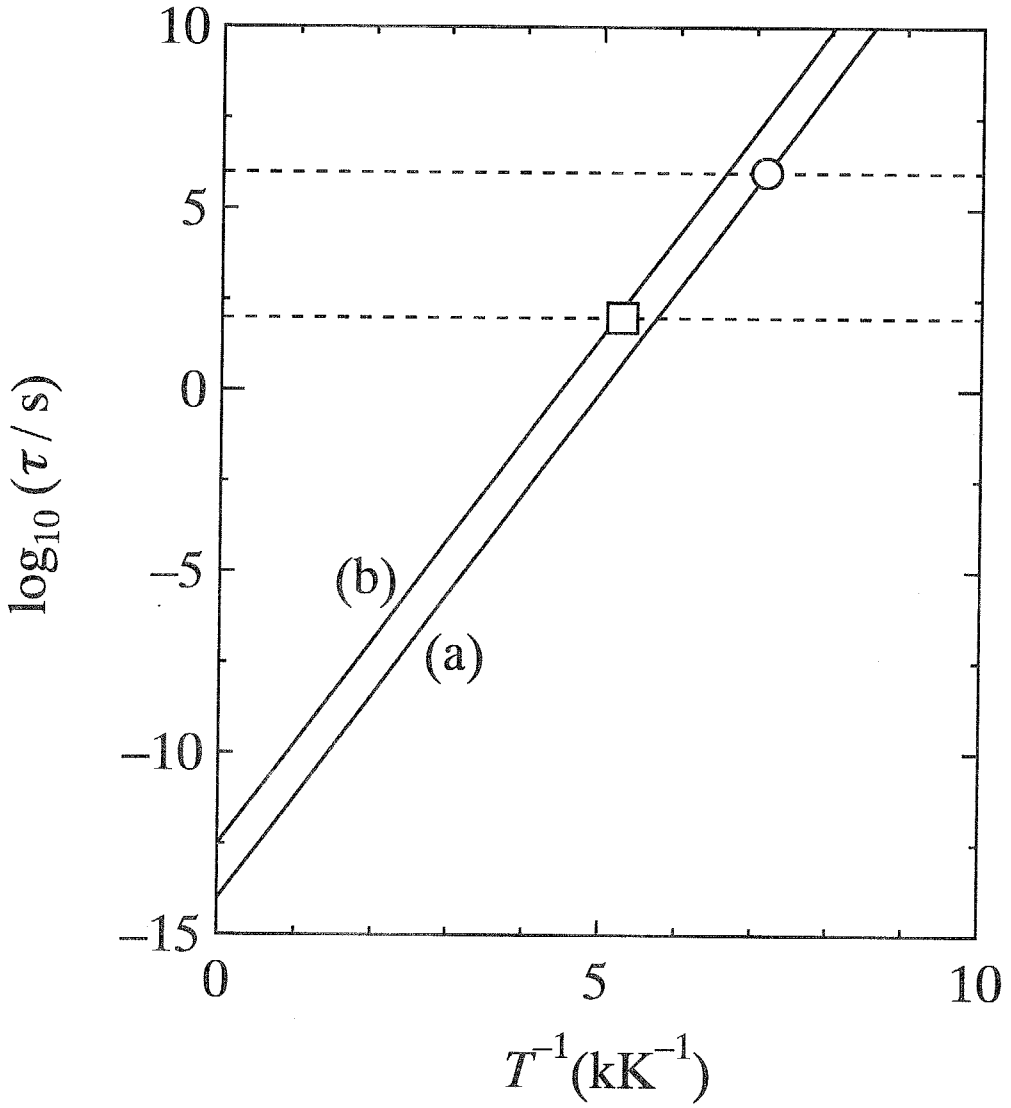

Figure 4.12: Arrhenius plots of relaxation times in $La_2CuO_{4.05}$ crystal: line (a), one-step process; line (b), $10^{1.5}$-step process. Open circle and square represent the data corresponding to the lowest and highest temperatures beyond which no heat evolution nor absorption was observed. Two horizontal dashed lines represent the boundaries of the range of experimental time scale, 10^2-10^6 s, by a precise adiabatic calorimetry.

4.3.4 Characters in the crystal structure determining the glass transition temperature

The heat evolution and absorption effects due to glass transition were observed in the temperature range 200-270 K in $La_3Ni_2O_{7.091}$ crystal. Because the temperature region is relatively wide, it might be concluded that the crystal is phase separated with respect to excess oxygen composition as well as $La_2NiO_{4.062}$ crystal. However, it is noticed that the presence of stacking faults of $LaNiO_3$ and LaO layers has been reported in $La_3Ni_2O_{7+\delta}$ and $La_4Ni_3O_{10}$ crystals.[81] Actually, the X-ray diffraction peaks of $La_3Ni_2O_{7.091}$ crystal were found to be broad as compared with those of $La_2NiO_{4+\delta}$ crystal, as consistent with the presence of stacking faults. Therefore, the wide glass transition temperature region would be based on the presence of the wide distribution of activation energies in the crystal owing to the presence of stacking faults.

When an excess oxygen atom changes its position, it must push away apical oxygen atoms, O(2), which surround the excess oxygen atom. It is thus expected that the easier the pushing away of apical oxygen atoms is, the lower the activation energy for the diffusion of excess oxygen atoms; that is, the longer the distance between transition metal atom, M, and the apical oxygen atom is, the more easily the apical oxygen atoms would be pushed away. Figure 4.13(a) shows the relation between M-O(2) distance, $d_{M-O(2)}$, and the temperature, $T_{g,s}$, at which appreciable heat evolution effect due to the glass transition started to be observed, for $La_2CuO_{4.05}$, $La_2NiO_{4.062}$ and $La_3Ni_2O_{7.091}$ crystals.(The M-O(2) distances plotted in the figure are the values in the respective stoichiometric crystals. See Table 1.1 for the values in La_2CuO_4 and La_2NiO_4 crystals and literature[1] for that in $La_3Ni_2O_7$ crystal.) It is found that $T_{g,s}$ and therefore the activation energy for the diffusion of excess oxygen atoms become small with increasing the M-O(2) distance, indicating that the expectation is quite reasonable.

Another correlation was found between the glass transition temperature and the volume, v_i, of the interstitial site, where the excess oxygen atom is accomodated, as shown in Fig. 4.13(b); the values are for the respective stoichiometric crystals. It is

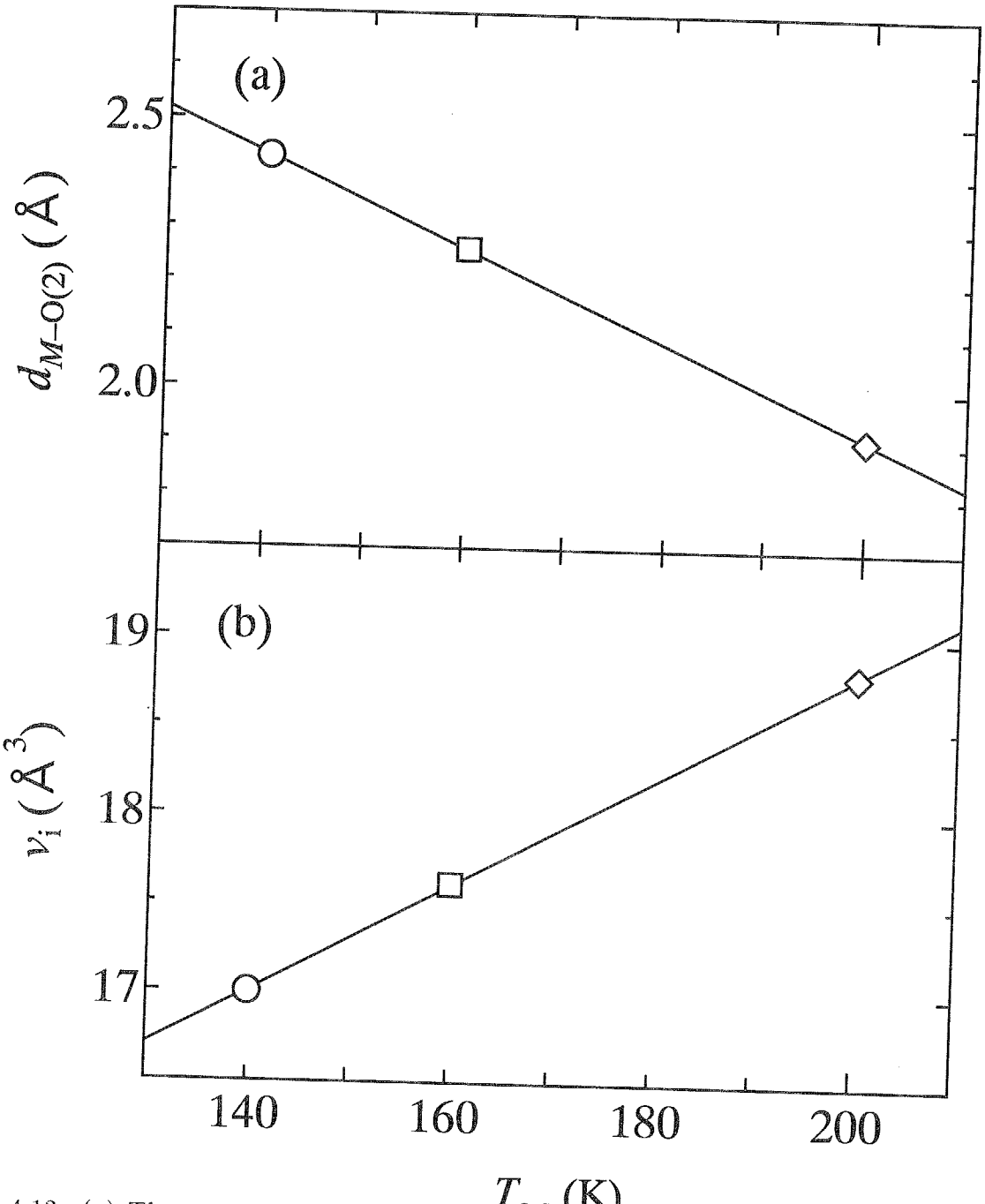

Figure 4.13: (a) The relation between M-O(2) distance, $d_{M-O(2)}$, and the temperature, $T_{g,s}$, at which appreciable heat evolution effect due to the glass transition started to be observed; (b) The relation between $T_{g,s}$ and the volume, v_i, of the interstitial site, where the excess oxygen atom is accomodated: ○, $La_2CuO_{4.05}$ □, $La_2NiO_{4.062}$ ◇, $La_3Ni_2O_{7.091}$.

deduced from the figure that the activation energy for the diffusion of excess oxygen atoms becomes large with increasing v_i. The correlation is interpreted as follows: The activation energy is the difference in energy between the two states where the excess oxygen atom is located at a stable interstitial site and at a saddle point between the neighboring interstitial sites, as represented by marks $\times$ and $+$ respectively in Fig. 4.14(a). The spatial circumstances of the oxygen atoms located at the stable site and the saddle point are dipicted in Figs. 4.14(b) and 4.14(c) respectively for $La_3Ni_2O_7$ crystal which has the largest v_i among the three systems as cross sections of planes drawn by thick solid and dashed lines in Fig. 3.14(a), respectively. Open circle drawn by thick line and shaded circle represent apical oxygen atom and lanthanum atom, respectively, and open circle drawn by thin line represents excess oxygen atom located at the respective sites. The ionic radii of O^{2-} and La^{3+} are 1.40 Å and 1.15 Å, respectively. As seen from the figures, both the distances between the stable site and the surrounding atoms and between the saddle point and the surrounding atoms are smaller than the sum of ionic radii of excess oxygen ion, O^{2-}, and the corresponding surrounding ion, O^{2-} or La^{3+}. The situation is same in the other two systems, La_2CuO_4 and La_2NiO_4 crystals. Thus, the energies of the both states become lower with increasing v_i. The dependence of the energies of the respective states on v_i should be, however, different from each other. When located at the stable site, the excess oxygen atom is surrounded by four apical oxygen atoms and four lanthanum atoms and the average distance between the excess oxygen atom and each of the surrounding atoms is $\sqrt{3}v_i^{\frac{1}{3}}$. On the other hand, when located at the saddle point, the excess oxygen atom is surrounded by two apical oxygen atoms and two lanthanum atoms and the average distance between the excess oxygen atom and each of the surrounding atoms is $\sqrt{2}v_i^{\frac{1}{3}}$. Therefore, as v_i increases, the distance between the stable site and the surrounding atoms increases in proportion to $\sqrt{3}$, but the distance between the saddle point and the surrounding atoms increases in proportion to $\sqrt{2}$. In addition, the coordination numbers are eight at stable site and four at saddle point. The both factors are expected, in a certain range of v_i, to lead to faster decrease in the energy at the stable interstitial site rather than at the saddle point. In such situations,

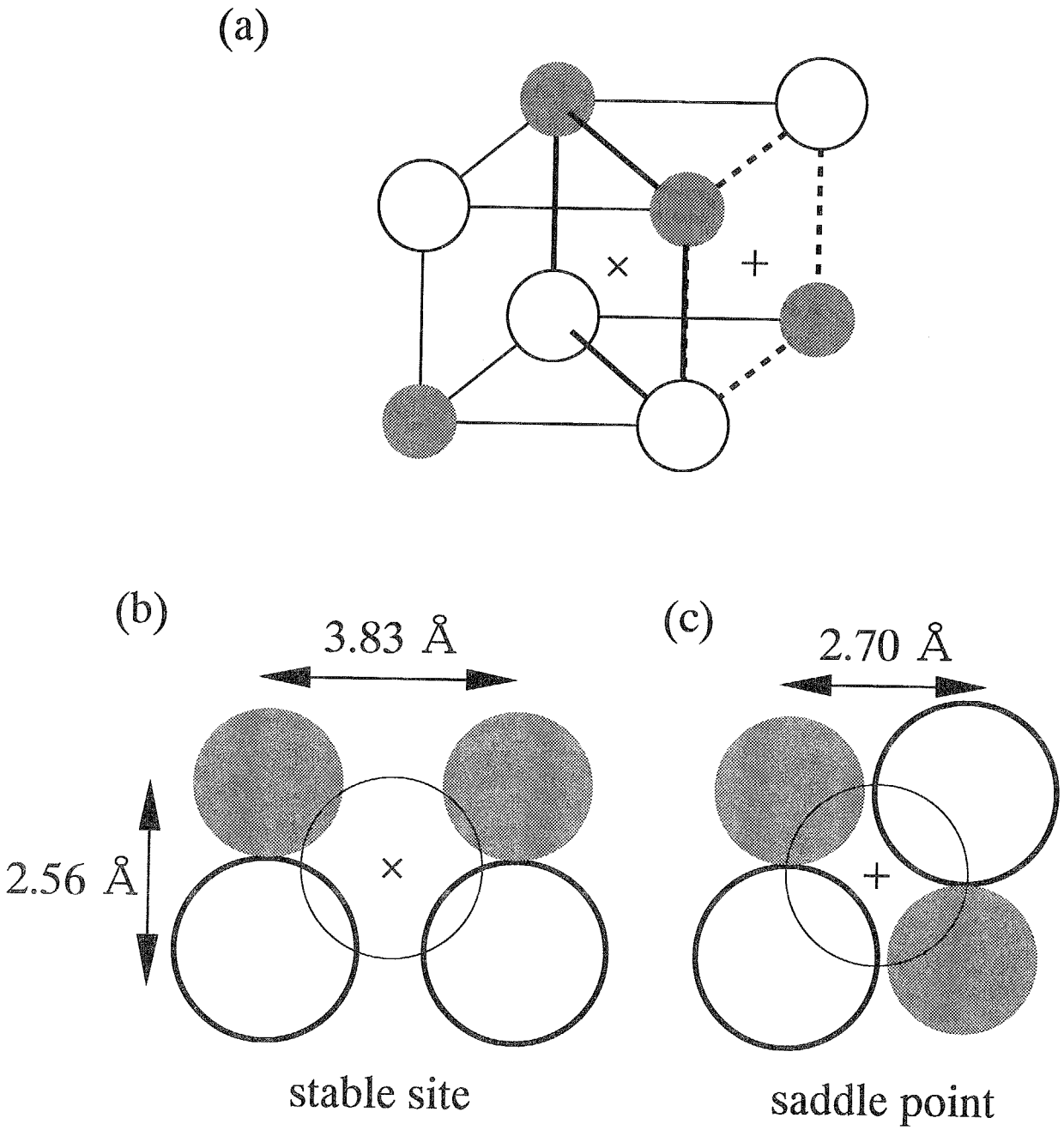

Figure 4.14: (a) Interstitial site with the stable site and saddle point for excess oxygen atom as represented by the marks × and +, respectively. Open and shaded circles represent apical oxygen atom and lanthanum atom, repsectively. The cross sections of planes drawn by thick solid and dashed lines in Fig. (a) when an excess oxygen atom, which represented by open circle drawn by thin line in Figs. (b) and (c), is located at (b) the stable site and (c) the saddle point, respectively. The values of distances indicated in the figure are for those in $La_3Ni_2O_7$ crystal. Open circle drawn by thick solid line and shaded circle represent apical oxygen atom and lanthanum atom, repsectively.

the activation energy, namely the difference in energy between the relevant two states becomes large with increasing v_i.

Chapter 5

Concluding remarks

Adiabatic calorimetry was demonstrated to be a very effective technique so as to clarify the thermodynamic(static) and kinetic properties of nonstoichiometric crystalline systems. This technique will be successfully applied to studies on other similar systems in future.

Many interesting features have been disclosed concerning the phase relation in the present systems. First, it is noticed that the eutectoid and peritectoid phase formation/decomposition and solid solution formation take place with respect to the composition of excess oxygen atoms in $La_2NiO_{4+\delta}$ systems. These will be generally found in many other nonstoichiometric crystalline systems. In relation to this, how the low-temperature structures are stabilized at discrete compositions of excess oxygen atoms in $La_2NiO_{4+\delta}$ system has not been clarified yet completely. The clarification gives an interesting subject in the future work. Second, $La_2NiO_{4+\delta}$ and $La_2CuO_{4+\delta}$ systems show different behaviors. The coupling between the positional ordering of excess oxygen atoms and the lattice deformation of NiO_2 planes in $La_2NiO_{4+\delta}$ system seems to be stronger than the corresponding coupling interaction in $La_2CuO_{4+\delta}$ system: In the former system, the ordering and the deformation take place simultaneously in one phase transition, while in the latter system the two proceed rather separately through different phase transitions. This was interpreted as due to the difference that the NiO_6 octahedron is rather tight in the bonding and the apical oxygen of CuO_6 octahedron is rather loosely bonded. Such a difference in the coordination bonds of MO_6 octahedea between copper and some other transition-metal ions has been reported in many fields of inorganic chemistry. The difference in the coupling

would be one consequent of the aspect appearing in the present systems. In relation to this, some potential reasonings were raised for the observation that the temperature of the long-range ordering of excess oxygen atoms is higher by over 100 K in $La_2CuO_{4+\delta}$ than that in $La_2NiO_{4+\delta}$ with same $\delta \approx 0.06$. The determination of which reasoning is adequate to the evaluation is desired in future. Third, interesting features are found in the magnetic properties. One is that strong coupling exists between the ordering of excess oxygen atom positions and the ordering of magnetic spins on NiO_2 planes in $La_2NiO_{4.13}$ crystal: The magnetic phase transition takes place only under the ordered arrangement of excess oxygen atoms. This is quite interesting in the respect that the holes introduced into the NiO_2 planes are coupled in their positions to the excess oxygen atoms in the crystal and therefore under the ordered arrangement of excess oxygen atoms the spins on nickel ions could form the two and partially three dimensional extension as a region without hole. This means that the holes in $La_2NiO_{4+\delta}$ crystal are localized, as is consistent with the fact that the crystal is semiconductor or insulator. Another feature is that the antiferromagnetic phase transition in La_2CuO_4 crystal disappears and instead superconducting phase transition appears with rather small amount of δ, and on the other hand the antiferromagnetic phase transition in La_2NiO_4 crystal remains through the δ range measured in the present study. In reality, the antiferromagnetic ordering in $La_2NiO_{4+\delta}$ has been observed in the low-temperature phase with ordered arrangement of excess oxygen atoms. These would be interpreted, as well, based on the aspect that the holes are apt to be rather fixed on some local sites in $La_2NiO_{4+\delta}$ while rather itinerant over CuO_2 planes in $La_2CuO_{4+\delta}$. Fourth, it is noted that there exists naturally a strong correlation between the manner of lattice deformation and the properties of superconducting phase transition in $La_2CuO_{4+\delta}$. The clarification is also a subject in the future, without detailed informations about the manner of lattice deformation at present.

The expression of the relaxation times proposed for the diffusion process of excess oxygen atoms is noticed. According to this expression, long-distant diffusion process such as phase separation and short-distant one such as the order-disorder process in homogeneous systems are discriminated, as an example, from the temperature range in which the

enthalpy relaxation phenomenon due to glass transition is observed calorimetrically: The former process displays the relaxation phenomenon in a rather wide range while the latter in a narrow range, and the average step number, in the order of magnitude, proceeding really in the diffusion can be estimated from the analysis of the range observed. The idea of the expression would be applicable even in making insight into the relaxation processes in supercooled liquids and glasses in the future.

This study is the first which has disclosed the dynamic properties of excess oxygen atoms in the present systems. Glass transition phenomena due to the freezing-in of the rearrangement motion of the oxygen atoms were observed in $La_2NiO_{4+\delta}$, $La_3Ni_2O_{7+\delta}$ and $La_2CuO_{4+\delta}$ crystals. Especially the phenomenon was observed over the wide temperature range 150-250 K in $La_2NiO_{4+\delta}$ system. This result provides the first evidence for the fact that the excess oxygen atoms freeze in below the glass transition temperature and that the phase separation takes place with respect to excess oxygen atom composition in $La_2NiO_{4+\delta}$ system.

Since the discovery of superconductivity in $(La, Ba)_2CuO_4$ crystal, many Cu-based superconductors have been synthesized so far. Most of the crystals show oxygen nonstoichiometry. It has been reported in $YBa_2Cu_3O_{6+\delta}$ crystal that the excess oxygen atoms are arranged in the disordered way in the small δ region and in the ordered way in the large δ region.[82] What long-range ordered structures are formed in the arrangement of the excess oxygen atoms is attractive in the comparison with those realized in $La_2NiO_{4+\delta}$ crystal. In view of the present results, the dynamic properties and ordering processes of excess oxygen atoms and phase relation of these crystals are also intriguing in relation to the nature of superconductivity.

Bibliography

[1] Z. Zhang, M. Greenblatt, and J. B. Goodenough, *J. Solid State Chem.* **108,** 402 (1994).

[2] Z. Zhang and M. Greenblatt, *J. Solid State Chem.* **117,** 236 (1995).

[3] Y. Nishihara, M. Tokumoto, K. Murata, and H. Unoki, *Jpn. J. Appl. Phys. Part 2* **26**, L1416 (1987).

[4] S. M. Fine, M. Greenblatt, S. Simizu, and S. A. Friedberg, *Phys. Rev.* **B36**, 5716 (1987).

[5] J. E. Schirber, B. Morosin, R. M. Merrill, P. F. Hlava, E. L. Venturini, J. F. Kwak, P. J. Nigrey, R. J. Baughman, and D. S. Ginley, *Physica* **C152**, 121 (1988).

[6] J. D. Jorgensen, B. Dabrowski, S. Pei, D. G. Hinks, and L. Soderholm, *Phys. Rev.* **B38**, 11337 (1988).

[7] J. Choisnet, J. M. Bassat, H. Pilliere, and P. Odier, *Solid State Commun.*, **66**, 1245 (1988).

[8] K. Kitayama, *J. Solid State Chem.* **87**, 165 (1990).

[9] P. Odier, J. M. Bassat, J. C. Rifflet, and J. P. Loup, *Solid State Commun.* **85**, 561 (1993).

[10] A. Wattiaux, J.-C. Park, J. C. Grenier, and M. Pouchard, *C. R. Acad. Sci.* (Paris) **310**, 1047 (1990).

[11] J. C. Grenier, A. Wattiaux, N. Lagueyte, J.-C. Park, E. Marguestaut, J. Etourneau, and M. Pouchard, *Physica* **C173**, 139 (1991).

[12] J. D. Jorgensen, B. Dabrowski, S. Pei, D. R. Richards, and D. G. Hinks, *Phys. Rev.* **B40**, 2187 (1989).

[13] P. Ganguly and S. Ramasesha, *Magn. Lett.* **1**, 131 (1980).

[14] R. R. Schartman and J. M. Honig, *Mat. Res. Bull.* **24**, 1375 (1989).

[15] H. Tamura, A. Hayashi, and Y. Ueda, *Physica* **C216**, 83 (1993).

[16] J. W. Rogers, Jr., N. D. Shinn, J. E. Schirber, E. L. Venturini, J. F. Kwak, P. J. Nigrey, R. J. Baughman, and D. S. Ginley, *Phys. Rev.* **B38**, 5021 (1988).

[17] N. D. Shinn, J. W. Rogers, J. E. Schirber, E. L. Venturini, B. Morosin, and D. S. Ginley, *Synthetic Metals* **29**, F709 (1989).

[18] J. Zhou, S. Shinha, and J. B. Goodenough, *Phys. Rev.* **B39**, 12331 (1989).

[19] M. Y. Su, E. A. Cooper, C. E. Elsbernd, and T. O. Mason, *J. Am. Ceram. Soc.* **73**, 3453 (1990).

[20] J. Rodríguez-Carvajal, M. T. Fernández-Díaz, and J. L. Martínez *J. Phys. C: Condens. Matter.* **3**, 3215 (1991).

[21] V. B. Grande, Hk.Müller-Buschbaum, and M. Schweizer, *Z. Anorg. Allg. Chem.* **428**, 120 (1977).

[22] J. Rodríguez-Carvajal, J. L. Martínez, and J. Pannetier, *Phys. Rev.* **B38**, 7148 (1988).

[23] D. E. Rice, M. K. Crawford, D. J. Buttrey, and W. E. Farneth, *Phys. Rev.* **B42**, 8787 (1990).

[24] A. Hayashi, H. Tamura, and Y. Ueda, *Physica* **C216**, 77 (1993).

[25] J. D. Axe, A. H. Moudden, D. Hohlwein, D. E. Cox, K. M. Mohanty, A. R. Moodenbaugh, and Youwen Xu, *Phys. Rev. Lett.* **62**, 2751 (1989).

[26] C. Chaillout, S. W. Cheong, Z. Fisk, M. S. Lehmann, M. Marezio, B. Morosin, and J. E. Schirber, *Physica* **C158**, 183 (1989).

[27] Z. Hiroi, T. Obata, M. Takano, and Y. Bando, *Phys. Rev.* **B41**, 11665 (1990).

[28] A. Demourgues, F. Weill, J. C. Grenier, A. Wattiaux, and M. Pouchard, *Physica* **C192**, 425 (1992).

[29] J. M. Tranquada, Y. Konig, J. E. Lorenzo, D. J. Buttrey, D. E. Rice, and V. Sachan, *Phys. Rev.* **B50**, 6340 (1994).

[30] J. M. Tranquada, J. E. Lorenzo, D. J. Buttrey, and V. Sachan, *Phys. Rev.* **B52**, 3581 (1995).

[31] P. G. Radaelli, J. D. Jorgensen, A. J. Schultz, B. A. Hunter, J. L. Wagner, F. C. Chou, and D. C. Johnston, *Phys. Rev.* **B48**, 499 (1993).

[32] B. O. Wells, R. J. Birgeneau, F. C. Chou, Y. Endoh, D. C. Johnston, M. A. Kastner, Y. S. Lee, G. Shirane, J. M. Tranquada, and K. Yamada, *Z. Phys.* **B100**, 535 (1996).

[33] B. O. Wells, Y. S. Lee, M. A. Kastner, R. J. Christianson, F. C. Chou, and R. J. Birgeneau, *NATO ASI Ser.,* **E343** 281 (1997).

[34] S. Hosoya, T. Omata, K. Nakajima, K. Yamada, and Y. Endoh, *Physica* **C202**, 188 (1992).

[35] D. E. Rice and D. J. Buttrey, *J. Solid State Chem.* **105**, 197 (1993).

[36] P. Zolliker, D. E. Cox, J. B. Parise, E. M. McCarron III, and W. E. Farneth, *Phys. Rev.* **B42**, 6332 (1990).

[37] D. Vaknin, J. L. Zarestky, D. C. Johnston, J. E. Schirber, and Z. Fisk, *Phys. Rev.* **B49**, 9057 (1994).

[38] M. F. Hundley, J. D. Thompson, S-W. Cheong, and Z. Fisk, and J. E. Schirber, *Phys. Rev.* **B41**, 4062 (1990).

[39] P. C. Hammel, A. P. Reyes, Z. Fisk, M. Takigawa, J. D. Thompson, R. H. Heffner, S-W. Cheong, J. E. Schirber, *Phys. Rev.* **B42**, 6781 (1990).

[40] J. Ryder, P. A. Midgley, R. Exley, R. J. Beynon, D. L. Yates, L. Afalfiz, and J. A. Wilson, *Physica* **C173**, 9 (1991).

[41] R. J. Birgeneau, H. J. Guggenheim, and G. Shirane, *Phys. Rev. Lett.* **22**, 720 (1969).

[42] R. J. Birgeneau, J. Als-Nielsen, and G. Shirane, *Phys. Rev.* **B16**, 280 (1977).

[43] K. Yamada, T. Omata, K. Nakajima, S. Hosoya, T. Sumida, and Y. Endoh, *Physica* **C191**, 15 (1992).

[44] D. E. MacLaughlin, J. P. Vithayathil, H. B. Brom, J. C. J. de Rooy, P. C. Hammel, P. C. Canfield, A. P. Reyes, Z. Fisk, J. D. Thompson, and S.-W. Cheong, *Phys. Rev. Lett.* **72**, 760 (1994).

[45] G. Aeppli and D. J. Buttrey, *Phys. Rev. Lett.* **61**, 203 (1988).

[46] G. Shirane, Y. Endoh, R. J. Birgeneau, M. A. Kastner, Y. Hidaka, M. Oda, M. Suzuki, and T. Murakami, *Phys. Rev. Lett.* **59**, 1613 (1987).

[47] K. B. Lyons, P. A. Fleury, J. P. Remeika, A. S. Cooper, and T. J. Negran, *Phys. Rev.* **B37**, 2353 (1988).

[48] K. Yamada, M. Arai, Y. Endoh, S. Hosoya, K. Nakajima, T. Perring, and A. Taylor, *J. Phys. Soc. Jpn.* **60**, 1197 (1991).

[49] E. T. Ahrens, A. P. Reyes, P. C. Hammel, J. D. Thompson, P. C. Canfield, and Z. Fisk, *Physica* **C212**, 317 (1993).

[50] R. K. Kremer, E. Sigmund, V. Hizhnyakov, F. Hentsch, A. Simon, K. A. Müller, and M. Mehring, *Z. Phys.* **B86**, 319 (1992).

[51] R. K. Kremer, V. Hizhnyakov, E. Sigmund, A. Simon, and K. A. Müller, *Z. Phys.* **B91**, 169 (1993).

[52] J. M. Tranquada, P. Wochner, A. R. Moodenbaugh,] and D. J. Buttrey, *Phys. Rev.* **B55,** R6113 (1997).

[53] P. Wochner, J. M. Tranquada, D. J. Buttrey, and V. Sachan, *Phys. Rev.* **B57,** 1066 (1998).

[54] T. Akashi, K. Matumi, T. Okada, and T. Mizutani, *IEEE trans.* **MAG-5**, 285 (1969).

[55] S. Kimura and I. Shindo, *J. Cryst. Growth* **41**, 192 (1977).

[56] K. Oka and H. Unoki, *Jpn. J. Appl. Phys.* **26**, L1590 (1987).

[57] K. Kobashi, T. Kyômen, and Masaharu Oguni, *J. Phys. Chem. Solids* **59,** 667-677 (1998).

[58] Ed. J. P. McCullough and D. W. Scoot, *Experimental Thermodynamics* **1**, *"Calorimetry of Non-reacting systems"*, Butterworths, London (1968).

[59] D. E. Burns, F. H. Dacol, D. E. Rice, D. J. Buttrey, and M. K. Crawford, *Phys. Rev.* **B42**, 10777 (1990).

[60] S. Sugai, S. Hosoya, T. Kajitani, T. Fukuda, and S. Onodera, *Physica* **C185-189**, 895 (1991).

[61] L. Pintschovius, J. M. Bassat, P. Odier, F. Gervais, G. Chevrier, W. Reichardt, and F. Gompf, *Phys. Rev.* **B40**, 2229 (1989).

[62] T. M. Brill, G. Hampel, F. Mertens, R. Schürmann, W. Assmus, and B. Lüthi, *Phys. Rev.* **B43**, 10548 (1991).

[63] K. Yamada, T. Omata, K. Nakajima, Y. Endoh, and S. Hosoya, *Physica* **C221**, 355 (1994).

[64] C. N. R. Rao and K. J. Rao, *Phase Transitions in Solids*, p.82. McGraw-Hill, New York (1978).

[65] K. F. Kelton, *Solid State Phys.* **45**, 75 (1991).

[66] M. Itoh, M. Oguni, T. Kyômen, H. Tamura, J. D. Yu, Y. Yanagida, Y. Inaguma, and T. Nakamura, *Solid state Commun.* **90**, 787 (1994).

[67] Y. Hongshun, Z. Xiaonong, Z. Changfei, W. Keqin, C. Liczhao, and C. Zhaojia, *Physica* **C172**, 71 (1990).

[68] C. Zener, "*Imperfections in nearly perfect crystals,*" J. Wiley, New York, (1952).

[69] P. G. Shewmon, *"Diffusion in Solids"*, McGraw-Hill, New York (1963).

[70] A. Migliori, William M. Visscher, S. E. Brown, Z. Fisk, S. -W. Cheong, B, Alten, E. T. Ahrens, K. A. Kubat-Martin, J. D. Maynard, Y. Huang, D. R. Kirk, K. A. Gillis, H. K. Kim, and M. H. W. Chan, *Phys. Rev.* **B41**, 2098 (1990).

[71] H. Fujimori and M. Oguni, *Solid State Commun.* **94**, 157 (1995).

[72] B. K. Chanudhuri, K. Nomoto, T. Atake, and H. Chihara, *J. Chem. Thermodyn.* **15**, 339 (1983); 383 (1983).

[73] K. Hamano, Y. Ikeda, T. Fujimoto, K. Ema, and S. Hirotsu, *J. Phys. Soc. Jpn.* **49**, 2278 (1980); *Ferroelectrics* **36**, 343 (1981).

[74] P. Figuiere, H. Szwarcm, M. Oguni, and H. Suga, *J. Chem. Thermodyn.* **17**, 949 (1985).

[75] N. Okamoto, M. Oguni, and H. Suga, *Solid State Commun.* **70**, 219 (1989).

[76] T. Kajitani, Y. Kitagaki, K. Hiraga, S. Hosoya, T. Fukuda, Y. Tamaguchi, S. Wada, S. Sugai, Y. Morii, k. Fuchizaki, and S. Funahashi, *Physica* **C185-189**, 579 (1991).

[77] P. Muralt, R. Kind, and W. Bührer, *Phys. Rev.* **B38**, 666 (1988).

[78] M. B. Salamon and H. Ikeda, *Phys. Rev.* **B7**, 2017 (1973).

[79] T. Kyômen, M. Oguni, M. Itoh, and J. D. Yu, *Phys. Rev.* **B51,** 3181 (1995).

[80] J. D. Yu, Y. Inaguma, M. Itoh, M. Oguni, and T. Kyômen, *Phys. Rev.* **B54,** 7455 (1996).

[81] R. A. Mohan Ram, L. Ganapathi, P. Ganguly, and C. N. Rao, *J. solid State Chem.* **63,** 139 (1986).

[82] J. D. Jorgensen, B. W. Veal, A. P. Paulikas, L. J. Nowicki, G. W. Crabtree, H. Claus, and W. K. Knok, *Phys. Rev. B41,* 1863 (1990).